Cell

Organ-specific electrophile responsivity mapping in live *C. elegans*

Graphical abstract

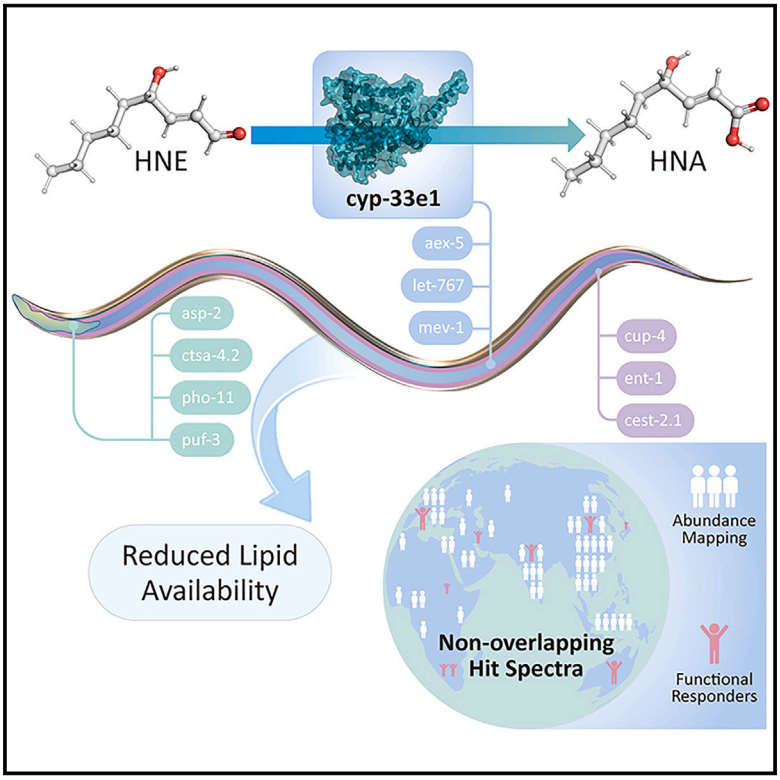

Highlights

- Localis-REX maps organ-specific electrophile-responsive proteins in worms
- Hits are neither identified by organ-specific Ultra-ID nor biased by localized expression
- Hits are enriched in proteins functionally relevant to stress-related phenotypes
- Localized responsivity of gut-specific hit, cyp-33e1, shapes global lipid availability

Authors

Jinmin Liu, Amogh Kulkarni, Yong-Qi Gao, ..., Balázs Á. Novotny, Marcus J.C. Long, Yimon Aye

Correspondence

marcusjohncurtis.long@unil.ch (M.J.C.L.), yimon.aye@chem.ox.ac.uk (Y.A.)

In brief

Context-specific protein reactivity is a cornerstone of biological stress responsivity and thus has important ramifications for drug discovery. No current method can inform on these parameters. Here, we debut a method that cartographs locale-specific actionability to reactive metabolites. Cyp-33e1, a gut-specific responder, emerged to partition between electrophile-driven localized enzymatic turnover that triggers gut-specific metabolite production shaping global lipid storage and localized electrophile sensing that marshals global stress response.

Liu et al., 2024, Cell *187*, 7450–7469
December 26, 2024
https://doi.org/10.1016/j.cell.2024.10.014

CellPress

CellPress
OPEN ACCESS

Cell

Article

Organ-specific electrophile responsivity mapping in live *C. elegans*

Jinmin Liu,[1,2] Amogh Kulkarni,[2,3] Yong-Qi Gao,[2] Daniel A. Urul,[2,4] Romain Hamelin,[2] Balázs Á. Novotny,[2] Marcus J.C. Long,[5,*] and Yimon Aye[1,2,6,*]

[1]Department of Chemistry, University of Oxford, Oxford OX1 3TA, UK
[2]Swiss Federal Institute of Technology Lausanne, Lausanne 1015, Switzerland
[3]Friedrich Schiller University, 07737 Jena, Germany
[4]AssayQuant Technologies, Marlboro, MA 01752, USA
[5]University of Lausanne, Lausanne 1015, Switzerland
[6]Lead contact
*Correspondence: marcusjohncurtis.long@unil.ch (M.J.C.L.), yimon.aye@chem.ox.ac.uk (Y.A.)
https://doi.org/10.1016/j.cell.2024.10.014

SUMMARY

Proximity labeling technologies are limited to indexing localized protein residents. Such data—although valuable—cannot inform on small-molecule responsivity of local residents. We here bridge this gap by demonstrating in live *C. elegans* how electrophile-sensing propensity in specific organs can be quantitatively mapped and ranked. Using this method, >70% of tissue-specific responders exhibit electrophile responsivity, *independent* of tissue-specific abundance. One responder, cyp-33e1—for which both human and worm orthologs are electrophile responsive—marshals stress-dependent gut functions, despite manifesting uniform abundance across all tissues studied. Cyp-33e1's localized electrophile responsivity operates site specifically, triggering multifaceted responses: electrophile sensing through the catalytic-site cysteine results in partitioning between enzyme inhibition and localized production of a critical metabolite that governs global lipid availability, whereas rapid dual-cysteine site-specific sensing modulates gut homeostasis. Beyond pinpointing chemical actionability within local proteomes, organ-specific electrophile responsivity mapping illuminates otherwise intractable locale-specific metabolite signaling and stress response programs influencing organ-specific decision-making.

INTRODUCTION

Single-cell RNA sequencing (scRNA-seq) and proximity mapping technologies have revolutionized precision investigations into locale-specific biological makeups. At the proteome level, pioneering techniques like BioID/TurboID, APEX, and μMap are leading the way to census protein residents at defined biological locales,[1–4] although techniques like BONCAT that profile localized nascent proteomes[5,6] are also insightful. Nonetheless, we remain limited in mapping locale-specific chemical actionability, i.e., how protein responsivity to small molecules varies as a function of tissue or subcellular contexts. Indeed, mapping the plasticity of chemical reactivity as a function of locale remains outside the remit of all cutting-edge methods. This is because noninvasive strategies to selectively dispatch biologically or drug-relevant, yet ephemeral, small molecules to a specific organ/tissue within an intact organism on demand are scarce. Indeed, to identify chemically actionable protein targets, reactive small-molecule metabolites, or drug-like electrophilic fragments, are often administered in bulk to cells/animals. Such approaches have limited spatiotemporal precision and poor control of reactive ligand distribution, bioavailability, and metabolism. These uncontrolled approaches are also prone to issues associated with reactive electrophile overload, including toxicity and stress.

Unfortunately, signaling modalities of electrophiles are particularly context dependent, with productive signaling occurring upon the correct confluence of situation, association, and redox state/microenvironment of specific proteins.[7] Uncovering such context-specific responsivity to reactive metabolites is biomedically important because innate electrophile signaling can modulate specific signaling pathways.[8–12] Such data can uncover rapid response circuits and also elucidate (specific) functions of specific proteins within these pathways, e.g., in specific subcellular compartments[13] or cell types.[14] As electrophile-protein engagement mimics how covalent drug-protein interactions occur, such discoveries are also relevant to drug design.[15–19]

Here, we evaluate the hypothesis that by releasing a transient burst of a specific native electrophile in a specific organ of a live, intact worm, we can fingerprint localized native proteins with privileged functional electrophile responsivity in the organ of interest. We achieved this feat using a method that mimics natural, localized, transient signaling by the native electrophilic

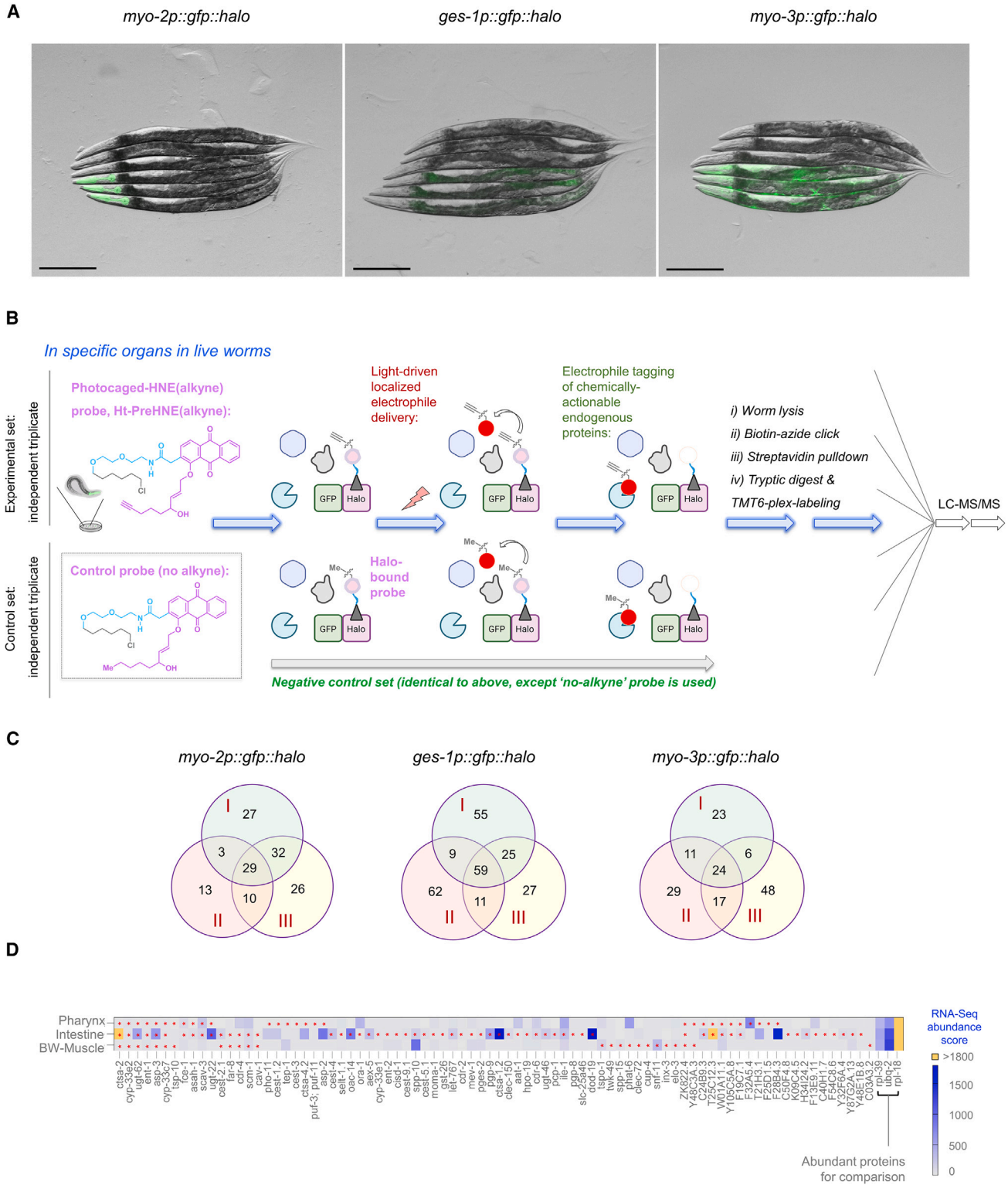

Figure 1. OS-Localis-REX identifies *chemically actionable* tissue-specific targets independent of native tissue preference/abundance

(A) Fluorescence imaging confirmed tissue-specific GFP-Halo expression in day 1 adult worms: myo-2, ges-1, and myo-3 promoters respectively drive GFP-Halo expression in pharynx, intestine, and body-wall muscles (3 transgenic worms [lower] against 3 wild-type N2 worms [upper]). Scale bars: 200 μm. See also Figure S1A–S1D. Note: due to mosaicity, GFP expression patterns were not identical across worms in the same group.

(legend continued on next page)

metabolite, 4-hydroxynonenal (HNE).[7] This setup, termed "organ-specific (OS) Localis-REX" hereafter, allows the best protein sensors to be HNEylated prior to interception by bystander proteins (which are frequently labeled during bolus administration). We used enrichment-coupled quantitative mass spectrometry (MS) to identify electrophile-actionable proteins in specific locales. The resulting maps of local proteome responsivity within distinct organs revealed that >70% of the targets displayed localized electrophile responsivity, unreflective of tissue-specific abundance.[20] Proteins identified in OS-Localis-REX workflow were also not identified by tissue-specific biotinylation using Ultra-ID, a hyperactive variant of BioID.[21] Several of the identified proteins emerged to be involved in tissue-specific homeostatic regulatory events consistent with the locales in which they were identified. More frequently than expected based on literature precedents, knockdown of these genes changed responsivity to electrophilic stress, consistent with OS-Localis-REX hits being involved in electrophilic stress management. We pursued one specific candidate, cyp-33e1. Both *C. elegans* and human orthologs emerged to be electrophile responsive. In *C. elegans*, despite similar expression across all 3 organs, cyp-33e1 was an active electrophile responder specifically in the gut, consistent with our data from OS-Localis-REX. This localized electrophile responsivity in turn triggered a gut-specific signaling program crucial for global lipid homeostasis.

These data support that contrary to other methods,[22] OS-Localis-REX directly informs on chemical actionability within specified local proteomes in live animals, independent of locale-specific expression levels. Beyond paving the way toward an arsenal of chemical genetic methods to perturb *local* proteome function in living systems, data so derived *proffer* a means to identify OS responders to localized stress. Such information is not easily accessible by traditional profiling technologies.

RESULTS

OS controlled electrophile generation, OS-Localis-REX, in *C. elegans*

Our experimental design involved repurposing our precision electrophile delivery tools[8] to achieve light-driven release of a reactive native electrophile within specific organs in *C. elegans*. To anchor our small-molecule photocaged-electrophile probe[23,24] that interacts specifically with Halo protein in specific tissues in live worms, we generated worms with tissue-specific expression of GFP-Halo. Our chosen promoters to drive GFP-Halo expression were myo-2p (pharyngeal expression), ges-1p (intestinal expression), and myo-3p (body-wall [BW] muscle expression). We surmised that following exposure of these live transgenic worms to our probe, Halo protein would irreversibly anchor our photocaged-electrophile probe, such that following washout of unbound probe, light illumination would drive tissue-specific electrophile release. Worms with non-integrated extrachromosomal arrays were thus created, which were transmissive at ~70% frequency and showed expected tissue-specific, albeit, as expected mosaic, GFP expression (Figure 1A). There was less than 2-fold difference in Halo expression across these constructs (Figure S1A).

We chose to release the endogenous lipid-derived electrophile, HNE. This choice was spurred by HNE's prevailing, yet poorly understood, context-specific pathophysiological roles, including in myriad neurodegenerative disorders,[7,25,26] where *C. elegans* is an established model.[27–29] Furthermore, recent work indicates that HNE houses a natural electrophilic pharmacophore of relevance to precision medicine design.[12,15] We thus used our photocaged HNE(alkyne-functionalized) probe (Ht-PreHNE, hereafter, Figures 1B and S1B) that undergoes efficient cellular uptake, is stable when bound to Halo, and is non-toxic in multiple live models.[14,23,24,30] Alkyne modification allows efficient HNE detection, orthogonal from a non-alkyne-tagged variant used as a control during OS-Localis-REX profiling. Alkyne-modified HNE is commonly deployed and is widely accepted to be non-invasive as the alkyne is remote from the site of electrophilic chemistry and innocuously changes HNE's physiochemical properties.

Using an optimized Ht-PreHNE dosage over 6-h treatment followed by washout of excess unbound probe, the probe selectively labeled the desired tissues in all localized Halo-expressing strains (Figures S1C and S1D). Photouncaging of HNE(alkyne) using a low-power hand-held lamp (5 mW/cm^2, 366 nm) was rapid, $t_{1/2(\text{photouncaging})}$~0.5 min (Figures S1E and S1F). The liberated HNE-labeled proteins in live worms (Figure S1G).

Mapping OS functional first responders in live *C. elegans* using OS-Localis-REX

We proceeded to identify HNE responders as a function of locale. Tandem mass tag (TMT)-6-plex labeling[31] was used to quantitatively score enriched targets from each strain over three independent biological replicates against a control triplicate set (processed identically but treated with a non-alkyne-functionalized probe) (Figures 1B and S1G–S1I; Data S1 and

(B) OS-Localis-REX: organ-specific Halo-transgenic worms were treated with either photocaged HNE(alkyne) (Ht-PreHNE[alkyne]) (experimental set comprising independent biological triplicates, top) or a non-alkyne-functionalized variant, Ht-PreHNE(no alkyne) (triplicate controls, bottom). Following washout, light (5 mW/cm^2, 366 nm, 3 min) exposure rapidly ($t_{1/2}$ ~0.5 min) liberates the electrophile, HNE(alkyne), or HNE(no alkyne). Alkyne-functionalized HNEylated native protein responders were enriched by biotin-azide click coupling and streptavidin pull-down, whereas HNE(no-alkyne)-tagged proteins were not enriched. Samples were subjected to trypsin digest, isotopic labeling, and liquid chromatography-tandem mass spectrometry (LC-MS/MS) analysis. See also Figures S1E–S1H.

(C) 29, 59, and 24 proteins were selected as significant electrophile-responders in indicated tissue-specific GFP-Halo-transgenic strains, across three independent biological replicates (labeled as I, II, and III) against corresponding controls. See also Figure S1I and Data S1, S2, and S3.

(D) 59 from 82 (~72%) non-overlapping significant hits across the 3 strains reflect electrophile-actionable protein targets, whose tissue-specific electrophile responsivity manifested in tissues (marked by *) that are not their canonical native/preferred locale(s) (represented by heatmap indicating transcript scores derived from cell-specific RNA-seq datasets[20]; yellow denotes heatmap scores >1,800). Note: highly abundant *C. elegans* proteins—rpl-39, ubq-2, and rpl-18—and their tissue-specific distributions are included for comparison: these proteins were not scored as electrophile-responders by OS-Localis-REX. See also Figure S1J and Data S2.

See also Figures S1 and S3.

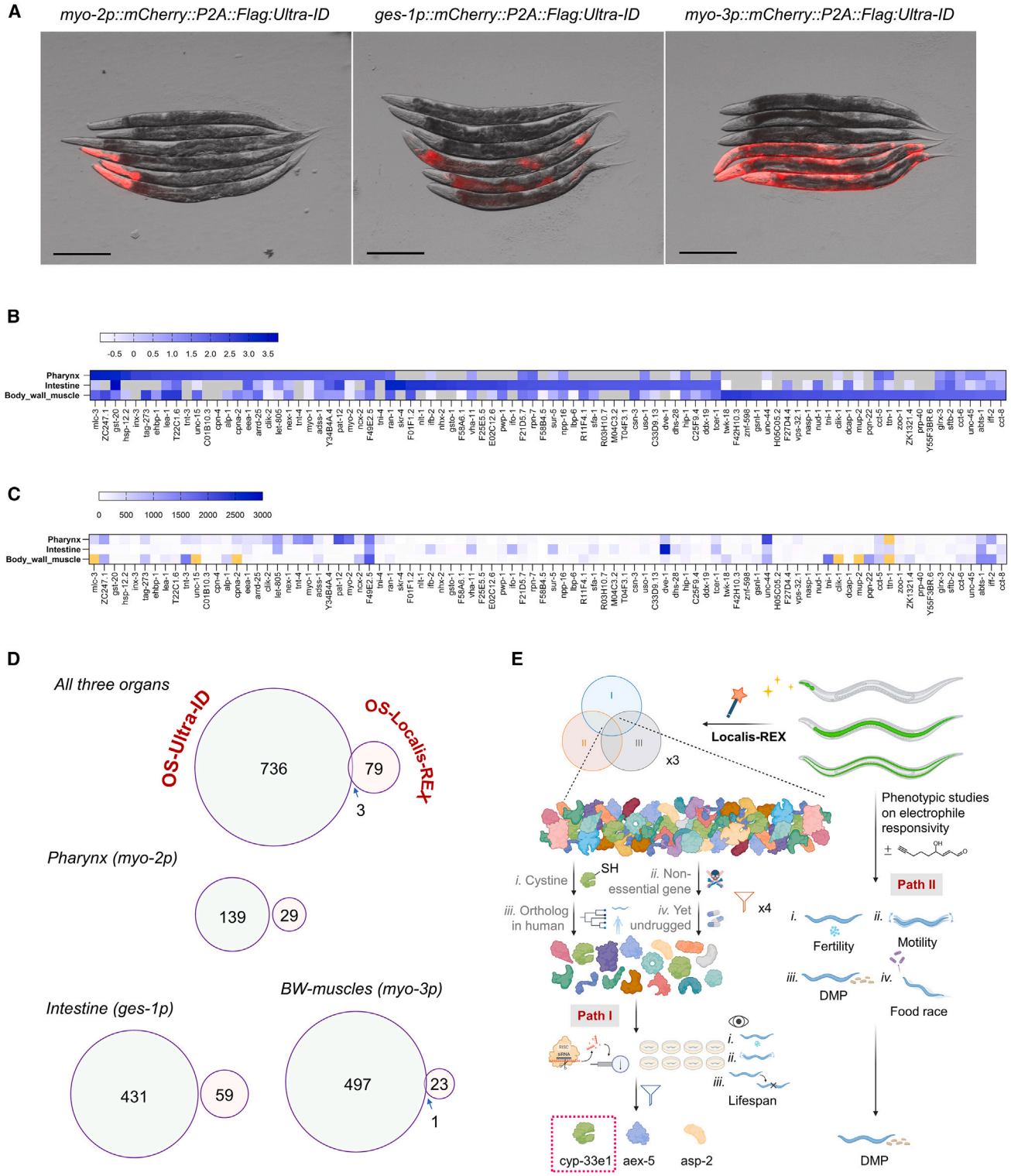

Figure 2. OS-Localis-REX and OS-Ultra-ID exhibit divergent target spectra and functional enrichment

(A) Fluorescence imaging of mCherry expression in day 1 Ultra-ID transgenic hermaphrodites. Each image shows 3 tissue-specific mCherry-P2A-Ultra-ID-expressing animals (lower), against 3 wild-type N2 worms (upper, controls). Scale bars: 200 μm. Note: due to mosaicity, mCherry expression patterns are not identical across all 3 transgenic worms. See also Figures S2A–S2D.

(legend continued on next page)

S2; Methods S1). For each strain, enriched proteins were strongly correlated (Pearson r > 0.95) (Data S3A). We thus identified responders in the pharynx (29), intestine (59), and BW muscles (24) (Figure 1C). ~70% of these hits were HNE responsive only in one tissue, and ~20% were responsive in two tissues (Data S2). Several tissue-specific responders are involved in processes relevant to the tissue in which they sensed electrophiles: e.g., aex-5, an intestinal-specific responder, functions in the intestinal regulation of *C. elegans* defecation motor program (DMP),[32] and aex-5 mutant animals have impaired intestinal fat metabolism.[33]

Tissue-specific electrophile responsivity identified by OS-Localis-REX is not correlated with tissue-specific expression

Comparison of our Localis-REX hits against published *C. elegans* tissue-specific scRNA-seq datasets[20] showed that tissue-specific electrophile responsivity was independent of expression in respective tissues (Figure 1D). A similar conclusion was drawn upon comparison of our Localis-REX hits with PAXdb, a protein abundance database derived from published experimental data (Figure S1J). Such observations indicate that locale-specific expression does not strongly influence locale-specific electrophile responsivity, consistent with a recent report from our laboratory investigating subcellular responsivity to electrophiles.[13]

We sought further evidence to rule out that our identified tissue-specific HNE responders were biased by protein abundance in the tissues we profiled. We engineered worms expressing Ultra-ID (the smallest and most active promiscuous biotin ligase available to date[21] for proximity/interactome mapping). Tissue-specific Ultra-ID expression was driven by the same promoters used in OS-Localis-REX. We validated Ultra-ID localization in each strain by imaging *mCherry* (encoded upstream of *Ultra-ID*, spaced by P2A "self-cleaving" peptide[24]; Methods S1; Figures 2A and S2A). In these OS Ultra-ID strains, total proteome abundance/composition[34] was largely unaffected (Figure S2B; Data S4). Streptavidin blot confirmed biotinylation activity of Ultra-ID in each strain (Figure S2C).

To reduce background biotinylation, we used biotin-auxotrophic *E. coli* as food[35] (Figures S2C and S2D). We then executed OS-Ultra-ID, mapping locale-specific protein abundance over 3 independent biological replicates, against 2 separate control groups in triplicate (Data S5). Briefly, post-worm lysis, streptavidin enrichment, on-bead digestion of enriched proteins, and labeling of eluted peptides with isotopomeric TMT labels,[31] peptides were compared by MS (Figures S2E and S2F). This workflow is similar to the enrichment workflow deployed in OS-Localis-REX, except endogenously biotinylated proteins cannot be removed prior to enrichment, as they are in OS-Localis-REX (Figures 1B, S1I, S2E, and S2F; Data S3B).

Assessment of OS-Ultra-ID datasets unveiled several key points (Figures 2B–2D and S2G). (1) Numerous targets were captured exclusively in a single tissue: focusing on enriched hits (with protein false discovery rate [FDR] $\leq$ 0.05) bearing 2-fold change against biotin-treated wild-type (WT) controls, 32, 107, and 125 (Figure S2G, lower-right) respectively constitute proteins abundantly expressed in one locale. (2) Taking 30 top-ranked hits (FDR $\leq$ 0.05) from each tissue as representatives, the resultant tissue-specific expression profiles (Figure 2B) were consistent with those derived from scRNA-seq[20] (Figure 2C), validating the scRNA-seq datasets used above (Figure 1D). (3) Despite the fact that both OS-Localis-REX and OS-Ultra-ID deployed similar biotin-based enrichment strategies (Figures 1B and S1I; cf. Figures S2E and S2F), there was minimal overlap between the techniques (Figure 2D). Even when all 739 enriched proteins (FDR $\leq$ 0.05) across all organs from OS-Ultra-ID were considered, only 3 proteins (Figure 2D, top row) overlapped between OS-Ultra-ID and OS-Localis-REX: *two of these overlapping hits were identified in different locales*. Based on the parity of scRNA-seq and OS-Ultra-ID, as well as OS-Ultra-ID and OS-Localis-REX identifying some overlapping proteins but mostly in *different* locales, we conclude that OS-Localis-REX pinpoints bona fide responders whose HNE responsivity is augmented in specific locales, independent of expression. Finally, functional enrichment analyses using two independent programs (Cytoscape and g:*Profiler*)[36] showed non-overlapping Gene Ontology (GO) subterms and KEGG pathway terms

(B) Tissue-specific protein abundance mapped by OS-Ultra-ID, featuring top ~30 hits (from 90 total) ranked based on $\log_2$FC (fold change of designated transgenic strain against wild type) and FDR for all hits $\leq$0.05. Gray boxes denote corresponding proteins not identified. See also Figures S2E–S2G and Data S5. Scale bar above designates $\log_2$FC (designated transgenic strain vs. wild type) derived from TMT ratios (see Data S5A–S5C).

(C) OS-Ultra-ID hits shown in (B) were searched for their corresponding tissue-specific abundance scores from cell-specific RNA-seq datasets, covering the same tissues. Yellow boxes correspond to transcript scores >3,000 (thus, out of range of the indicated scale bar).

(D) Top: by applying FDR $\leq$ 0.05 and $\log_2$FC (designated transgenic strain vs. wild type) >0 to OS-Ultra-ID hits across all 3 tissues, the resulting 739 targets (Data S5A–S5C) featured only 3 proteins that overlapped with chemically actionable responders mapped by OS-Localis-REX (Figure 1D; Data S1, S2, and S3). Bottom: same analysis as above but within each tissue, revealing no overlap between OS-Ultra-ID (larger circle) and OS-Localis-REX (smaller circle) hits, except in body-wall muscles (one overlapping target, cav-1). Such divergence extends to outputs obtained from functional pathway enrichments. See also Figure S3 and Data S1 vs. S5.

(E) Roadmap illustrating OS-Localis-REX hit discovery and subsequent functional and phenotypic validations. Top left: selection criteria (i–iv) applied to 82 first responders from OS-Localis-REX (see Figures 1C and 1D) manifesting at least one cysteine; human orthologs; and disease relevance. Essential genes (not amenable to KO/KD studies in whole animals) were further removed; hits yet unknown to be druggable/ligandable were favored, while ensuring final selected list reflected both unique and common hits across three different tissues. The resulting 15 candidates were then subjected to: (path I) RNAi phenotypic screen, against commonly assayed *C. elegans* phenotypes: (1) egg-laying (fertility); (2) movements (motility); and (3) lifespan (survival). Note: tissue-specific RNAi screen, in lieu of/supplementing ubiquitous knockdown, may be undertaken here, as was done for aex-5. A parallel RNAi screen in the presence or absence of acute electrophilic stress, focusing on egg-laying, pinpointed 3 potential electrophile-stress-dependent functionally relevant candidates: cyp-33e1, aex-5, and asp-2. T-REX cell-based validations singled out cyp-33e1 (and its human ortholog, CYP2A6) as kinetically privileged responder and established labeling sites. In path II, DMP, a phenotype reporting intestinal physiology, was first identified as the phenotype most affected by acute electrophilic stress.
See also Figures S2 and S3.

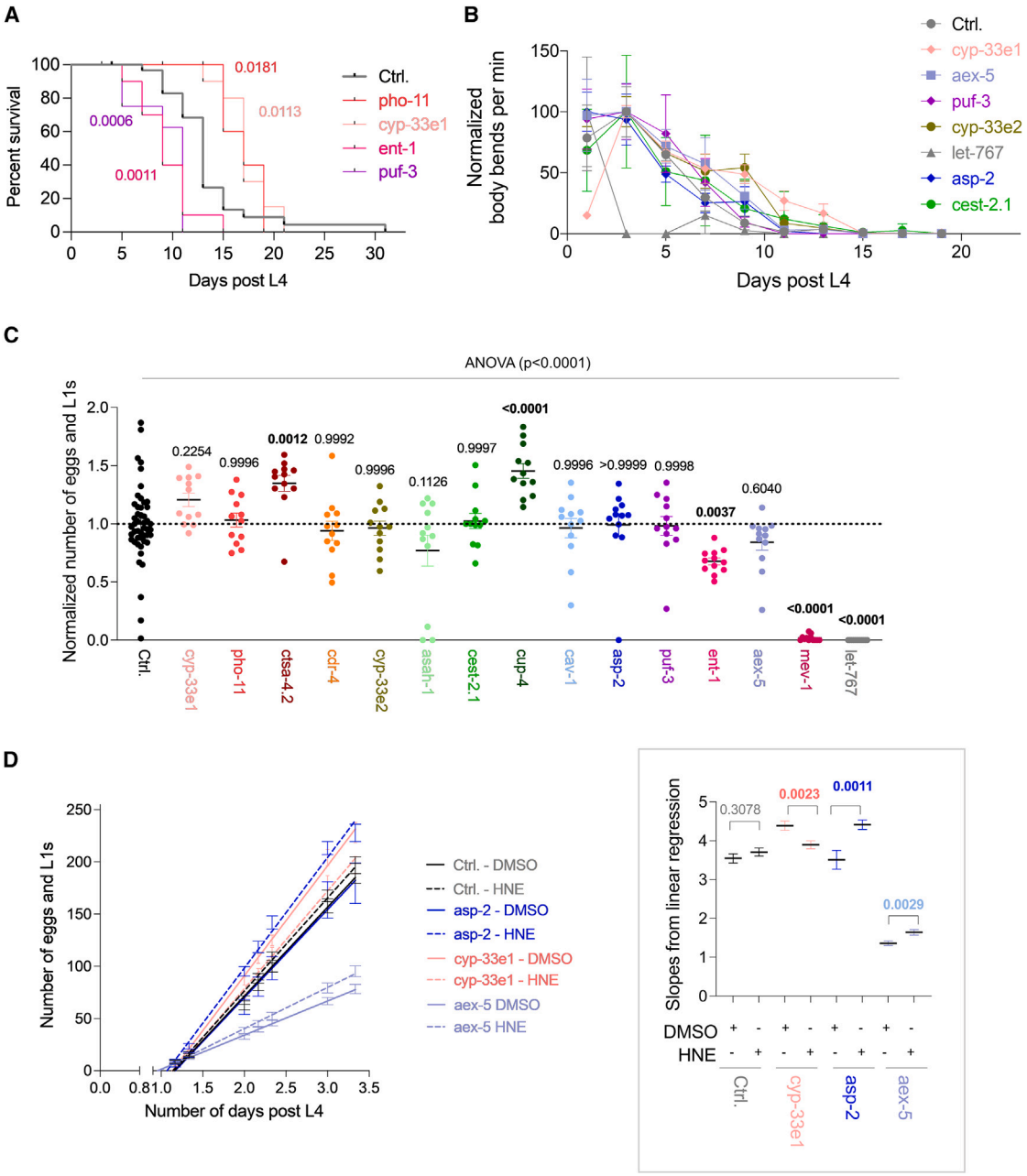

Figure 3. RNAi knockdown of OS-Localis-REX hits influences survival, motility, and reproductive fitness

(A) Pho-11, cyp-33e1, ent-1, and puf-3 (see Figures S4A–S4C and Methods S1) were identified as 4 genes (from 15) whose RNAi significantly affected survival, following application of log-rank (Mantel-Cox) test, with indicated *p* values. See also Figure S4D: aex-5 was significantly different from control when Gehan-Breslow-Wilcoxon (GBW) test was applied. *n* = 30 for the control group; *n* = 10 for other groups.

(B) Normalized body bends per min of worms where RNAi of individual indicated genes significantly altered motility with respect to control animals, as judged by Gaussian distribution analysis (see Figures S4E and S4F). Data were normalized such that the highest body-bending rate corresponds to 100. *n* = 30 for the control group; *n* = 10 for other groups.

(C) Total number of eggs and L1s from indicated RNAi-fed worms in the absence (Ctrl.) and presence of RNAi of indicated genes. Data were normalized to the mean of control (Ctrl.). *p* values were calculated using Dunnett's multiple comparisons test against control group. Corrected $p < 0.05$ are in bold. *n* = 30 for the control group; *n* = 10 for other groups.

(D) Linear regression analysis of the number of fertile eggs over indicated days where knockdown of indicated genes resulted in differential reproductive fitness, in the presence (HNE) vs. absence (DMSO) of electrophilic stress, compared with knockdown control (Ctrl.). See also Figures S4G and S4H for data from all 15

(legend continued on next page)

between OS-Localis-REX vs. OS-Ultra-ID in each tissue (Figure S3).

Proteins mapped by OS-Localis-REX influence animal health and physiology

Among the 82 responders mapped by OS-Localis-REX across all strains, 18 proteins are not yet functionally annotated in Wormbase. BLAST analysis showed that 6 of these 18 proteins showed ~17%–47% sequence identity with human proteins (Data S2). Thus, ~76%, 62 *C. elegans* responders out of 82, represented proteins with human orthologs. ~67% (55/82) are disease-associated genes, but only 43% (35/82) are chemically actionable based on representation in DrugBank (Data S2). With the goal of identifying interesting "undruggable" proteins for in-depth investigations, we studied functional relevance of 15 selected hits having (1) human orthologs of disease relevance (Figures 2E and S4A), (2) no known electrophile sensitivity/druggability (Data S2), and (3) both human and worm orthologs housing at least one cysteine (Figure 2E). These 15 candidates further reflect both unique and common hits across the three tissues (Figure S4A; Data S2).

Initially, we assessed the functional relevance of these proteins using RNAi (Figure 2E), focusing on readily measurable phenotypes: (1) survival, (2) motility, and (3) reproductive fitness. Animals were fed double-stranded RNA (dsRNA)-producing HT115 bacteria containing plasmids from the Ahringer library.[37] Knockdown efficiencies (Figure S4B; Methods S1) were >90% for most genes. However, efficiencies were closer to 50% for 4 genes (Figure S4B), possibly reflecting low efficiency or expression localization to regions impermeable to RNAi, such as neurons,[38] which are not the focus of our study. RNAi targeting let-767 (a positive control) caused development and growth defects, as previously reported.[39–41]

Survival management

Deficiency in aex-5, pho-11, and cyp-33e1 prolonged mean lifespan, whereas puf-3 and ent-1 (beyond let-767, positive control) deficiency reduced lifespan (Figures 3A, S4C, and S4D). Our data on aex-5 are consistent with a previous report.[42] pho-11-knockdown reduces survival of otherwise lifespan-extended *daf-2* and *daf-16* mutant animals,[43] although pho-11-deficiency in the WT background has not previously been assayed. Puf-3 RNAi-fed animals manifested shortened lifespans. In mouse, hyperactivity of a closely related isoform of puf-3's human ortholog, PUM2, drives premature aging.[44] Notably, ent-1 RNAi, in our hands, reduced the lifespan, but a previous study reported no effect on lifespan.[45] Nonetheless, the overall consistency of the outcomes from our survival-curve analysis and additional interesting, previously unknown, findings with relatable phenotypes in human orthologs altogether hint at the conserved importance of OS-Localis-REX targets in animal survival.

Motility

Pharynx and BW muscles are critical for nematode movement. Body bends per minute (BPM) is an indicator of *C. elegans* musculature function. L3/L4 larvae subjected to let-767 RNAi manifested uncoordinated movement as reported,[39,41] validating our workflow. Knockdown of several other hits showed significant motor defects (Figures 3B and S4E). Applying a stiff cutoff ($\pm 2\sigma$) to Gaussian fit of the resultant measurements across all hits over the three developmental stages assayed revealed that, in addition to let-767 RNAi, asp-2 RNAi caused significant positive deviation from the mean BPM (Figure S4F). Asp-2 is orthologous to cathepsin-E, a disease-associated aspartic protease expressed in mammalian immune system and epidermis. Cathepsin-E deficiency decreases motility of dendritic cells[46] and Schwann cells.[47]

Reproductive fitness

The effects of RNAi on the total number of fertilized eggs were next assessed for the 15 candidate proteins. let-767 RNAi decreased fertility, as expected (Figure 3C). The same result was observed in animals treated with RNAi of mev-1, whose human ortholog corresponds to subunit-C of the mitochondrial tumor suppressor protein, succinate dehydrogenase (SDH, also known as complex-II), a non-essential component of the electron transport chain and contributor to the TCA cycle.[48] Loss-of-function mutations in SDH subunits increase predisposition to cancers.[49] In *C. elegans*, a homozygous missense mutant of mev-1 with depleted complex-II activity[50] shortens lifespan,[51–53] although RNAi of mev-1 has no effect on lifespan,[54,55] consistent with our data (Figures 3A, S4C, and S4D). mev-1 loss-of-function mutant worms have diminished fecundity,[54] in agreement with our data (Figure 3C). ent-1 RNAi-fed animals, beyond reduced survival (Figures 3A, S4C, and S4D), displayed diminished fecundity (Figure 3C). The human ortholog of ent-1 is SLC29A1, encoding equilibrative nucleoside transporter 1 (ENT1). Polymorphisms in SLC29A1 are linked to multiple diseases and drug resistance. Ent1$^{-/-}$ mice show paralysis among other defects.[56,57] By contrast, depletion of ctsa-4.2 (human ortholog: CTSA, lysosomal cathepsin-A serine carboxypeptidase) and cup-4 gene, encoding a coelomocyte-specific ligand-gated ion channel (human ortholog: CHRNA9), has increased fertility (Figure 3C).

OS-Localis-REX hit proteins are implicated in stress-induced changes in animal reproductive fitness

We next investigated how deficiency of our candidate proteins impacts response to HNE stress. For these experiments, we measured reproductive fitness, as this phenotype allows more high-throughput scoring. Furthermore, acute electrophilic stress exerts strong effects on cell cycle in nematodes,[58] and reproductive fitness is strongly dependent on cell-cycle progression. We thus quantitatively compared fecundity and fertility scores in DMSO- or HNE-treated worms for each RNAi. Since the number of fertile eggs laid proceeds at a consistent rate over several days during young adulthood, the cumulative total of eggs laid can be reliably fit by linear regression. Using this analysis, we assessed to what extent the gradients for DMSO- and HNE-treated

genes. Inset: slope values from linear regression. *p* values from unpaired, two-tailed Students' t test. Bonferroni adjustment was applied, *p*: adjusted, 0.003125. $n = 48$ for the control group; $n = 12$ for other groups.
All data present mean ± SEM. Decision tree for statistical treatment in Methods S3.
See also Figure S4.

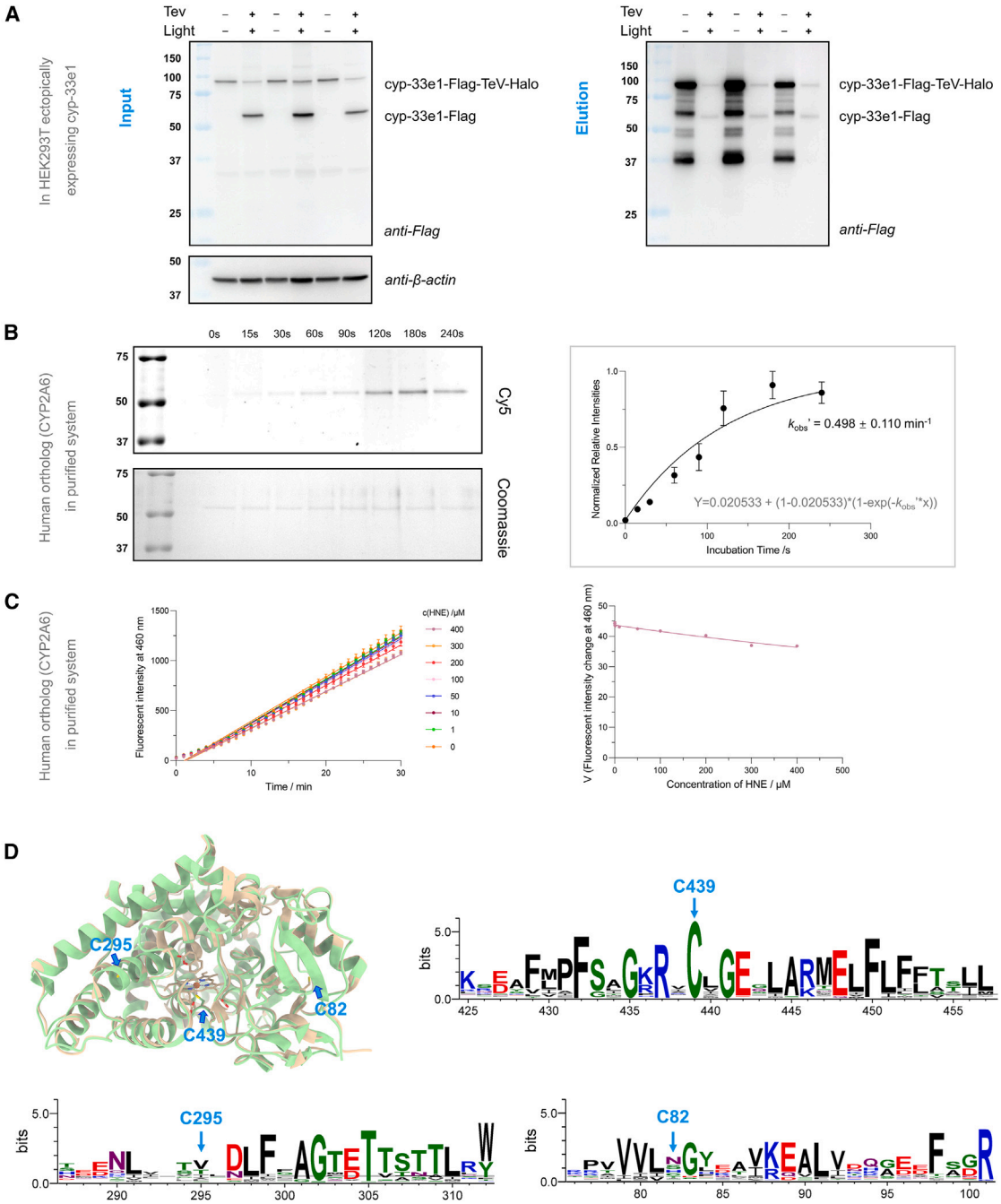

Figure 4. cyp-33e1 and its human ortholog CYP2A6 are kinetically privileged responders

(A) cyp-33e1 was scored as a first responder using T-REX in HEK293T (see Figure S5A). Input and elution samples resulting from Click-biotin pull-down of the protein post cell lysis and subsequent TeV-protease-mediated separation of Halo and cyp-33e1, analyzed by western blot using anti-FLAG and anti-β-actin antibodies. MWs: cyp-33e1-FLAG-TeV-Halo-His: 95 kDa, cyp-33e1-FLAG (post TeV cleavage): 60 kDa. Note: incomplete TeV cleavage results in residual full-length fusion protein in "+ TeV" lanes in both input and elution. Inadvertent cleavage occurs during pull-down, leading to multiple FLAG-positive bands in negative-control samples in elution. Nonetheless, the HNE(alkyne)-tagged enriched species in experimental samples (+ TeV, + light) in elution corresponds to full-length cyp-33e1.

(B) Labeling of recombinant CYP2A6 labeling by HNE(alkyne). Inset: quantification. $k_{obs}' = 0.50 \pm 0.110$ min^{-1} was calculated by normalized HNEylation, to CYP2A6 amount deployed and fitting to: Y = 0.021 + (1–0.021) * (1-exp(−k_{obs}'*x)). For comparison with the previously reported HNE responders (Ube2v2: 2.1 × 10^8; HSPB7: 8.5 ± 1.2 × 10^7; HuR: 5.1 ± 0.6 × 10^6 M^{-2}s^{-1}), the k_{obs}' was adjusted to equivalent concentrations as in previous studies, resulting in k_{obs} ~4 × 10^8 M^{-2}s^{-1}. n = 3 for all conditions.

(legend continued on next page)

worms were different for each condition. There was no significant difference between the twain for control-RNAi-treated worms (*p*, unadjusted, value 0.3078) (Figure 3D). Given that we have 15 different RNAi's and a control, we applied the Bonferroni adjustment to the resulting analysis (null hypothesis rejected if $p < 0.003125$), which revealed that cyp-33e1, aex-5, and asp-2 play functional roles in reproductive fitness during stress (Figures 3D, S4G, and S4H). The fact that 20% of our studied proteins were linked to martialing HNE stress is surprising. Although the percentage of HNE responders across proteomes is unknown, several methods have shown that proteins highly sensitive to HNE are scarce: a previous study estimated that ~98% of cysteines are unresponsive to specific electrophiles,[59] and another study, using electrophiles more reactive than HNE, estimated that ~5% of cysteines are reactive in worms.[60]

In parallel, we also explored preliminarily how phenotypic changes may be functionally linked to specific tissues where these proteins were identified by OS-Localis-REX, harnessing tissue-specific gene knockdown in *C. elegans*. Using aex-5 as an initial test case, the diminished egg-laying rate was recapitulated when aex-5 RNAi was targeted to intestinal cells but not to BW-muscle cells (Figure S4L). Interestingly, aex-5 was mapped by OS-Localis-REX as an intestine-specific responder (Figures 1D and S4A; Data S1 and S2). Based on a previous report indicating a link between global deficiency of aex-5 and decreased fat accumulation,[33] we further examined the effects of aex-5 deficiency on global lipid content. Using the oil red O (ORO) staining assay, we found aberrant lipid accumulation in the anterior intestine in L4 aex-5-depleted worms (Figure S4I) but decreased fat in adult aex-5-depleted worms (Figure S4J). Notably, intestine-specific aex-5 knockdown mimicked these effects, but these features were absent in the knockdown control or BW-muscle-specific RNAi animals in both young and adult hermaphrodites (Figure S4K).

Cyp-33e1 and its human ortholog CYP2A6 are kinetically privileged first responders to HNE; however, HNE only partially inhibits oxidoreductase activity

Based on the outcomes above, we further investigated the three candidate proteins, cyp-33e1, aex-5, and asp-2, specifically in the context of localized electrophile-sensing capabilities. First, we used cell-based T-REX quantitative electrophile responsivity ranking assay,[23] to evaluate electrophile-sensing propensity of each protein in live cells. T-REX liberates HNE in the vicinity of a protein of interest (POI) and hence can quantitatively rank[8] HNE responsivities in live cells by assessing the fraction of HNE that covalently labels a specific POI prior to HNE irreversibly diffusing away from the POI (Figure S5A). T-REX is thus a particularly stringent and quantitative test of electrophile sensitivity. From these experiments, cyp-33e1 emerged to be the most HNE responsive of the three POIs (Figures 4A, S5B, and S5C). The human ortholog of cyp-33e1, CYP2A6, was also HNE responsive (Figure S5D), and PCSK1, the human ortholog of aex-5, was not (Figure S5E).

As cyp-33e1 emerged to be the most avid HNE sensor, and HNE sensing was conserved to its human ortholog, we focused on cyp-33e1. We subjected purified recombinant CYP2A6 to HNE and detected time-dependent labeling that saturated after ~150 s (Figure 4B). Thus, CYP2A6 reacts with HNE faster than several HNE sensors reported from other groups that we have studied *in vitro* previously.[7,62] However, the time to saturation was slower than some of the electrophile sensors that we have reported (e.g., Ube2V2[63]), although the conditions were admittedly different, rendering direct comparisons difficult.

Several studies implicate either inhibitory, simulatory, or no effects induced by HNE on various mammalian CYP P450 isozymes[64–68]: CYP2A6 has not previously been examined. Treatment of commercially available CYP2A6 with HNE demonstrated a minor impact on enzymatic activity that occurred at high HNE concentrations, $K_i \sim >200\ \mu M$ (Figures 4C and S5F). Given that an excess of HNE had a minor effect on CYP2A6 activity and that relatively low HNE concentrations *labeled* the enzyme, we proposed that there are at least two HNE-labeling events within CYP2A6: one occurs rapidly with little impact on activity (such an event would be detected by our profiling strategy, even though under these first-responder conditions, CYP2A6 would remain active), and the second event reduced activity. We have reported such scenarios previously.[13,62] However, we cannot exclude, at this juncture, the possibility that the second labeling event occurs due to isomerization/aggregation of the first labeled species.

Cyp-33e1 and its human ortholog CYP2A6 undergo electrophile sensing at two cysteines

Cysteine is the most kinetically privileged, among nucleophilic protein residues, in terms of reactivity against Michael-acceptor-based electrophiles, including HNE.[7] Cyp-33e1 harbors 2 cysteines, C439, a conserved Heme-iron-binding cysteine within the catalytic site (Figures 4D, S5G, and S5H), and C295, an off-active-site residue that based on homology modeling, resides in a loop bridging an α helix and a β sheet (Figure 4D). The human ortholog CYP2A6 houses 3 cysteines: C14 and C82, in addition to the conserved catalytic-site C439. Overlays of the available X-ray crystal structure of human CYP2A6

(C) Recombinant CYP2A6 was partially inactivated by HNE. Data (left) were fit by linear regression to derive reaction velocities, which were subsequently plotted against (HNE) (right) and fit to Morrison tight-binding equation: $v = V_o*(1-((((([E] + (K_i*(1 + ([S]/K_M))))-((([E] + [I] + (K_i*(1 + ([S]/K_M))))2)-4*[E]*[I])0.5))/(2*[E])))$. [I], HNE concentration; [E], CYP2A6 concentration; [S], 3-cyano coumarin concentration; for K_M, see Figure S5F. The Morrison K_i: 207.9 ± 35.4 μM. $n = 3$ for all conditions.
(D) Overlay of human CYP2A6 (gold) (PDB: 1Z10) and *C. elegans* cyp-33e1 (green) (homology model) in ribbon presentation and sequence logos for sequences flanking indicated cysteines, derived from 936 sequences (isoforms) integrating 38 metazoan species (WebLogo). Sequence alignment for 936 sequences was performed using Super5 algorithm in MUSCLE5.[61] C439, catalytically essential residue, is highly conserved. Almost all Cyps house at least one additional cysteine beyond C439. Note: C14 of CYP2A6 lies within the N-terminal signal peptide sequence, and the construct used for crystallization does not bear this sequence. Also see Figures S5G and S5H.
All data present mean ± SEM. Decision tree for statistical treatment in Methods S3.
See also Figure S5.

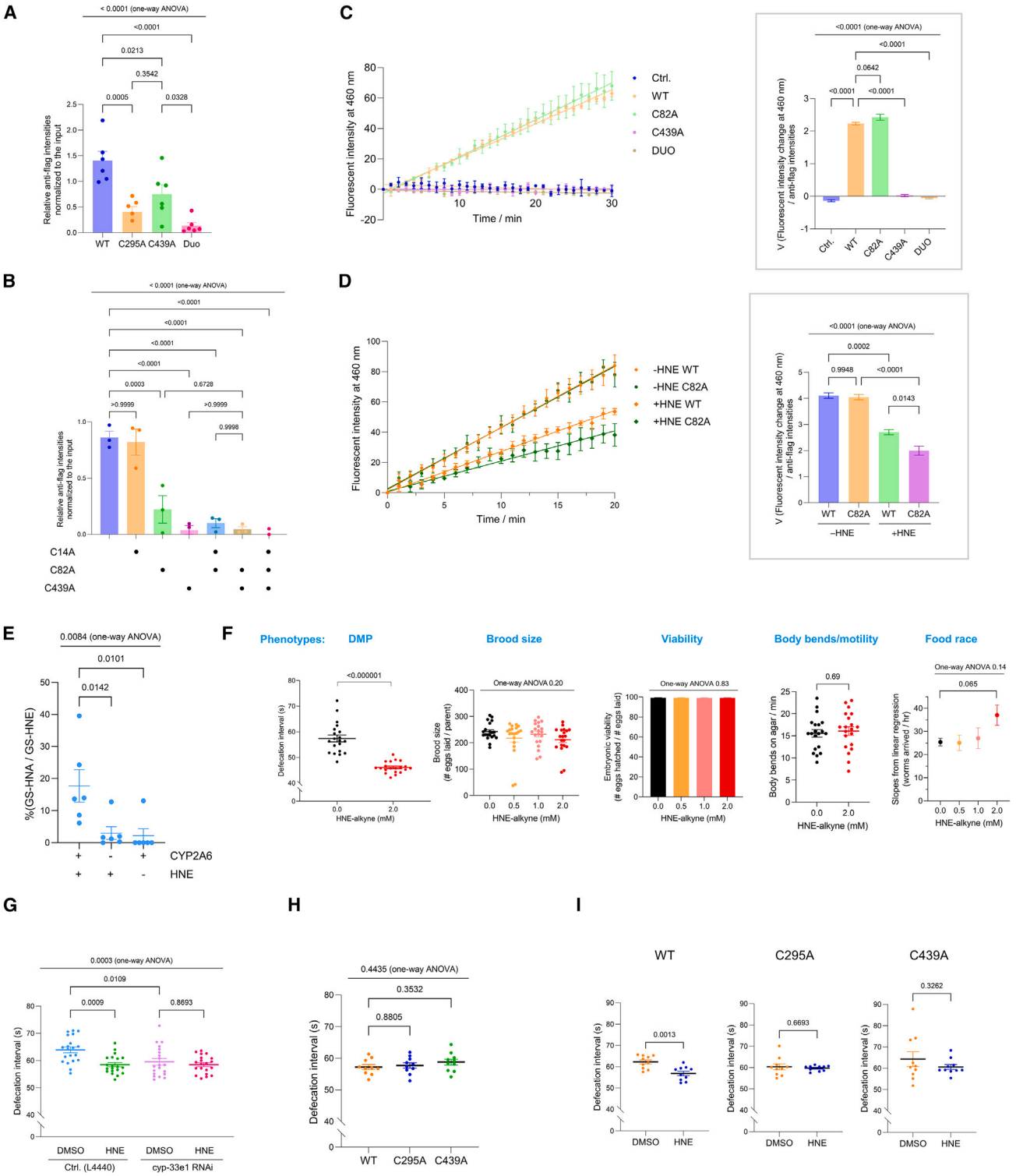

Figure 5. Cyp-33e1/CYP2A6, sense HNE at a conserved catalytic cysteine and an off-active-site cysteine; the former inhibits activity, yet labeling at both sites regulates stress-dependent changes in intestinal physiology

(A) Electrophile-sensing ability of cyp-33e1 WT, single, or double ("duo") cysteine-to-alanine mutants was quantitatively compared following T-REX in HEK293T (see Figure S5A) and click-biotin pull-down of HNEylated protein, as in Figure 4A. Plot shows quantification of Figure S6A. $n = 6$ for all conditions.

(B) Identical to (A) except electrophile-sensing ability of CYP2A6 WT, single, double, or triple cysteine-to-alanine mutants was quantitatively compared. Note: quantification takes into account of differences in WT/mutant expression. See also Figure S6B and Data S3C and S3D. $n = 3$ for all conditions.

(legend continued on next page)

(PDB: 1Z10) and a homology model of cyp-33e1 indicated that C82 and C295 in human and worm are located in different regions of the protein. C14 is not present in the worm protein (Figures 4D and S5G).

To delve deeper into underlying mechanisms and potential site specificity in sensing and inhibition, we created single, double, and where applicable, triple cysteine mutants of both human and nematode constructs and replicated HEK293T cell-based T-REX assays.[8,23] All mutants were expressed, although with variable expression levels (Figures S6A and S6B). Expression-level differences were subsequently taken into account in calculating ligand occupancy[8] for each POI, derived from T-REX (Figures 5A, 5B, S6A, and S6B).

In the *C. elegans* protein cyp-33e1, both single mutants intercepted HNE under T-REX (Figures 5A and S6A), indicating that C439 and C295 sense HNE. cyp-33e1(C295A, C439A) showed minimal labeling, indicating that these two cysteines account for the majority of HNE sensing. Likewise, C82 and C439 in CYP2A6 but not C14 were kinetically privileged sensing sites (Figures 5B and S6B). In parallel, mass-spectrometry-based site-specific modification analysis of CYP2A6, exposed to sub-micromolar HNE, revealed HNE-derived modification at C82 and C439 (Data S3C and S3D). No modification occurred at C14, consistent with T-REX (Figures 5A, 5B, S6A, and S6B). Thus, there are two HNE-sensing functions within cyp-33e1/CYP2A6: one occurs at a conserved active-site cysteine (C439), and the other occurs at a residue that has shifted during evolution ($C295^{worm}/C82^{human}$).

We next determined how each HNE-sensing site contributes to partial inhibition of oxidoreductase activity observed above (Figures 4C and S5F). Preparation of purified cyp-33e1 has not been previously reported. Despite numerous attempts, we were unable to isolate sufficient quantities of cyp-33e1 for enzymatic assays. However, we were able to purify human microsomal CYP2A6 WT and the 3 relevant mutants: C82A, C439A, and (C82A, C439A) double mutant, using HEK293+Hycell expression system (Figure S6C). Mutation of the catalytic-site cysteine, C439, rendered CYP2A6(C439A) and CYP2A6(C82A, C439A) inactive (Figures 5C and S6D). CYP2A6(C82A) exhibited activity similar to CYP2A6(WT) (Figures 5C and S6D). Under similar HNE dosage and treatment times as deployed for commercial CYP2A6(WT) above (Figure 4C), our in-house-expressed CYP2A6(WT) was inhibited (Figures 5D and S6E), similarly to what we observed for the commercial protein (Figure 4C). Under identical conditions, CYP2A6(C82A) was comparably sensitive to HNE (Figures 5D and S6E). These data affirm that partial suppression of oxidoreductase activity occurs through HNEylation at the conserved catalytic-site cysteine, C439.

HNE is also potentially a CYP2A6 substrate. Indeed, incubation of HNE with the enzyme in the presence of NADPH in an aerobic environment produced detectable amounts of HNA. When the enzyme was omitted from the same assay mixture, HNA production was insignificant compared with background control (i.e., in the absence of HNE) (Figure 5E; Data S3E). Thus, HNE in the active site of CYP2A6 undergoes partitioning between enzymatic oxidation and labeling the active site.

Cyp-33e1 is an essential mediator of intestinal physiology in both non-stressed and stressed states

We next used *CRISPR-cas9* technology to generate homozygous cyp-33e1(C295A) and cyp-33e1(C439A) knockin (KI) *C. elegans*. Following back-crossing into WT nematodes, each strain was validated by sequencing using single-worm PCR (Methods S2A–S2C). The KI animals grew comparably to WT worms. In parallel, we undertook a systematic quantitative assessment of *C. elegans* phenotypes to identify those most prominently affected by acute electrophilic stress (Figure 2E, path II). Between food race, body bends/minute, viability, brood size, and DMP cycles, DMP emerged to be most affected by acute HNE stress (Figure 5F). As DMP cycles in *C. elegans*

(C) Oxidoreductase activities measured for in-house generated CYP2A6 (WT or indicated single and double cys-to-ala mutants) were fit by linear regression (Ctrl: $y = -0.13*x + 3.26$; WT: $y = 2.23*x - 1.53$; C82A: $y = 2.25*x - 2.81$; C439A: $y = 0.021*x - 0.284$; DUO: $y = -0.0578*x - 0.777$), to derive reaction velocities. Background subtraction and normalization were applied to all datasets. Inset on right: quantification of relative slopes. Negative control denotes cells without transfection. See also Figures S6C and S6D. $n = 3$ for all conditions.

(D) Progress curve analyses of CYP2A6 (WT or C82A) enzymatic turnover, in the presence and absence of HNE (400 μM). Data were fit by linear regression (−HNE WT: $y = 4.11*x + 2.1$; −HNE C82A: $y = 4.05*x + 2.6$; +HNE WT: $y = 2.71*x + 0.16$; +HNE C82A: $y = 2.00*x + 0.95$). Background subtraction and normalization were applied to all datasets. Inset on right: quantification of the relative slopes. See also Figures S6C and S6E. $n = 3$ for all conditions.

(E) CYP2A6 in the presence of NADPH, and under aerobic conditions, produced measurable amount of acid metabolite, HNA, detected and quantified as a glutathione (GSH) adduct (termed, GS-HNA), against indicated controls (i.e., in the absence of CYP2A6, or HNE). Note: HNE can undergo inadvertent oxidation in the absence of CYP2A6, oftentimes resulting in aberrant background signals. Quantification here shows combined datasets across 6 independent biological replicates involving substrate concentrations indicated in Data S3E. y axis represents relative percent of GS-HNA detected over GS-HNE in each replicate. *p* values calculated by Dunnett's multiple comparisons test.

(F) Indicated phenotypic changes were quantitatively scored for day 1 adult worms following acute HNE stress (2 mM, 1 h). $n = 3$ for the food race, $n = 20$ for others.

(G) Average defecation motor program (DMP) intervals of day 1 adult worms, in response to electrophilic stress (HNE[alkyne], 2 mM, 1 h) vs. DMSO, in the presence of either cyp-33e1 RNAi or RNAi control (Ctrl, L4440). Each data point represents average value of 5 cycles from individual animals. *p* values calculated by Tukey's multiple comparisons test. See also Figures S6F–S6H and Videos S2, S3, S4, S5, S6, and S7. $n = 20$ for all conditions.

(H) Average DMP intervals of L4 worms (48 h after seeding to RNAi plates) (WT or cyp-33e1 mutant knockin), measured in the absence of DMSO or electrophilic stress. Each data point represents the 6–9 (average 7) cycles from individual animals. *p* values calculated by Dunnett's multiple comparisons test. See also Methods S1, Figure S6I, and Videos S8, S9, and S10. See Methods S2B and S2C for validations of knockin strains. $n = 10$ for all conditions.

(I) Average DMP intervals of day 1 adult worms (WT or cyp-33e1 mutant knockin), in response to HNE(alkyne) (2 mM, 1 h). Each datapoint represents 4–7 (average 6) cycles from individual animals. *p* values calculated by unpaired Students' t test. See also Methods S1, Figure S6J, and Videos S12, S13, S14, S15, and S16. See Methods S2B and S2C for validations of knockin strains. $n = 10$ for all conditions.

All data present mean ± SEM. Decision tree for statistical treatment in Methods S3.

See also Figure S6.

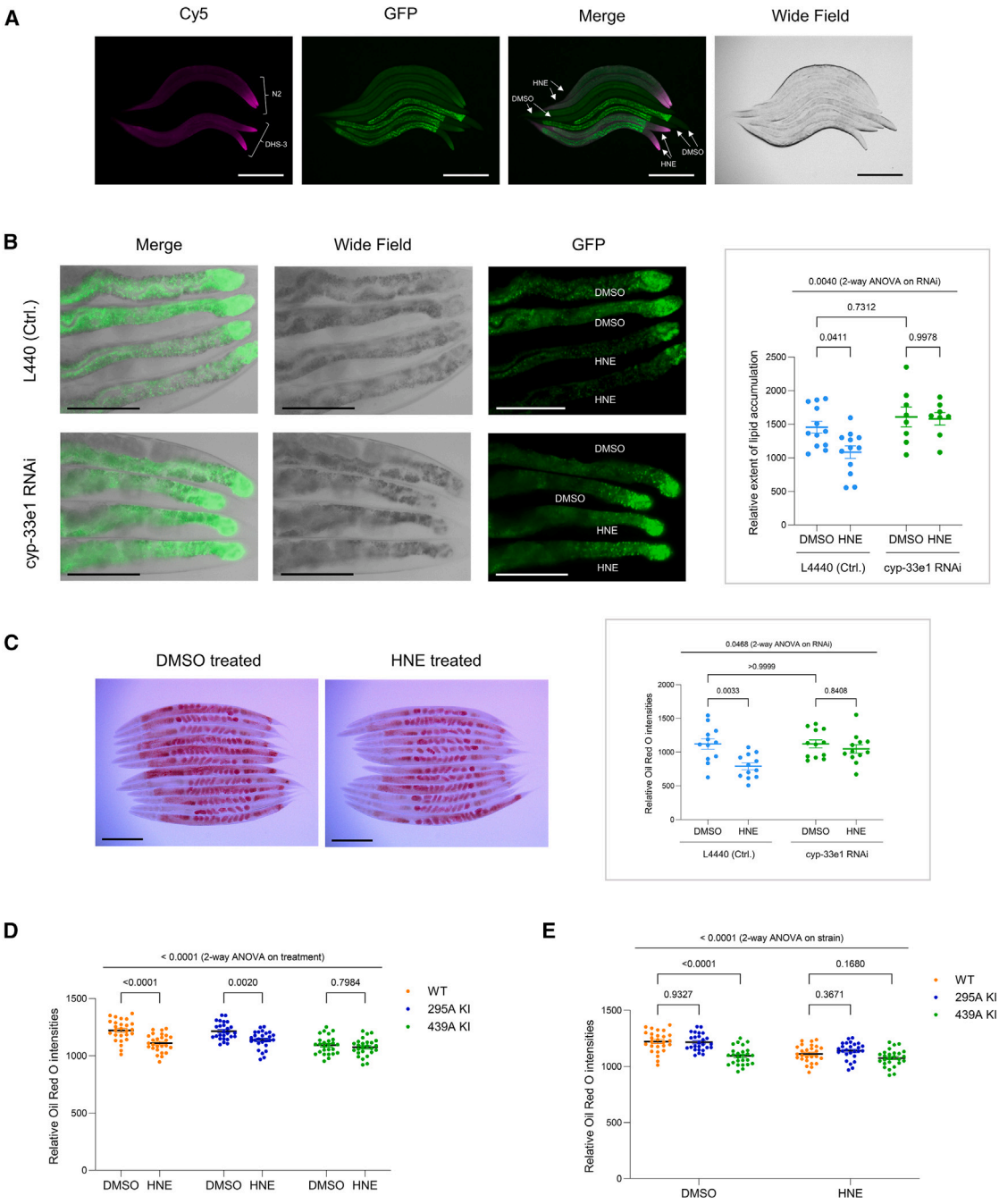

Figure 6. Electrophile stress disrupts lipid homeostasis: These effects are cyp-33e1—specifically, catalytic cysteine (C439)—dependent

(A) Click-Immunofluorescence imaging of paraformaldehyde-fixed animals showed effective uptake of alkyne-functionalized electrophile (following Click coupling with Cy5-azide), subsequent to whole-animal electrophile stimulation (HNE[alkyne] 2 mM, 1 h). 8 × L4-young adult hermaphrodites—4 × DHS-3::GFP reporter worms (key resources table), 4 × wild-type N2 worms for comparison—are shown. Note: elevated HNEylation in the head is likely due to preferential electrophile uptake with food. This issue was circumvented by the use of tissue-specific-Halo-targetable photocaged-HNE, see Figures S1C and S1D). Scale bar: 200 μm. See also Figure S6K.

(B) Acute electrophile stress (HNE[alkyne], 2 mM, 1 h) impairs lipid accumulation: cyp-33e1 deficiency ablates this phenotype. 4 × day 1 adult DHS-3::GFP hermaphrodites were aligned manually, post levamisole immobilization. Top 2 worms: DMSO treated; bottom 2 worms: electrophile treated. Representative posterior intestinal regions are shown. Scale bar: 100 μm. Inset: quantification derived from total intestinal GFP-signal intensity. *p* values calculated by Tukey's multiple comparisons test. *n* = 12 for L4440 (control) group. *n* = 8 for cyp-33e1 RNAi group.

(legend continued on next page)

also report on intestinal physiology[69] (Figure S6F; Video S1) and cyp-33e1 was mapped by OS-Localis-REX as a gut-responsive sensor (Figure 1D), we chose DMP to investigate the effects of altering cyp-33e1's electrophile responsivity on *C. elegans*.

Comprising three steps, DMP consists of highly coordinated periodic rhythms accurately quantifiable from real-time measurements. We first evaluated the effects of cyp-33e1 depletion on DMP. RNAi-control young adults underwent 63.7 ± 1.7 s intervals (Figures 5G and S6G; Videos S2 and S3), within the expected range for WT *C. elegans* at this age.[70] Cyp-33e1 depletion reduced DMP cycle length (Figure S6G; Video S3). Following whole-animal electrophile stimulation, DMP in control animals was significantly perturbed, reducing the mean cycle length to 58.5 ± 0.8 s (Figures 5G and S6H; Videos S4 and S5). Cyp-33e1-deficient animals did not undergo further reduction of cycle length following HNE treatment (Figures 5G and S6H; Videos S6 and S7). These results demonstrate that (1) cyp-33e1's electrophile-sensing activity plays a functional role in natural oscillations of DMP and likely overall gut homeostasis and that (2) HNE exerts its effect on DMP in a cyp-33e1-specific manner.

We subsequently compared changes in DMP cycles in cyp-33e1(C295A) and cyp-33e1(C439A) KI *C. elegans*, with and without acute HNE exposure. Neither KI strain showed a significant decrease in DMP (Figures 5H and S6I; Videos S8, S9, and S10). This result is in contrast to the decrease in defecation interval upon cyp-33e1 RNAi (Figures 5G, 1st vs. 3rd column and S6H; Videos S2 and S3). These data imply that changes in defecation interval in cyp-33e1 RNAi nematodes are not ascribable uniquely to loss of cyp-33e1 activity. Moreover, *both* KI strains emerged to be recalcitrant to HNE-induced reduction of DMP-cycle length observed in WT animals (Figures 5I and S6J; Videos S11, S12, S13, S14, S15, and S16). As cyp-33e1 RNAi and both KI strains are refractory to HNE-induced changes in DMP cycles (Figures 5G, 3rd and 4th columns and 5I), electrophile sensing by cyp-33e1 at *both* electrophile-sensing sites is important for reduction in defecation intervals during stress.

Electrophile stress promotes defects in lipid accumulation dependent on cyp-33e1 activity

HNE is a prototypical lipid-derived electrophile upregulated under physiological stress by non-enzymatic and enzymatic lipid peroxidation.[7] Fat metabolism defects are also correlated with DMP defects.[33] We thus next investigated the effect of HNE treatment on lipid storage. Using a lipid-droplet reporter strain[71] (DHS-3::GFP, Figure S6K; key resources table), HNE treatment depleted lipids (Figures 6A and 6B). cyp33e1-RNAi did not induce lipid depletion (Figure 6B, 1st vs. 3rd columns). However, cyp-33e1-RNAi worms were refractory to HNE-induced lipid-level changes (Figure 6B). ORO staining of control RNAi (WT N2) and the corresponding cyp-33e1-RNAi worms gave similar outcomes (Figures 6C and S6L). Thus, cyp-33e1-deficient animals marshall lipid-distribution responses to HNE differently from controls. However, cyp-33e1(C439A) KI animals were refractory to HNE-induced lipid depletion (Figures 6D, last two columns and S6M), whereas cyp-33e1(C295A) KI strain behaved similarly to WT (Figures 6D, first four columns and S6M). Indeed, cyp-33e1(C439A) KI strain exhibited reduced global lipid content even in non-stressed states (Figures 6E, compare within "DMSO" set and S6M), and cyp-33e1(C295A) KI strain exhibited similar lipid levels to WT *C. elegans* (Figures 6E, compare within DMSO set and S6M). The refractory nature of strains lacking active cyp-33e1 to HNE highlights the importance of cyp-33e1 activity in the maintenance of global lipid storage during stress. Altogether, differences between cyp-33e1(C439A) KI and cyp-33e1 RNAi backgrounds in the absence of exogenous HNE (Figure 6E, 1st and 3rd columns, vs. Figures 6B and 6C, 1st and 3rd columns) further demonstrate that there are regulatory modes of cyp-33e1 that are not dependent on activity. However, these modes of regulation are outside the remit of this study, as they are independent of HNE.

Cyp-33e1 oxidation of HNE triggers global lipid deficit

Since cyp-33e1 activity emerged to be crucial for HNE-induced lipid storage changes, we hypothesized that either reductive or oxidative metabolism of HNE, mediated by cyp-33e1, initiates lipid deficit. Given the simplicity of HNE, two main cyp-33e1-catalyzed metabolites are possible: HNA (oxidation) and DHN (reduction). Both metabolites were synthesized, and their homogeneity was characterized using NMR spectroscopy (Data S3F). Feeding RNAi-control nematodes with HNA but not DHN phenocopied HNE-induced lipid depletion in DHS-3::GFP lipid-reporter worms (Figures 7A, left set and S7A). In cyp-33e1-deficient reporter worms, HNE-stressed animals did not undergo changes in lipid accumulation (Figure 7A, right set), consistent with our data above (Figures 6B and 6C). In cyp-33e1-RNAi reporter worms, DHN had no effect (Figure 7A). However, HNA feeding to cyp-33e1-RNAi-fed worms caused lipid depletion (Figures 7A, right set and S7A). This observation was further validated by ORO staining (Figures S7B and S7C). These data are consistent with cyp-33e1 converting HNE to HNA, that directly interferes with lipid storage. Linking these data back to effects on DMP, HNA administration to WT N2 nematodes reduced defecation intervals similarly to HNE administration (Figure 7B; Videos S11, S12, and S16). Thus, cyp-33e1 activity on HNE produces HNA, which ushers lipid depletion that is likely important for HNE's effects on DMP activity.

(C) Oil red O staining validated lipid depletion, following acute electrophilic stress (HNE[alkyne], 2 mM, 1 h): 12 fixed day 1 adult worms were manually aligned. Scale bar: 200 μm. Inset: quantification. Signals were quantified by circling the entire animal except for the pharyngeal region. *p* values calculated by Tukey's multiple comparisons test. See also Figure S6L. *n* = 12 for all conditions.

(D) WT and indicated knockin mutant animals were subjected to the same conditions as (C). *p* values calculated by Šidak's multiple comparisons test. See also Figure S6M. *n* = 26 for all conditions.

(E) Results in (D) presented/analyzed with different groupings. *p* values calculated by Dunnett's multiple comparisons test. *n* = 26 for all conditions.

All data present mean ± SEM. Decision tree for statistical treatment in Methods S3.

See also Figure S6.

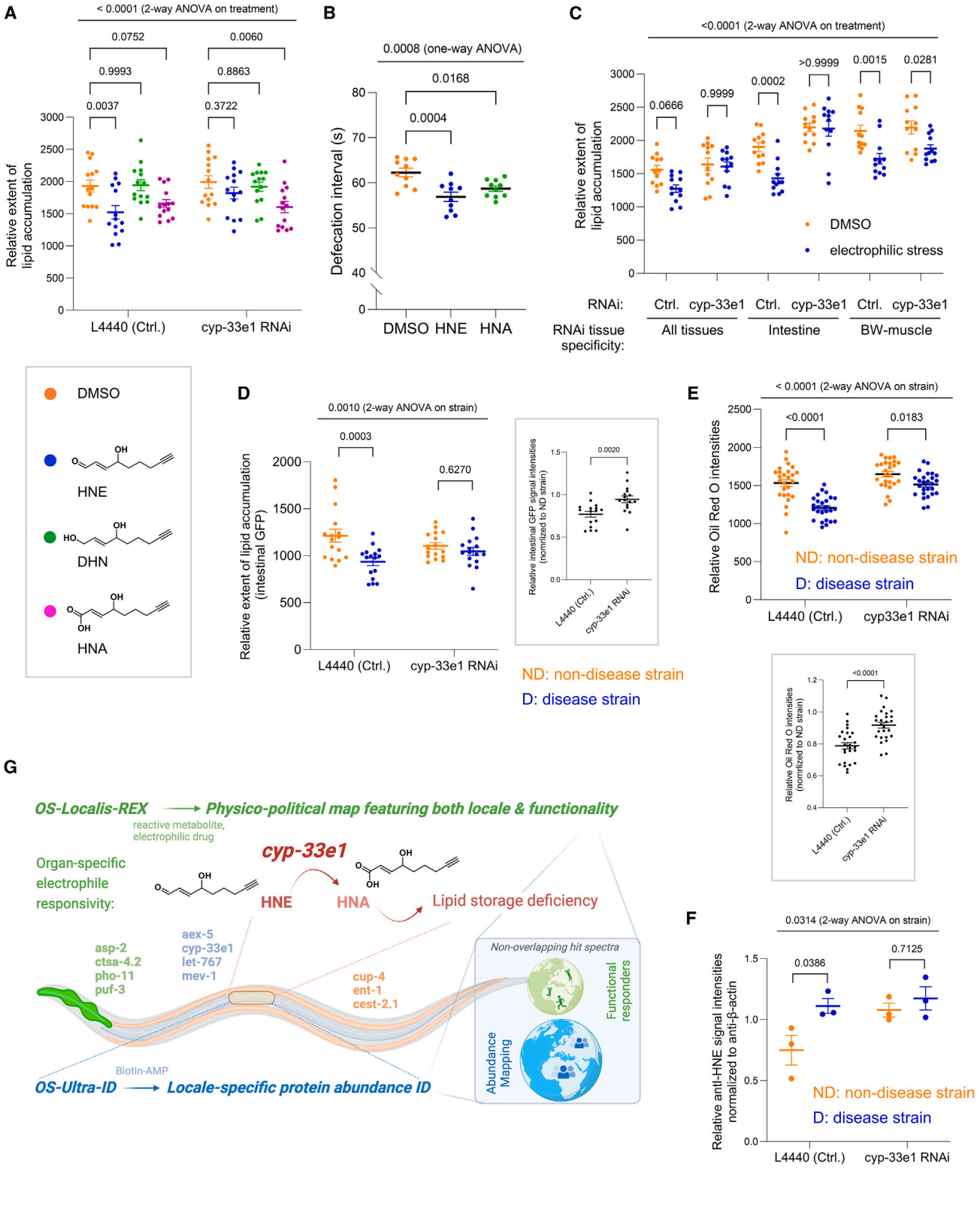

(legend on next page)

Tissue-specific electrophile responsivity of cyp-33e1

At this juncture, because cyp-33e1 is present in numerous locales at similar levels (Figure 1D), it remains unclear from our data to what extent cyp-33e1 activity must localize in the gut to exert its effect on lipid storage. We used tissue-specific RNAi[72] to address this question. We first generated and validated the strains necessary to execute tissue-specific gene silencing in either intestine or BW muscles (Methods S2D–S2G). Ubiquitous cyp-33e1 knockdown (Figure 7C, left set) reproduced our previous observations (Figure 7A, left set). BW-muscles-specific cyp-33e1 depletion did not block stress-induced lipid depletion (Figures 7C, left vs. middle sets and S7D). Intestine-targeted cyp-33e1-RNAi blocked lipid depletion (Figures 7C, left vs. right-most sets and S7D). Thus, HNE-induced lipid depletion is mediated by intestinal cyp-33e1.

Physiological significance of cyp-33e1 in animals with elevated endogenous stress

We exploited *C. elegans* harboring the transgene (unc-54p::Htt513(Q128)::YFP::unc-45 3′ UTR),[27–29,73] expressing YFP-tagged polyQ-expanded disease-associated fragment of human Hungtinton's disease (HD) protein Htt (key resources table). Endogenous HNE production and proteome HNEylation are upregulated in diseased animals compared with Htt513(Q15)-expressing non-disease animals. We crossed both strains into the DHS-3::GFP lipid reporter line (Methods S2H). Anti-HNE western blots confirmed elevated protein HNEylation, against age-matched healthy controls (Figure S7E, two left-hand lanes). Oxy-blot, a measure of overall protein carbonylation, showed minimal changes between diseased and control animals (Figure S7F). Thus, HNEylation is an operative stressor in diseased worms.

The resulting double transgenic lines showed hallmarks of Htt513 aggregation only in diseased worms (Figure S7G). Comparison of lipid-droplet levels in these two strains when treated with control RNAi showed that there was a depletion of lipid droplets in diseased strain compared with the control strain (Figures 7D and S7H, top). There was no difference between these strains when they were treated with cyp-33e1 RNAi (Figures 7D and S7H, bottom). Similar data were obtained with ORO staining (Figures 7E and S7I), although in this instance, cyp-33e1-RNAi caused an increase in lipid accumulation selectively in the diseased strain (Figure 7E, compare 2nd and 4th columns). This observation further reinforces the importance of cyp-33e1 activity in HNE-induced depletion of lipid accumulation. To determine if these outcomes could be explained simply by total protein HNEylation, we examined HNEylation in these backgrounds. Following cyp-33e1 RNAi, the difference in the extent of HNEylation between diseased and healthy animals was no longer apparent (Figures 7F and S7E, two right-hand lanes). Thus, proteome HNEylation is not correlated with changes in lipid storage, and the activity of cyp-33e1 is correlated with such changes.

DISCUSSION

Several lines of evidence indicate that our spatiotemporal and *functional* proteomics approach identified genuine locale-specific responders. First, hits were not dominated by expression: in several instances, reported[20] and our own tissue-specific expression datasets indicated that proteins sensed electrophiles in locales where they were of reduced expression than other locales investigated. Second, and no less remarkably, our hit proteins did not gravitate to locale-indiscriminate electrophile responders, indicating that OS-Localis-REX is indeed able to undertake OS actionability profiling, surmounting issues that have to date hindered development of *functionally annotated* maps. These results further point to there being significant context dependence among chemically actionable proteins across organs. These observations could reflect changes in

Figure 7. cyp-33e1 HNE sensing generates a metabolite (HNA) that promotes lipid depletion; similar results are found in diseased models with heightened endogenous HNE stress

(A) Administration of HNA, an enzymatic product of cyp-33e1, phenocopied HNE-induced lipid depletion in the wild-type (L4440, Ctrl.) animals and maintained this phenotype in the presence of cyp-33e1 RNAi. *p* values calculated by Dunnett's multiple comparisons test. See also Figure S7A. Inset: chemical structures of small molecules. See Figures S7B and S7C for results obtained using an orthogonal oil red O staining. $n = 14$ for all conditions.

(B) Average DMP intervals of live worms (WT, or indicated cyp-33e1 mutant knockin), following HNE(alkyne) (2 mM, 1 h) treatment. Each data point represents 4–7 (average 6) cycles from individual animals. *p* values calculated by Dunnett's multiple comparisons test. Data from first 2 columns are replicas of the first 2 columns within Figure 5H. See also Videos S11, S12, and S17. $n = 10$ for all conditions.

(C) Despite similar abundance of cyp-33e1 in both intestine and BW-muscle tissues (Figure 1D), BW-muscle-specific depletion of cyp-33e1 failed to block stress-induced lipid depletion, observed during ubiquitous and intestine-specific cyp-33e1 knockdown. Ctrl: control RNAi. *p* values calculated by Šídák's multiple comparisons test. See also Figure S7D and Methods S2D–S2G. $n = 12$ for all conditions.

(D) Quantification of relative lipid-droplet extent in indicated diseased (D) and non-diseased (ND) animals. See also Figures S7G and S7H and key resources table. *p* values calculated by Šídák's multiple comparisons test. Inset shows comparison between fold change in ND vs. D strains for control and cyp-33e1 RNAi worms. $n = 16$ for all conditions.

(E) Similar to (D) but deployed oil red O staining. *p* values calculated by Šídák's multiple comparisons test. See also Figure S7I. Inset (bottom) shows a comparison between fold change in ND vs. D strains for control and cyp-33e1 RNAi worms. $n = 26$ for all conditions.

(F) Quantification of the extent of HNEylated proteomes in D vs. ND animals subjected to cyp-33e1 RNAi or L4440 (Ctrl.) RNAi. *p* values calculated by Šídák's multiple comparisons test. See also Figures S7E and S7F. $n = 3$ for all conditions.

(G) A combination of profiling electrophile responders (using organ-specific precision localized electrophile generation [OS-Localis-REX]) and mechanistic investigations, provides a detailed annotated map of *chemically actionable* targets within specific organs in *C. elegans*. Inset (bottom right) shows effectively non-overlapping target spectra between OS-Localis-REX and OS-Ultra-ID (organ-specific mapping of localized protein abundance, performed in the same 3 organs as in OS-Localis-REX).

All data present mean ± SEM. Decision tree for statistical treatment in Methods S3.

See also Figure S7.

responder proteins' interactomes, locales, modifications, or other context-dependent regulatory nuances across tissues. All the above information is indeed difficult to extract by other proteomics/sequencing methods, including APEX and, as shown here, OS-Ultra-ID. Clearly, as our own data with OS-Ultra-ID-expressing worms show, OS-Localis-REX cannot replace the power of such methods to identify locale-specific proteomes because it is blind to proteins that have little chemical function. Hence OS-Localis-REX is complementary to existing profiling methods. However, as we outline in the introduction, it is often functionality or actionability that constitutes the most important parameters. Moreover, with an expanding toolset of proto-electrophiles applicable to REX technologies, a wealth of activities can be probed using the same approach, likely extending the possibilities of finding locale-specific actionable proteins.

Our investigations into the role of context-dependent responders uncovered several known and yet-unknown phenotypic effects associated with OS-Localis-REX hits. Several were also interestingly linked to electrophile-induced effects on egg-laying rate. Such phenotypic changes in electrophile response are, we submit, compelling evidence that OS-Localis-REX functionally annotated maps report on validated stress responders whose electrophile engagement is linked to how worms manage electrophilic challenges.

One specific responder, cyp-33e1, stood out. Subsequent mechanistic examinations documented that this metabolic enzyme manifests context-dependent roles in regulating gut health and response to electrophilic stress. cyp-33e1 thus emerged to be responsible for converting HNE to a signal, acid metabolite (HNA), ushering lipid deficit. This behavior is not positively linked to cyp-33e1 HNEylation (it is antagonistic, *in vitro*). These results demonstrate that OS-Localis-REX has the power to identify proteins that are metabolically active against specific electrophiles, providing that there is partitioning between metabolism and labeling.

Overall, this result adds an unexpected dimension to our profiling data and further underscores the ability of OS-Localis-REX to decode cellular signaling pathways enacted by enzymatic processes and their specific products at the tissue-specific level. This is far from a trivial discovery. Cyp-isoform-induced sensitization of molecules causing toxicity and disease, such as cancer, is well known. This occurs, for instance, in drug metabolism[65] and inadvertent toxification of xenobiotics, e.g., methanol (acidosis) and benzene (alkylation). However, several cyp-isoforms are also involved in reactive small-molecule signaling pathways, not unakin to what we delineate here. Such pathways in mammals, from where the majority of these data are derived, include CYP1–4 families that metabolize eicosanoids. Regulatory loops for other CYP family enzymes have been proposed[74]: e.g., several CYP enzymes, including CYP26 family enzymes, metabolize all *trans* retinoic acid.[75] It is interesting to note that retinoic acid is an important regulator of hepatic lipid homeostasis.[75,76] It is thus tempting to propose that CYP metabolism of lipophilic entities may form regulatory loops controlling lipid storage and hence regulate response to stresses that are *broadly* conserved across taxa. Unfortunately, despite reports of several *C. elegans* cyp enzymes performing lipid-metabolism roles,[77] precise molecular and pathway details are lacking. As we demonstrate here, localized reactive-lipid generation may be one way to progress in this area.

Limitations of the study

As noted above, OS-Localis-REX is blind to total protein levels in specific tissues. For the moment, at least, locale-specific abundance is admittedly the most commonly used parameter, although this study and previous work[13] question and caution the overall utility in inferring function from locale-specific abundance. Combination of OS-Ultra-ID with OS-Localis-REX is perhaps an ideal solution to this issue, as we demonstrate here. Moreover, as the electrophile released during OS-Localis-REX is relatively low concentration, our hits are limited to the very best responders. It is possible that modification of the REX protocols[23,24] may enable more depth to be achieved in a single experiment, without resorting to using a fleet of photocaged electrophiles.

At the biochemical level, we cede that how HNA functions to reduce lipid droplets remains to be defined. Likely this molecule interacts with (a) lipid receptor(s). However, as HNA is a non-reactive molecule, it is not applicable to REX technologies, and indeed, overall methods to study such interactomes are lacking. HNA befited with photo-crosslinkers and similar strategies are quite likely to be of use to achieve this goal but are outside the scope of this study.

Bearing these limitations in mind, subsequent work investigating such behaviors, and indeed profiling other tissues, will help establish a more detailed understanding of how locale-specific responders vary across worms. Similar profiling experiments across other organisms will bring further insights that can be compared across organisms/expression patterns to give a selective comprehensive lens into actionable protein targets against the local proteome noise.

RESOURCE AVAILABILITY

Lead contact

All unique materials will be made available upon reasonable request to the lead contact, Yimon Aye (yimon.aye@chem.ox.ac.uk).

Materials availability

The extrachromosomal and integrant *C. elegans* strains generated in this study (key resources table) are being distributed to Caenorhabditis Genetics Center (CGC): https://cgc.umn.edu/. All recombinant DNA generated in this study (key resources table) are being distributed to Addgene: https://www.addgene.org/. Further information and requests for resources and reagents should be directed to the lead contact.

Data and code availability

Proteomics data that support the findings of this study include the following: PRIDE ProteomeXchange identifier numbers are PRIDE: PXD027730 (TMT OS electrophile-responder analysis in OS-Localis-REX strains, Figures 1C and 1D; Data S1 and S2), PRIDE: PXD052114 (TMT OS abundance analysis in OS-Ultra-ID strains, Figures 2B–2D; Data S5), and PRIDE: PXD052493 (label-free quantification [LFQ] whole-proteome analysis in OS-Ultra-ID strains, Figure S2B; Data S4). See also Mendeley Data: http://www.doi.org/10.17632/4gyvt94vnm.1.

ACKNOWLEDGMENTS

We thank Drs. Krishna Tripathi, Kevin Fridianto, and Chaosheng Luo (Aye lab) for photocaged-electrophile probe synthesis; Prof. Pierre Gönczy and Ms. Coralie Busso (EPFL-SV) for RNAi clones (Ahringer's library); and

Prof. Mario de Bono and Ms. Ekaterina Lashmanova (IST:Austria) for the MG1655:BioBKan strain. Research was funded by the European Research Council (ERC) grant (project no. 101043303), which was funded by the State Secretairat for Education, Research, and Innovation (SERI) Switzerland (Y.A.) (2023–present); Swiss National Science Foundation (SNSF) project funding (310030_184729) (Y.A.) (2019–2023); SNSF R-Equip (Y.A.) for EPFL proteomics facility instrumentation (2023); the SNSF NCCR master program (J.L.) (2019); and the Novartis Foundation (M.J.C.L.).

AUTHOR CONTRIBUTIONS

J.L.: performed all experiments (except photocaged-electrophile synthesis and transgenic/KI worm generations), data analysis, compilation of figures, legends, and methods; A.K.: collaborated with J.L. on phenotypic assays and RNAi validations involving initial 15 genes; Y.-Q.G.: collaborated with J.L. on phenotypic assays, MS validations of protein modification, small-molecule MS analysis, and compilation of methods; D.A.U.: initial development of *C. elegans* Localis-REX workflows; R.H.: collaborated with J.L. and Y.A. on TMT-proteomics experiments and with J.L., Y.-Q.G., and Y.A. on MS-PTM mapping. B.Á.N.: collaborated with J.L. and A.K. on phenotypic assays involving the initial 15 genes; M.J.C.L.: experimental design and data analysis and writing (manuscript critical review and editing); Y.A.: conceptualization, project development and administration, experimental design and data analysis, writing (manuscript critical review and editing), supervision, and funding acquisition. All authors assisted with manuscript final proofing.

DECLARATION OF INTERESTS

The authors declare no competing interests.

STAR★METHODS

Detailed methods are provided in the online version of this paper and include the following:

SUPPLEMENTAL INFORMATION

Supplemental information can be found online at https://doi.org/10.1016/j.cell.2024.10.014.

Received: June 12, 2023
Revised: May 30, 2024
Accepted: October 10, 2024
Published: November 5, 2024

REFERENCES

1. Qin, W., Cho, K.F., Cavanagh, P.E., and Ting, A.Y. (2021). Deciphering molecular interactions by proximity labeling. Nat. Methods *18*, 133–143. https://doi.org/10.1038/s41592-020-01010-5.
2. Scorrano, L., De Matteis, M.A., Emr, S., Giordano, F., Hajnóczky, G., Kornmann, B., Lackner, L.L., Levine, T.P., Pellegrini, L., Reinisch, K., et al. (2019). Coming together to define membrane contact sites. Nat. Commun. *10*, 1287. https://doi.org/10.1038/s41467-019-09253-3.
3. Geri, J.B., Oakley, J.V., Reyes-Robles, T., Wang, T., McCarver, S.J., White, C.H., Rodriguez-Rivera, F.P., Parker, D.L., Jr., Hett, E.C., Fadeyi, O.O., et al. (2020). Microenvironment mapping via Dexter energy transfer on immune cells. Science *367*, 1091–1097. https://doi.org/10.1126/science.aay4106.
4. Lin, Z., Schaefer, K., Lui, I., Yao, Z., Fossati, A., Swaney, D.L., Palar, A., Sali, A., and Wells, J.A. (2024). Multiscale photocatalytic proximity labeling reveals cell surface neighbors on and between cells. Science *385*, eadl5763. https://doi.org/10.1126/science.adl5763.
5. Alvarez-Castelao, B., Schanzenbächer, C.T., Hanus, C., Glock, C., tom Dieck, S., Dörrbaum, A.R., Bartnik, I., Nassim-Assir, B., Ciirdaeva, E., Mueller, A., et al. (2017). Cell-type-specific metabolic labeling of nascent proteomes in vivo. Nat. Biotechnol. *35*, 1196–1201. https://doi.org/10.1038/nbt.4016.
6. Yuet, K.P., Doma, M.K., Ngo, J.T., Sweredoski, M.J., Graham, R.L.J., Moradian, A., Hess, S., Schuman, E.M., Sternberg, P.W., and Tirrell, D.A. (2015). Cell-specific proteomic analysis in *Caenorhabditis elegans*. Proc. Natl. Acad. Sci. USA *112*, 2705–2710. https://doi.org/10.1073/pnas.1421567112.
7. Parvez, S., Long, M.J.C., Poganik, J.R., and Aye, Y. (2018). Redox signaling by reactive electrophiles and oxidants. Chem. Rev. *118*, 8798–8888. https://doi.org/10.1021/acs.chemrev.7b00698.
8. Long, M.J.C., Rogg, C., and Aye, Y. (2021). An oculus to profile and probe target engagement in vivo: How T-REX Was Born and its evolution into G-REX. Acc. Chem. Res. *54*, 618–631. https://doi.org/10.1021/acs.accounts.0c00537.
9. Bollong, M.J., Lee, G., Coukos, J.S., Yun, H., Zambaldo, C., Chang, J.W., Chin, E.N., Ahmad, I., Chatterjee, A.K., Lairson, L.L., et al. (2018). A metabolite-derived protein modification integrates glycolysis with KEAP1–NRF2 signalling. Nature *562*, 600–604. https://doi.org/10.1038/s41586-018-0622-0.
10. Kulkarni, R.A., Bak, D.W., Wei, D., Bergholtz, S.E., Briney, C.A., Shrimp, J.H., Alpsoy, A., Thorpe, A.L., Bavari, A.E., Crooks, D.R., et al. (2019). A chemoproteomic portrait of the oncometabolite fumarate. Nat. Chem. Biol. *15*, 391–400. https://doi.org/10.1038/s41589-018-0217-y.
11. Pham, V.N., Bruemmer, K.J., Toh, J.D.W., Ge, E.J., Tenney, L., Ward, C.C., Dingler, F.A., Millington, C.L., Garcia-Prieto, C.A., Pulos-Holmes, M.C., et al. (2023). Formaldehyde regulates S-adenosylmethionine

biosynthesis and one-carbon metabolism. Science *382*, eabp9201. https://doi.org/10.1126/science.abp9201.

12. Long, M.J.C., Parvez, S., Zhao, Y., Surya, S.L., Wang, Y., Zhang, S., and Aye, Y. (2017). Akt3 is a privileged first responder in isozyme-specific electrophile response. Nat. Chem. Biol. *13*, 333–338. https://doi.org/10.1038/nchembio.2284.
13. Zhao, Y., Miranda Herrera, P.A., Chang, D., Hamelin, R., Long, M.J.C., and Aye, Y. (2022). Function-guided proximity mapping unveils electrophilic-metabolite sensing by proteins not present in their canonical locales. Proc. Natl. Acad. Sci. USA *119*, e2120687119. https://doi.org/10.1073/pnas.2120687119.
14. Poganik, J.R., Huang, K.T., Parvez, S., Zhao, Y., Raja, S., Long, M.J.C., and Aye, Y. (2021). Wdr1 and cofilin are necessary mediators of immune-cell-specific apoptosis triggered by Tecfidera. Nat. Commun. *12*, 5736. https://doi.org/10.1038/s41467-021-25466-x.
15. Liu, X., Long, M.J.C., Hopkins, B.D., Luo, C., Wang, L., and Aye, Y. (2020). Precision targeting of pten-null triple-negative breast tumors guided by electrophilic metabolite sensing. ACS Cent. Sci. *6*, 892–902. https://doi.org/10.1021/acscentsci.9b00893.
16. Gersch, M., Kreuzer, J., and Sieber, S.A. (2012). Electrophilic natural products and their biological targets. Nat. Prod. Rep. *29*, 659–682. https://doi.org/10.1039/c2np20012k.
17. Visscher, M., Arkin, M.R., and Dansen, T.B. (2016). Covalent targeting of acquired cysteines in cancer. Curr. Opin. Chem. Biol. *30*, 61–67. https://doi.org/10.1016/j.cbpa.2015.11.004.
18. Zheng, Q., Peacock, D.M., and Shokat, K.M. (2022). Drugging the next undruggable KRAS allele-Gly12Asp. J. Med. Chem. *65*, 3119–3122. https://doi.org/10.1021/acs.jmedchem.2c00099.
19. Long, M.J.C., and Aye, Y. (2017). Privileged electrophile sensors: A resource for covalent drug development. Cell Chem. Biol. *24*, 787–800. https://doi.org/10.1016/j.chembiol.2017.05.023.
20. Cao, J., Packer, J.S., Ramani, V., Cusanovich, D.A., Huynh, C., Daza, R., Qiu, X., Lee, C., Furlan, S.N., Steemers, F.J., et al. (2017). Comprehensive single-cell transcriptional profiling of a multicellular organism. Science *357*, 661–667. https://doi.org/10.1126/science.aam8940.
21. Kubitz, L., Bitsch, S., Zhao, X., Schmitt, K., Deweid, L., Roehrig, A., Barazzone, E.C., Valerius, O., Kolmar, H., and Béthune, J. (2022). Engineering of ultraID, a compact and hyperactive enzyme for proximity-dependent biotinylation in living cells. Commun. Biol. *5*, 657. https://doi.org/10.1038/s42003-022-03604-5.
22. Long, M.J.C., and Aye, Y. (2024). Climbing into their skin to understand contextual protein–protein associations and localizations: functional investigations in transgenic live model organisms. ChemBioChem (EFMC special collection). Chembiochem *25*, e202400005. https://doi.org/10.1002/cbic.202400005.
23. Parvez, S., Long, M.J.C., Lin, H.-Y., Zhao, Y., Haegele, J.A., Pham, V.N., Lee, D.K., and Aye, Y. (2016). T-REX on-demand redox targeting in live cells. Nat. Protoc. *11*, 2328–2356. https://doi.org/10.1038/nprot.2016.114.
24. Huang, K.T., Poganik, J.R., Parvez, S., Raja, S., Miller, B., Long, M.J.C., Fetcho, J.R., and Aye, Y. (2023). Z-REX: shepherding reactive electrophiles to specific proteins expressed tissue specifically or ubiquitously, and recording the resultant functional electrophile-induced redox responses in larval fish. Nat. Protoc. *18*, 1379–1415. https://doi.org/10.1038/s41596-023-00809-8.
25. Sies, H., Belousov, V.V., Chandel, N.S., Davies, M.J., Jones, D.P., Mann, G.E., Murphy, M.P., Yamamoto, M., and Winterbourn, C. (2022). Defining roles of specific reactive oxygen species (ROS) in cell biology and physiology. Nat. Rev. Mol. Cell Biol. *23*, 499–515. https://doi.org/10.1038/s41580-022-00456-z.
26. Dalleau, S., Baradat, M., Guéraud, F., and Huc, L. (2013). Cell death and diseases related to oxidative stress:4-hydroxynonenal (HNE) in the balance. Cell Death Differ. *20*, 1615–1630. https://doi.org/10.1038/cdd.2013.138.
27. Markaki, M., and Tavernarakis, N. (2020). Caenorhabditis elegans as a model system for human diseases. Curr. Opin. Biotechnol. *63*, 118–125. https://doi.org/10.1016/j.copbio.2019.12.011.
28. Silverman, G.A., Luke, C.J., Bhatia, S.R., Long, O.S., Vetica, A.C., Perlmutter, D.H., and Pak, S.C. (2009). Modeling molecular and cellular aspects of human disease using the nematode Caenorhabditis elegans. Pediatr. Res. *65*, 10–18. https://doi.org/10.1203/PDR.0b013e31819009b0.
29. Kim, D.-K., Kim, T.H., and Lee, S.-J. (2016). Mechanisms of aging-related proteinopathies in Caenorhabditis elegans. Exp. Mol. Med. *48*, e263. https://doi.org/10.1038/emm.2016.109.
30. Van Hall-Beauvais, A., Zhao, Y., Urul, D.A., Long, M.J.C., and Aye, Y. (2018). Single-protein-specific redox targeting in live mammalian cells and C. elegans. Curr. Protoc. Chem. Biol. *10*, e43. https://doi.org/10.1002/cpch.43.
31. Li, J., Van Vranken, J.G., Pontano Vaites, L., Schweppe, D.K., Huttlin, E.L., Etienne, C., Nandhikonda, P., Viner, R., Robitaille, A.M., Thompson, A.H., et al. (2020). TMTpro reagents: a set of isobaric labeling mass tags enables simultaneous proteome-wide measurements across 16 samples. Nat. Methods *17*, 399–404. https://doi.org/10.1038/s41592-020-0781-4.
32. Mahoney, T.R., Luo, S., Round, E.K., Brauner, M., Gottschalk, A., Thomas, J.H., and Nonet, M.L. (2008). Intestinal signaling to GABAergic neurons regulates a rhythmic behavior in *Caenorhabditis elegans*. Proc. Natl. Acad. Sci. USA *105*, 16350–16355. https://doi.org/10.1073/pnas.0803617105.
33. Sheng, M., Hosseinzadeh, A., Muralidharan, S.V., Gaur, R., Selstam, E., and Tuck, S. (2015). Aberrant fat metabolism in Caenorhabditis elegans mutants with defects in the defecation motor program. PLoS One *10*, e0124515. https://doi.org/10.1371/journal.pone.0124515.
34. Ammar, C., Schessner, J.P., Willems, S., Michaelis, A.C., and Mann, M. (2023). Accurate label-free quantification by directLFQ to compare unlimited numbers of proteomes. Mol. Cell. Proteomics *22*, 100581. https://doi.org/10.1016/j.mcpro.2023.100581.
35. Artan, M., Barratt, S., Flynn, S.M., Begum, F., Skehel, M., Nicolas, A., and de Bono, M. (2021). Interactome analysis of Caenorhabditis elegans synapses by TurboID-based proximity labeling. J. Biol. Chem. *297*, 101094. https://doi.org/10.1016/j.jbc.2021.101094.
36. Reimand, J., Isserlin, R., Voisin, V., Kucera, M., Tannus-Lopes, C., Rostamianfar, A., Wadi, L., Meyer, M., Wong, J., Xu, C., et al. (2019). Pathway enrichment analysis and visualization of omics data using g:profiler, GSEA, cytoscape and EnrichmentMap. Nat. Protoc. *14*, 482–517. https://doi.org/10.1038/s41596-018-0103-9.
37. Fraser, A.G., Kamath, R.S., Zipperlen, P., Martinez-Campos, M., Sohrmann, M., and Ahringer, J. (2000). Functional genomic analysis of C. elegans chromosome I by systematic RNA interference. Nature *408*, 325–330. https://doi.org/10.1038/35042517.
38. Calixto, A., Chelur, D., Topalidou, I., Chen, X., and Chalfie, M. (2010). Enhanced neuronal RNAi in C. elegans using SID-1. Nat. Methods *7*, 554–559. https://doi.org/10.1038/nmeth.1463.
39. Entchev, E.V., Schwudke, D., Zagoriy, V., Matyash, V., Bogdanova, A., Habermann, B., Zhu, L., Shevchenko, A., and Kurzchalia, T.V. (2008). LET-767 is required for the production of branched chain and long chain fatty acids in Caenorhabditis elegans. J. Biol. Chem. *283*, 17550–17560. https://doi.org/10.1074/jbc.M800965200.
40. Kuervers, L.M., Jones, C.L., O'Neil, N.J., and Baillie, D.L. (2003). The sterol modifying enzyme LET-767 is essential for growth, reproduction and development in Caenorhabditis elegans. Mol. Genet. Genomics *270*, 121–131. https://doi.org/10.1007/s00438-003-0900-9.
41. Kamath, R.S., Fraser, A.G., Dong, Y., Poulin, G., Durbin, R., Gotta, M., Kanapin, A., Le Bot, N., Moreno, S., Sohrmann, M., et al. (2003). Systematic functional analysis of the Caenorhabditis elegans genome using RNAi. Nature *421*, 231–237. https://doi.org/10.1038/nature01278.

42. Singh, J., and Aballay, A. (2019). Microbial colonization activates an immune fight-and-flight response via neuroendocrine signaling. Dev. Cell *49*, 89–99.e4.

43. Rasulova, M.F., Shanmugam, N., and Braeckman, B.P. (2012). The aging lysosome of *Caenorhabditis elegans*. Published Thesis (Department of Nematology, Ghent University Faculty of Sciences).

44. Kopp, F., Elguindy, M.M., Yalvac, M.E., Zhang, H., Chen, B., Gillett, F.A., Lee, S., Sivakumar, S., Yu, H., Xie, Y., et al. (2019). PUMILIO hyperactivity drives premature aging of Norad-deficient mice. eLife *8*, e42650. https://doi.org/10.7554/eLife.42650.

45. Zhou, K.I., Pincus, Z., and Slack, F.J. (2011). Longevity and stress in Caenorhabditis elegans. Aging (Albany, NY) *3*, 733–753. https://doi.org/10.18632/aging.100367.

46. Mengwasser, J., Babes, L., Cordes, S., Mertlitz, S., Riesner, K., Shi, Y., McGearey, A., Kalupa, M., Reinheckel, T., and Penack, O. (2017). Cathepsin E deficiency ameliorates graft-versus-host disease and modifies dendritic cell motility. Front. Immunol. *8*, 203. https://doi.org/10.3389/fimmu.2017.00203.

47. Lutz, D., Wolters-Eisfeld, G., Schachner, M., and Kleene, R. (2014). Cathepsin E generates a SUMOylated intracellular fragment of the cell adhesion molecule L1 to promote neuronal and Schwann cell migration as well as myelination. J. Neurochem. *128*, 713–724. https://doi.org/10.1111/jnc.12473.

48. Bardella, C., Pollard, P.J., and Tomlinson, I. (2011). SDH mutations in cancer. Biochim. Biophys. Acta *1807*, 1432–1443. https://doi.org/10.1016/j.bbabio.2011.07.003.

49. Evenepoel, L., Papathomas, T.G., Krol, N., Korpershoek, E., de Krijger, R.R., Persu, A., and Dinjens, W.N.M. (2015). Toward an improved definition of the genetic and tumor spectrum associated with SDH germ-line mutations. Genet. Med. *17*, 610–620. https://doi.org/10.1038/gim.2014.162.

50. Xu, C., Hwang, W., Jeong, D.E., Ryu, Y., Ha, C.M., Lee, S.V., Liu, L., and He, Z.M. (2018). Genetic inhibition of an ATP synthase subunit extends lifespan in C. elegans. Sci. Rep. *8*, 14836. https://doi.org/10.1038/s41598-018-32025-w.

51. Butler, J.A., Ventura, N., Johnson, T.E., and Rea, S.L. (2010). Long-lived mitochondrial (Mit) mutants of Caenorhabditis elegans utilize a novel metabolism. FASEB J. *24*, 4977–4988. https://doi.org/10.1096/fj.10-162941.

52. Senoo-Matsuda, N., Hartman, P.S., Akatsuka, A., Yoshimura, S., and Ishii, N. (2003). A complex II defect affects mitochondrial structure, leading to ced-3- and ced-4-dependent apoptosis and aging. J. Biol. Chem. *278*, 22031–22036. https://doi.org/10.1074/jbc.M211377200.

53. Fitzenberger, E., Boll, M., and Wenzel, U. (2013). Impairment of the proteasome is crucial for glucose-induced lifespan reduction in the mev-1 mutant of Caenorhabditis elegans. Biochim. Biophys. Acta *1832*, 565–573. https://doi.org/10.1016/j.bbadis.2013.01.012.

54. Baruah, A., Chang, H., Hall, M., Yuan, J., Gordon, S., Johnson, E., Shtessel, L.L., Yee, C., Hekimi, S., Derry, W.B., et al. (2014). CEP-1, the Caenorhabditis elegans p53 homolog, mediates opposing longevity outcomes in mitochondrial electron transport chain mutants. PLoS Genet. *10*, e1004097. https://doi.org/10.1371/journal.pgen.1004097.

55. Rea, S.L., Ventura, N., and Johnson, T.E. (2007). Relationship between mitochondrial electron transport chain dysfunction, development, and life extension in Caenorhabditis elegans. PLoS Biol. *5*, e259. https://doi.org/10.1371/journal.pbio.0050259.

56. Mikdar, M., González-Menéndez, P., Cai, X., Zhang, Y., Serra, M., Dembélé, A.K., Boschat, A.C., Sanquer, S., Chhuon, C., Guerrera, I.C., et al. (2021). The equilibrative nucleoside transporter 1 (ENT1) is critical for nucleotide homeostasis and optimal erythropoiesis. Blood *137*, 3548–3562. https://doi.org/10.1182/blood.2020007281.

57. Warraich, S., Bone, D.B.J., Quinonez, D., Ii, H., Choi, D.S., Holdsworth, D.W., Drangova, M., Dixon, S.J., Séguin, C.A., and Hammond, J.R. (2013). Loss of equilibrative nucleoside transporter 1 in mice leads to progressive ectopic mineralization of spinal tissues resembling diffuse idiopathic skeletal hyperostosis in humans. J. Bone Miner. Res. *28*, 1135–1149. https://doi.org/10.1002/jbmr.1826.

58. Culetto, E., and Sattelle, D.B. (2000). A role for Caenorhabditis elegans in understanding the function and interactions of human disease genes. Hum. Mol. Genet. *9*, 869–877. https://doi.org/10.1093/hmg/9.6.869.

59. Wang, C., Weerapana, E., Blewett, M.M., and Cravatt, B.F. (2014). A chemoproteomic platform to quantitatively map targets of lipid-derived electrophiles. Nat. Methods *11*, 79–85. https://doi.org/10.1038/nmeth.2759.

60. Martell, J., Seo, Y., Bak, D.W., Kingsley, S.F., Tissenbaum, H.A., and Weerapana, E. (2016). Global cysteine-reactivity profiling during impaired insulin/IGF-1 signaling in C. elegans identifies uncharacterized mediators of longevity. Cell Chem. Biol. *23*, 955–966. https://doi.org/10.1016/j.chembiol.2016.06.015.

61. Edgar, R.C. (2022). Muscle5: high-accuracy alignment ensembles enable unbiased assessments of sequence homology and phylogeny. Nat. Commun. *13*, 6968. https://doi.org/10.1038/s41467-022-34630-w.

62. Surya, S.L., Long, M.J.C., Urul, D.A., Zhao, Y., Mercer, E.J., Elsaid, I.M., Evans, T., and Aye, Y. (2018). Cardiovascular small heat shock protein HSPB7 is a kinetically privileged reactive electrophilic species (RES) sensor. ACS Chem. Biol. *13*, 1824–1831. https://doi.org/10.1021/acschembio.7b00925.

63. Zhao, Y., Long, M.J.C., Wang, Y., Zhang, S., and Aye, Y. (2018). Ube2V2 is a Rosetta Stone bridging redox and ubiquitin codes, coordinating DNA damage responses. ACS Cent. Sci. *4*, 246–259. https://doi.org/10.1021/acscentsci.7b00556.

64. Vaz, A.D., McGinnity, D.F., and Coon, M.J. (1998). Epoxidation of olefins by cytochrome P450: evidence from site-specific mutagenesis for hydroperoxo-iron as an electrophilic oxidant. Proc. Natl. Acad. Sci. USA *95*, 3555–3560. https://doi.org/10.1073/pnas.95.7.3555.

65. Amunom, I., Dieter, L.J., Tamasi, V., Cai, J., Conklin, D.J., Srivastava, S., Martin, M.V., Guengerich, F.P., and Prough, R.A. (2011). Cytochromes P450 catalyze the reduction of α,β-unsaturated aldehydes. Chem. Res. Toxicol. *24*, 1223–1230. https://doi.org/10.1021/tx200080b.

66. Guéraud, F., Alary, J., Costet, P., Debrauwer, L., Dolo, L., Pineau, T., and Paris, A. (1999). In vivo involvement of cytochrome P450 4A family in the oxidative metabolism of the lipid peroxidation product trans-4-hydroxy-2-nonenal, using PPARalpha-deficient mice. J. Lipid Res. *40*, 152–159.

67. Kuo, C.L., Vaz, A.D., and Coon, M.J. (1997). Metabolic activation of trans-4-hydroxy-2-nonenal, a toxic product of membrane lipid peroxidation and inhibitor of P450 cytochromes. J. Biol. Chem. *272*, 22611–22616. https://doi.org/10.1074/jbc.272.36.22611.

68. Raza, H., and John, A. (2006). 4-hydroxynonenal induces mitochondrial oxidative stress, apoptosis and expression of glutathione S-transferase A4-4 and cytochrome P450 2E1 in PC12 cells. Toxicol. Appl. Pharmacol. *216*, 309–318. https://doi.org/10.1016/j.taap.2006.06.001.

69. Teramoto, T., Lambie, E.J., and Iwasaki, K. (2005). Differential regulation of TRPM channels governs electrolyte homeostasis in the C. elegans intestine. Cell Metab. *1*, 343–354. https://doi.org/10.1016/j.cmet.2005.04.007.

70. Branicky, R., Shibata, Y., Feng, J., and Hekimi, S. (2001). Phenotypic and suppressor analysis of defecation in clk-1 mutants reveals that reaction to changes in temperature is an active process in Caenorhabditis elegans. Genetics *159*, 997–1006. https://doi.org/10.1093/genetics/159.3.997.

71. Watterson, A., Tatge, L., Wajahat, N., Arneaud, S.L.B., Solano Fonseca, R., Beheshti, S.T., Metang, P., Mihelakis, M., Zuurbier, K.R., Corley, C.D., et al. (2022). Intracellular lipid surveillance by small G protein geranylgeranylation. Nature *605*, 736–740. https://doi.org/10.1038/s41586-022-04729-7.

72. Watts, J.S., Harrison, H.F., Omi, S., Guenthers, Q., Dalelio, J., Pujol, N., and Watts, J.L. (2020). New strains for tissue-specific RNAi studies in Caenorhabditis elegans. G3 (Bethesda) *10*, 4167–4176. https://doi.org/10.1534/g3.120.401749.

73. Lee, A.L., Ung, H.M., Sands, L.P., and Kikis, E.A. (2017). A new Caenorhabditis elegans model of human huntingtin 513 aggregation and toxicity in body wall muscles. PLoS One *12*, e0173644. https://doi.org/10.1371/journal.pone.0173644.

74. Antoni, M.H., Lutgendorf, S.K., Cole, S.W., Dhabhar, F.S., Sephton, S.E., McDonald, P.G., Stefanek, M., and Sood, A.K. (2006). The influence of bio-behavioural factors on tumour biology: pathways and mechanisms. Nat. Rev. Cancer *6*, 240–248. https://doi.org/10.1038/nrc1820.

75. Isoherranen, N., and Zhong, G. (2019). Biochemical and physiological importance of the CYP26 retinoic acid hydroxylases. Pharmacol. Ther. *204*, 107400. https://doi.org/10.1016/j.pharmthera.2019.107400.

76. He, Y., Gong, L., Fang, Y., Zhan, Q., Liu, H.X., Lu, Y., Guo, G.L., Lehman-McKeeman, L., Fang, J., and Wan, Y.J.Y. (2013). The role of retinoic acid in hepatic lipid homeostasis defined by genomic binding and transcriptome profiling. BMC Genomics *14*, 575. https://doi.org/10.1186/1471-2164-14-575.

77. Larigot, L., Mansuy, D., Borowski, I., Coumoul, X., and Dairou, J. (2022). Cytochromes P450 of Caenorhabditis elegans: implication in biological functions and metabolism of xenobiotics. Biomolecules *12*, 342. https://doi.org/10.3390/biom12030342.

78. Long, M.J., Lin, H.-Y., Parvez, S., Zhao, Y., Poganik, J.R., Huang, P., and Aye, Y. (2017). β-TrCP1 Is a Vacillatory Regulator of Wnt Signaling. Cell Chem. Biol. *24*, 944–957.e7. https://doi.org/10.1016/j.chembiol.2017.06.009.

79. Schindelin, J., Arganda-Carreras, I., Frise, E., Kaynig, V., Longair, M., Pietzsch, T., Preibisch, S., Rueden, C., Saalfeld, S., Schmid, B., et al. (2012). Fiji: an open-source platform for biological-image analysis. Nat. Methods *9*, 676–682. https://doi.org/10.1038/nmeth.2019.

80. Kolberg, L., Raudvere, U., Kuzmin, I., Adler, P., Vilo, J., and Peterson, H. (2023). g:profiler-interoperable web service for functional enrichment analysis and gene identifier mapping (2023 update). Nucleic Acids Res. *51*, W207–W212. https://doi.org/10.1093/nar/gkad347.

81. Cox, J., and Mann, M. (2008). MaxQuant enables high peptide identification rates, individualized p.p.b.-range mass accuracies and proteome-wide protein quantification. Nat. Biotechnol. *26*, 1367–1372. https://doi.org/10.1038/nbt.1511.

82. Tamura, K., Stecher, G., and Kumar, S. (2021). MEGA11: Molecular Evolutionary Genetics Analysis, version 11. Mol. Biol. Evol. *38*, 3022–3027. https://doi.org/10.1093/molbev/msab120.

83. Szklarczyk, D., Kirsch, R., Koutrouli, M., Nastou, K., Mehryary, F., Hachilif, R., Gable, A.L., Fang, T., Doncheva, N.T., Pyysalo, S., et al. (2023). The STRING database in 2023: protein-protein association networks and functional enrichment analyses for any sequenced genome of interest. Nucleic Acids Res. *51*, D638–D646. https://doi.org/10.1093/nar/gkac1000.

84. Goddard, T.D., Huang, C.C., Meng, E.C., Pettersen, E.F., Couch, G.S., Morris, J.H., and Ferrin, T.E. (2018). UCSF ChimeraX: meeting modern challenges in visualization and analysis. Protein Sci. *27*, 14–25. https://doi.org/10.1002/pro.3235.

85. Long, M.J.C., Urul, D.A., Chawla, S., Lin, H.-Y., Zhao, Y., Haegele, J.A., Wang, Y., and Aye, Y. (2018). Precision electrophile tagging in Caenorhabditis elegans. Biochemistry *57*, 216–220. https://doi.org/10.1021/acs.biochem.7b00642.

86. Rappsilber, J., Mann, M., and Ishihama, Y. (2007). Protocol for micro-purification, enrichment, pre-fractionation and storage of peptides for proteomics using StageTips. Nat. Protoc. *2*, 1896–1906. https://doi.org/10.1038/nprot.2007.261.

87. Jones, D.T., Taylor, W.R., and Thornton, J.M. (1992). The rapid generation of mutation data matrices from protein sequences. Comput. Appl. Biosci. *8*, 275–282. https://doi.org/10.1093/bioinformatics/8.3.275.

STAR★METHODS

KEY RESOURCES TABLE

REAGENT or RESOURCE	SOURCE	IDENTIFIER
Antibodies		
Anti-β-actin-HRP conjugated primary antibody	Sigma	Cat#A3854; RRID:AB_262011
Anti-HaloTag monoclonal antibody	Promega	Cat#G9211; RRID:AB_2688011
GFP antibody (B-2)	Santa Cruz Biotech	Cat#sc-9996; RRID:AB_627695
DYKDDDDK polyclonal antibody	Thermo Fischer	Cat#PA1-984B; RRID:AB_347227
Anti-4-hydroxynonenal antibody	Abcam	Cat#ab46544; RRID:AB_722493
Rabbit anti-DNP antibody (in Oxyblot kit)	in S7150; Sigma	Cat#90451
Anti-GFP antibody	Abcam	Cat#ab6673; RRID:AB_305643
Donkey anti-goat IgG H&L (Alexa Fluor® 488)	Abcam	Cat#ab150133; RRID:AB_2832252
Mouse anti-goat IgG-HRP	Santa Cruz Biotech	Cat#sc-2354; RRID:AB_628490
Streptavidin-HRP	Abcam	Cat#ab7403
Anti-rabbit IgG, HRP-linked Antibody	Cell Signaling Technology	Cat#7074S; RRID:AB_2099233
Anti-mouse IgG, HRP-linked Antibody	Cell Signaling Technology	Cat#7076S; RRID:AB_330924
Goat anti-Rabbit IgG (HRP-conjugated)	in S7150; Sigma	Cat#90452
Chemicals, Peptides, and Recombinant Proteins		
cOmplete™ mini (EDTA free) protease inhibitor	Roche	Cat#11836170001
NADPH, tetrasodium salt	Roche	Cat#10041939103; CAS: 2646-71-1
Biotin-dPEG™$_{11}$-Azide	Iris Biotech	Cat#PEG4340; CAS: 956494-20-5
Acrylamide/Bisacrylamide 37.5:1, 30% solution	Abcr	Cat#ab350851; CAS: 1173018-90-0
HCl	Reactolab	Cat#99400; CAS: 7647-01-0
KOH	Reactolab	Cat#99510; CAS: 1310-58-3
Methanol	Thommen Furler	Cat#203-VL54K; CAS: 67-56-1
Acetone	Thommen Furler	Cat#133-VL54K; CAS: 67-64-1
TCEP·HCl	Goldbio	Cat#TCEP25; CAS: 51805-45-9
Isopropyl β-D-1-thio-galactopyranoside (IPTG)	Goldbio	Cat#I2481C25; CAS: 16758-34-2
Cu(II)-TBTA, 10 mM in 55% DMSO	Lumiprobe	Cat#21050
Sulfo-cyanine5 (Cy5)-azide	Lumiprobe	Cat#B3330
TMR-Halo ligand	Promega	Cat#G8251
Set of dATP, dCTP, dGTP, dTTP	Promega	Cat#U1240
NcoI-HF	NEB	Cat#R3193
DpnI	NEB	Cat#R0176L
SexAI	NEB	Cat#0605S
XmaI	NEB	Cat#R0180S
Phusion HotStart II polymerase	ThermoFisher (Invitrogen)	Cat#F549L
Phusion HF Buffer Pack	ThermoFisher (Invitrogen)	Cat#F518L
Pierce™ Bovine Serum Albumin Standard Ampules	ThermoFisher (Invitrogen)	Cat#23209
TRIzol™ reagent	ThermoFisher (Invitrogen)	Cat#15596018
High-capacity streptavidin agarose	ThermoFisher (Invitrogen)	Cat#20361
TMTsixplex™ Isobaric Label Reagent Set	ThermoFisher (Invitrogen)	Cat#90068
TMT10plex™ Isobaric Label Reagent Set	ThermoFisher (Invitrogen)	Cat#90111
TMT11-131C Label Reagent	ThermoFisher (Invitrogen)	Cat#A37724
Pierce™ ECL Plus Western Blotting Substrate	ThermoFisher (Invitrogen)	Cat#32132
Pierce™ ECL Western Blotting Substrate	ThermoFisher (Invitrogen)	Cat#32106
Novex™ Tris-Glycine Mini Protein Gels	ThermoFisher (Invitrogen)	Cat#XP00120BOX

(*Continued on next page*)

Continued

REAGENT or RESOURCE	SOURCE	IDENTIFIER
Pierce™ Trypsin Protease	ThermoFisher (Invitrogen)	Cat#90058
RNaseOUT™ Recombinant Ribonuclease Inhibitor	ThermoFisher (Invitrogen)	Cat#10777019
Superscript™ III Reverse Transcriptase	ThermoFisher (Invitrogen)	Cat#18080093
Quick Start™ Bradford 1x dye reagent	Bio-Rad	Cat#5000205
iQ™ SYBR® Green Supermix Dye	Bio-Rad	Cat#1708880
Precision Plus Protein™ unstained standard	Bio-Rad	Cat#1610363
Precision Plus Protein™ all blue standard	Bio-Rad	Cat#1610373
Immun-Blot PVDF Membrane	Bio-Rad	Cat#1620177
Coomassie blue G250	Fisher Scientific	Cat#C/P541/46; CAS: 6104-58-1
Ethanol	Fisher Scientific	Cat#E/0650DF/17; CAS: 64-17-5
Fetal Bovine Serum	sigma-aldrich	Cat#F0392
K_2HPO_4	sigma-aldrich	Cat#P3786; CAS: 7758-11-4
KH_2PO_4	sigma-aldrich	Cat#P0662; CAS: 7778-77-0
$CuSO_4$	sigma-aldrich	Cat#209198; CAS: 7758-99-8
t-BuOH	sigma-aldrich	Cat#471712; CAS: 75-65-0
Tween-20	sigma-aldrich	Cat#P9416; CAS: 9005-64-5
Triton X-100	sigma-aldrich	Cat#X100; CAS: 9036-19-5
Ammonium persulfate (APS)	sigma-aldrich	Cat#A3678; CAS: 7727-54-0
Glycine	sigma-aldrich	Cat#G8898; CAS: 56-40-6
N,N,N',N'-Tetramethylethylenediamine (TEMED)	sigma-aldrich	Cat#T7024; CAS: 110-18-9
Biotin	sigma-aldrich	Cat#B4639; CAS: 58-85-5
Lysozyme	sigma-aldrich	Cat#10837059001
DNase I	sigma-aldrich	Cat# 11284932001
Oil Red O solution	sigma-aldrich	Cat#O1391; CAS: 1320-06-5
Dimethyl sulfoxide (DMSO)	sigma-aldrich	Cat#D8418; CAS: 67-68-5
Paraformaldehyde (PFA)	sigma-aldrich	Cat#P6148; CAS: 30525-89-4
2-mercaptoethanol (BME)	sigma-aldrich	Cat#M3148; CAS: 60-24-2
Immobilon ECL Ultra Western HRP Substrate	sigma-aldrich	Cat#WBULS0500
Proteinase K	sigma-aldrich	Cat#P2308
Lithium dodecyl sulfate (LDS)	sigma-aldrich	Cat#L9781; CAS: 2044-56-6
Na_2HPO_4	sigma-aldrich	Cat#S9390; CAS: 7782-85-6
Na_2EDTA	Apollo Scientific	Cat#BIA1417; CAS: 6381-92-6
Tris(hydroxymethyl)aminomethane (Tris)	Apollo Scientific	Cat#BI2888; CAS: 77-86-1
Agarose	Apollo Scientific	Cat#BIA1176; CAS: 9012-36-6
Tryptone	Apollo Scientific	Cat#BIT1332
4-(2-hydroxyethyl)-1-piperazineethanesulfonic acid (HEPES)	Apollo Scientific	Cat#BI8181; CAS: 7365-45-9
Sodium dodecyl sulfate (SDS)	Apollo Scientific	Cat#BIB2008; CAS: 151-21-3
$MgSO_4$	ThermoFisher (Acros)	Cat#10003812; CAS: 7487-88-9
Glycerol	ThermoFisher (Acros)	Cat#158920100; CAS: 56-81-5
NaCl	AppliChem	Cat#A2942; CAS: 7647-14-5
RbCl	AppliChem	Cat#A4240; CAS: 7791-11-9
$CaCl_2$	AppliChem	Cat#A4689; CAS: 10035-04-8
Imidazole	AppliChem	Cat#A1073; CAS: 288-32-4
Ammonium sulfate	AppliChem	Cat#A3485; CAS: 7783-20-2
Sodium azide	AppliChem	Cat#A1430; CAS: 26628-22-8
PMSF	AppliChem	Cat#A0999; CAS: 329-98-6

(*Continued on next page*)

Continued

REAGENT or RESOURCE	SOURCE	IDENTIFIER
Ampicillin	AppliChem	Cat#A0839; CAS: 69-52-3
Carbenicillin	AppliChem	Cat#A1491; CAS: 4800-94-6
Kanamycin	AppliChem	Cat#A1493; CAS: 5965-95-7
Yeast extract	AppliChem	Cat#A3732
Ortho-phosphoric acid	AppliChem	Cat#131032; CAS: 7664-38-2
MOPS	AppliChem	Cat#A2947; CAS: 1132-61-2
Pluronic F-68	AppliChem	Cat#A1288; CAS: 9003-11-6
Glutathione (GSH)	TCI	Cat#G0074; CAS: 70-18-8
DMEM	GIBCO	Cat#41965039
Opti-MEM	GIBCO	Cat#51985026
RPMI 1640	GIBCO	Cat#21875034
MEM Non-Essential Amino Acids Solution (100X)	GIBCO	Cat#11140035
Penicillin-Streptomycin	GIBCO	Cat#15140122
DPBS, no calcium, no magnesium	GIBCO	Cat#14190094
Sodium Pyruvate	GIBCO	Cat#11360039
TrypLE Express Enzyme	GIBCO	Cat#12605028
Cytochrome P450 2A6 Human Recombinant Protein	OriGene Technologies	Cat#TP322995
PEI MAX - Transfection Grade	Polysciences	Cat#24765-1
HyCell TransFx-H transfection media	Cytiva	Cat#SH30939
4-hydroxynonenal in EtOH (HNE)	Cayman	Cat#32100; CAS: 75899-68-2
HaloTag-targetable photocaged precursor to HNE [Ht-PreHNE(alkyne)]	Long et al.[78]	N/A
HaloTag-targetable photocaged precursor to HNE [Ht-PreHNE(no alkyne)]	Long et al.[78]	N/A
HNE(alkyne-functionalized) [HNE(alkyne)]	Long et al.[78]	CAS: 1011268-23-7
HNA(alkyne-functionalized) [HNA(alkyne)]	This paper	N/A
DHN(alkyne-functionalized) [DHN(alkyne)]	This paper	N/A
Critical Commercial Assays		
OxyBlot Protein Oxidation Detection Kit	sigma-aldrich	Cat#S7150
Vivid CYP2A6 Blue Screening Kit	ThermoFisher	Cat#PV6140
Pure Yield Plasmid Miniprep System	Promega	Cat#A1222
Wizard SV Gel and PCR Clean-Up System	Promega	Cat#A9285
Experimental Models: Cell Lines		
Human cell line: HEK293T	ATCC	Cat#CRL-3216; RRID:CVCL_0063
Human cell line: HEK293	EPFL PTPSP	N/A
Bacterial and Virus Strains		
E. coli OP50	Caenorhabditis Genetics Center (CGC)	WormBase: OP50; WormBase: WBStrain00041969
E. coli Ht115(DE3)	Caenorhabditis Genetics Center (CGC)	WormBase: HT115; WormBase: WBStrain00041079
E. coli XL10	Agilent	Cat#200315
Deposited Data		
TMT organ-specific electrophile-responder analysis in OS-Localis-REX strains	This paper	PRIDE: PXD027730
TMT organ-specific abundance analysis in OS-Ultra-ID strains	This paper	PRIDE: PXD052114

(*Continued on next page*)

Continued

REAGENT or RESOURCE	SOURCE	IDENTIFIER
LFQ whole-proteome analysis in OS-Ultra-ID strains	This paper	PRIDE: PXD052493
Mendeley Data	This paper	http://www.doi.org/10.17632/4gyvt94vnm.1
Experimental Models: Organisms/Strains		
C. elegans N2	Caenorhabditis Genetics Center (CGC)	WormBase: N2; WormBase: WBStrain00000001
C. elegans LIU1, *dhs-3p::dhs-3::gfp*	Caenorhabditis Genetics Center (CGC)	WormBase: LIU1; WormBase: WBStrain00024198
C. elegans IG1839, *frSi17 [mtl-2p::rde-1::rde-1 3'UTR]* ***II****; frIs7 [nlp-29p::gfp + col-12p::DsRed]* ***IV****; rde-1(ne300)* ***V***	Caenorhabditis Genetics Center (CGC)	WormBase: IG1839; WormBase: WBStrain00050715
C. elegans WM118, *neIs9 [myo-3::HA::rde-1:: rde-1 3'UTR + rol-6(su1006)]* ***X****; rde-1(ne300)* ***V***	Caenorhabditis Genetics Center (CGC)	WormBase: WM118; WormBase: WBStrain00040438
C. elegans EAK102, *eeeIs1 [unc-54p:: Htt513(Q15)::yfp::unc-54 3'UTR]*	Caenorhabditis Genetics Center (CGC)	WormBase: EAK102; WormBase: WBStrain00006456
C. elegans EAK103, *eeeIs2 [unc-54p:: Htt513(Q128)::yfp::unc-54 3'UTR]*	Caenorhabditis Genetics Center (CGC)	WormBase: EAK103; WormBase: WBStrain00006457
myo-2p::gfp::halo::unc-54 3'UTR + mec-7p::mRFP	This paper	CYA03
ges-1p::gfp::halo::unc-54 3'UTR + mec-7p::mRFP	This paper	CYA04
myo-3p::gfp::halo::unc-54 3'UTR + mec-7p::mRFP	This paper	CYA05
myo-2p::mCherry::P2A:: UltraID::unc-54 3'UTR	This paper	CYA06
ges-1p::mCherry::P2A:: UltraID::unc-54 3'UTR	This paper	CYA07
myo-3p::mCherry::P2A:: UltraID::unc-54 3'UTR	This paper	CYA08
cyp-33e1 C295A	This paper, Methods S1	PHX8800
cyp-33e1 C439A	This paper, Methods S1	PHX8844
dhs-3p::dhs-3::gfp; cyp-33e1 C295A	This paper	CYA09
dhs-3p::dhs-3::gfp; cyp-33e1 C439A	This paper	CYA10
dhs-3p::dhs-3::gfp; unc-54p:: htt513(Q15)::yfp	This paper	CYA11
dhs-3p::dhs-3::gfp; unc-54p:: htt513(Q128)::yfp	This paper	CYA12
dhs-3p::dhs-3::gfp; frSi17 [mtl-2p:: rde-1::rde-1 3'UTR] ***II****; rde-1(ne300)* ***V***	This paper	CYA13
dhs-3p::dhs-3::gfp; neIs9 [myo-3p:: HA::rde-1 + rol-6(su1006)] ***X****; rde-1(ne300)* ***V***	This paper	CYA14
Oligonucleotides		
Primers for sequencing, cloning and qPCR	This paper, Methods S1	N/A
Recombinant DNA		
pCS2+8-cyp-33e1-flag-tev-halo-his	This paper	N/A
pCS2+8-aex-5-flag-tev-halo-his	This paper	N/A
pCS2+8-asp-2-flag-tev-halo-his	This paper	N/A
pCS2+8-CYP2A6-flag-tev-halo-his	This paper	N/A
pCS2+8-PCSK1-flag-tev-halo-his	This paper	N/A
pCS2+8- cyp-33e1(C295A)-flag-tev-halo-his	This paper	N/A
pCS2+8- cyp-33e1(C439A)-flag-tev-halo-his	This paper	N/A

(*Continued on next page*)

Continued

REAGENT or RESOURCE	SOURCE	IDENTIFIER
pCS2+8- cyp-33e1(C295A, C439A)-flag-tev-halo-his	This paper	N/A
pCS2+8-CYP2A6(C14A)-flag-tev-halo-his	This paper	N/A
pCS2+8-CYP2A6(C82A)-flag-tev-halo-his	This paper	N/A
pCS2+8-CYP2A6(C439A)-flag-tev-halo-his	This paper	N/A
pCS2+8-CYP2A6(C14A, C82A)-flag-tev-halo-his	This paper	N/A
pCS2+8-CYP2A6(C82A, C439A)-flag-tev-halo-his	This paper	N/A
pCS2+8-CYP2A6(C14A, C82A, C439A)-flag-tev-halo-his	This paper	N/A
pCS2+8-CYP2A6-flag-tev-his	This paper	N/A
pCS2+8-CYP2A6(C82A)-flag-tev-his	This paper	N/A
pCS2+8-CYP2A6(C439A)-flag-tev-his	This paper	N/A
pCS2+8-CYP2A6(C82A, C439A)-flag-tev-his	This paper	N/A
pWormgate2-myo-2p-gfp-halo	This paper, Methods S1	N/A
pWormgate2-ges-1p-gfp-halo	This paper, Methods S1	N/A
pWormgate2-myo-3p-gfp-halo	This paper, Methods S1	N/A
pWormgate2-myo-2p-mCherry-P2A-flag-UltraID	This paper, Methods S1	N/A
pWormgate2-ges-1p-mCherry-P2A-flag-UltraID	This paper, Methods S1	N/A
pWormgate2-myo-3p-mCherry-P2A-flag-UltraID	This paper, Methods S1	N/A
Software and Algorithms		
Fiji ImageJ 1.53f51	Schindelin et al.[79]	https://imagej.net/Fiji
g:*Profiler*	Kolberg et al.[80]	https://bio.tools/gprofiler
MaxQuant 1.6.8.0; 2.4.4.0	Cox and Mann[81]	https://www.maxquant.org/
MEGA 11	Tamura et al.[82]	https://www.megasoftware.net/
MUSCLE5	Edgar[61]	https://www.drive5.com/muscle/
Cytoscape 3.10.1	Szklarczyk et al.[83]	https://jensenlab.org/training/stringapp/
Prism 8-10	GraphPad Software	https://www.graphpad.com/
LAS X 3.8.2	Leica Microsystems	https://www.leica-microsystems.com/products/microscope-software/p/leica-las-x-ls/
Chimera X 1.1	Goddard et al.[84]	https://www.rbvi.ucsf.edu/chimerax
UNIFI 1.9.4.053	Waters Corporation	https://www.waters.com/
Other		
Leica fluorescence stereomicroscope	Leica	M205 FA
Microscope Camera	Leica	DFC7000 T

EXPERIMENTAL MODEL AND STUDY PARTICIPANT DETAILS

Technical services and contracted research organizations (CROs)

TMT-multiplex data processing and analysis were performed by Dr. Florence Armand (EPFL SV proteomics core facility) in collaboration with R.H., J.L., and Y.A. *C. elegans* transgenic and knock-in lines were designed by J.L., D.A.U., M.J.C.L., and Y.A., and subsequently generated in collaboration with the SUNY Biotech CRO. Small-molecule MS analysis data acquisition, processing and analysis were performed by Dr. Daniel Ortiz Trujillo (EPFL ISIC mass-spectrometry core facility) in collaboration with Y.-Q.G. and J.L.

Construction of plasmids

Sequences of all primers used for cloning and mutagenesis are listed in Methods S1. For protein overexpression in cultured HEK293T cells, all constructs were generated in pCS2+8 vector, using ligase-free Hawaiian cloning.[24] Cyp-33e1, aex-5, and asp-2 sequences were amplified from *C. elegans* cDNA, and cloned into pCS2+8 vector using the appropriate forward and reverse primers with Phusion Hotstart II following the manufacturer's protocol. Prior to insertion, the empty pCS2+8 plasmid was digested with appropriate restriction enzymes (NEB). The products were digested by DpnI (NEB) for 1 hour before transformation into XL10 Gold Ultracompetent cells (Agilent). The inserts generated were fully validated by Sanger sequencing using Microsynth sequencing service, Lausanne, Switzerland.

For cyp-33e1 and CYP2A6 mutagenesis in pCS2+8 vector, the appropriate forward and reverse primers listed in Methods S1 containing desired mutations were designed by Agilent QuikChange tool. Under different annealing temperatures (from 56 °C to 68 °C), pCS2+8 backbone and the primers were incubated in the thermocycler with Phusion Hotstart II, following the manufacturer's protocol. The products were digested by DpnI (NEB) for 2 hours before transformation into XL10 Gold Ultracompetent cells. The mutation sites were fully validated by Sanger sequencing using Microsynth sequencing service, Lausanne, Switzerland.

C. elegans maintenance and culture

Previously-reported procedures were followed.[85] Briefly, All *C. elegans* strains were grown at 17 °C for maintenance unless otherwise indicated. All worms were derived from the Bristol N2 *C. elegans* strain. Nematode growth medium (NGM-agarose) contained: 0.79 g Tris base (6.5 mM), 2 g NaCl (34 mM), 3 g tryptone, 17 g agarose, pH = 8.0, per liter of ddH_2O. Post autoclaving, when the temperature had become 50 - 60 °C, 1 mL (5 mg/L) cholesterol in EtOH was added per liter of media to render the final concentration as 5 μg/L. For a 10-cm plate, 15 mL NGM-agarose media was pipetted using sterile procedures. In parallel, to prepare OP50, bacteria were inoculated into 3 mL LB media (containing the following components in final concentrations: 10 g/L NaCl, 10 g/L tryptone, 5 g/L yeast extract). The cultures were incubated overnight at 37 °C with shaking, and 1 mL was to 200 mL flasks with ∼60 mL LB media. Then the flasks were incubated overnight at 37 °C with shaking. 1.5 mL OP50 was dispensed into the middle of solidified 10 cm NGM-agarose plates (described above) at room temperature in sterile biosafety cabinets. When OP50 was dry, the plates were subsequently stored at 4 °C. 20 healthy L4-young adult *C. elegans* were selected using platinum picks and grown on 10 cm NGM-agarose plates for 4-5 days at 20 °C until harvesting, which was performed when the plate had become densely populated but prior to starvation. Unless otherwise indicated, worm ages were not synchronized.

C. elegans Strains Generation

(i) Transgenic strains for OS-Localis-REX. (See Methods S1 for gene sequence and primers used to sequence the injected plasmids. Plasmids and worm strains will be deposited to Addgene and CGC repositories, respectively, post manuscript publication).

(ii) Transgenic strains for OS-Ultra-ID. (See Methods S1 for gene sequence and primers used to sequence the injected plasmids. Plasmids and worm strains will be deposited to Addgene and CGC repositories, respectively, post manuscript publication).

For transgenic strain generation, 10 μL corresponding plasmids were injected into the gonads of 30 adult wild-type P_0 worms. For OS-Localis-REX strains, the plasmids concentration was 100 ng/μL, mixed with 100 ng/μL plasmids (of the same backbone) with mec-7p::mRFP transgene marker. For OS-Ultra-ID strains, the plasmids' concentrations were: 10 ng/μL for myo-3p strains, 20 ng/μL for ges-1p strain, and 5 ng/μL mixed with empty vector pSL1190 plasmid (95 ng/uL) for myo-2p strain. The F_1 progeny carrying transgenic arrays were further selected and isolated in individual NGM plates for culturing. After the stable transgenic lines were isolated, the single worm PCR was applied to the extrachromosomal lines containing target plasmid for verification.

(iii) Knock-in strains using CRISPR-cas9. (See Methods S1 for gene sequence and primers used in single-worm PCR for mutation-site validations. Plasmids and worm strains will be deposited to Addgene and CGC repositories, respectively, post manuscript publication).

The sgRNAs were designed for both knock-in strains: Sg1: CCGTAAGCAGGCTACAGATAGAC; Sg2: CCGACCGAC CTAAACTCAACTAT for PHX8800 (cyp-33e1 syb8800, C295A); Sg1: CCAAAATGGAACTATTCTTGTAT; Sg2: CCTGAACCATA CGAATTCAAACC for PHX8844 (cyp-33e1 syb8844, C439A). A ∼1200 kb sequence near the mutation site was designed as the repair template. The sgRNA plasmids, repair template, Cas9 plasmid and co-injection marker were mixed and injected into the gonads of 30 adult P_0 worms. The F1 progeny with the precise expected sequence were further selected and isolated in individual NGM plates for culturing, verified by single worm PCR and restriction enzyme cutting. The stable homozygous progeny was isolated and validated by single worm PCR and sequencing.

Cell Culture

HEK293T (obtained from ATCC) and were cultured in MEM (Gibco) supplemented with 10% v/v fetal bovine serum (Sigma), penicillin/streptomycin (Gibco), sodium pyruvate (Gibco), and nonessential amino acids (Gibco) at 37 °C in a humidified atmosphere of 5% CO_2. Media were changed every 2–3 days. Mycoplasma test was performed tri-monthly using Venor GeM PCR-based mycoplasma detection kit. The kit was used as stated in the manual and purchased from Sigma.

METHOD DETAILS

Validation of antibodies

To validate primary antibodies used for the western blot analyses of the lysates originating from *C. elegans*, Bristol N2 (wild-type) strain, which does not express Halo/GFP, was used. Identical procedures of sample handling and data processing were performed for N2 worms as for transgenic worms. Antibodies used for the western blot analyses of the lysates originating from HEK293T cells

(key resources table) have been previously validated in the literature. Antibodies in the Oxyblot kit were validated by eliminating the carbonyl group derivatization using 2,4-Dinitrophenylhydrazine (DNPH) solution provided by the manufacturer.

Western blotting

Cells lysates, worm lysates, or appropriate samples as described in 1x Laemmli dye, were loaded on 11% or 15% SDS gel, separated by SDS-PAGE, transferred to PVDF either at 30 V overnight or 80V for 1 hour, followed by 55 V for 2 hours. The membrane was blocked in either 5% skimmed milk or 1% BSA recommended by the manufacturer for 2 hours, and then incubated with the appropriate antibodies (key resource table). Detection was carried out on the Fusion FX imager (Vilber) using ECL Western Blotting Substrate (Pierce) or Immobilon ECL Ultra Western HRP Substrate (Sigma). Western blot data were quantitated using the Gel Analysis tool in Fiji ImageJ 1.53f51.

Worm lysis

Worm pellets were removed from -80 °C and thawed on ice. 1x Roche cOmplete™ mini (EDTA free) protease inhibitor (in the final concentration recommended by manufacturer) was dissolved in 4.48 mL 50 mM HEPES (pH = 7.6), to which 50 μL 100 mM TCEP in 50 mM HEPES (pH = 7.0) and 0.5 mL 10% Triton-X100 in 50 mM HEPES (pH = 7.6) were added to generate the lysis buffer, which was freshly prepared just before use and kept chilled on ice. Per each worm pellet, 2-8 x pellet volumes of lysis buffer (400 μL) and 1/4 volume of zirconia beads were applied. (In pulldown experiments, volumes of pellets used where: typically, 60-100 μL). Once the worm pellets were thawed, the lysate buffer and the beads were added and the samples were vortexed for 15 seconds then freeze-thawed using liquid nitrogen (repeated 3 times). Afterwards, the samples were centrifuged at 20,000 x g, at 4 °C for 10 minutes. The supernatant was collected, and the protein concentration (in independent triplicate) was measured by Bradford assay. In each replicate of the Bradford assay, 1 μL lysate was mixed with 1 mL Bradford reagent. Then 200 μL of the mixture was pipetted to 96-well plates. Absorbance at 595 nm was measured using a plate reader and protein concentration (mean value over triplicate measurements) was assessed using BSA as a standard. The lysates were immediately used after Bradford quantitation.

Optimization of probe concentration for Halo-binding site saturation in vivo

The following procedure was used to identify the concentration of Ht-PreHNE(alkyne) that can saturate Halo protein binding site in vivo. All assays were performed under dim-red light. All plates of (densely packed, but not starved) worms were harvested with 3 mL of S buffer [6.45 mM K_2HPO_4, 43.6 mM KH_2PO_4, 100 mM NaCl, filter-sterilized (0.22 μm)], and the samples were pipetted into 15 mL falcon tubes using glass pipettes. [In terms of the number of worms, per each Click reaction condition, 3 x 10 cm plates of confluent worms (densely packed, but not starved) were typically used.] To wash away OP50, the tubes were centrifuged at 3000 x g for 2 min. The supernatant was removed, and the pellets were washed with 10 mL S buffer until the supernatant was clear. Worm pellets were resuspended in 1 mL S buffer, pooled then split equally into 15 ml falcon tubes. To prevent starvation, the following procedure was performed: 3 mL of a saturated OP50 culture was centrifuged and the resulting OP50 pellet was resuspended in 2.5 mL of S buffer. This resulting mixture was added to each of the falcon tubes above containing pelleted worms to fully resuspend the worms. In parallel, Ht-PreHNE(alkyne) was diluted in S buffer to prepare a 10x stock (1 mM). 500 μL, 250 μL, 120 μL, and 60 μL of this 1 mM stock solution were added to the samples above to render a gradient of final concentrations. The final volume of each condition was made up to 5.0 mL by adding S buffer [respectively, to give final concentrations of Ht-PreHNE(alkyne), as follows: 100 μM, 50 μM, 25 μM, and 12 μM]. After 6 hours of incubation involving end-to-end rotation under dim-red light at room temperature, the samples were washed twice (each time with 10 mL S buffer) and a third time with 50 mM HEPES (pH = 7.6), each wash/rotation lasting 30 minutes. Between each wash, the worms were pelleted by centrifugation at 3000 x g for 2 min. Subsequently, the samples were transferred into 1.5 mL tubes and pelleted, then flash-frozen in liquid nitrogen. The resulting pellets could be kept at -80 °C, for up to 1 week. Worm pellets were lysed (see section 'worm lysis'), and lysates were made to a concentration of 1 mg/mL and treated with 10 μM of Halo-TMR and incubated at 37 °C for 30 min. 10 μL 4X Laemmli buffer with 6% BME was added to quench the reaction. The tubes were either stored at –80 °C, protected from light, or directly analyzed by SDS-PAGE. For each Click reaction condition, 3 x 10 cm plates of (densely packed, but not starved) worms were used.

Precision localized electrophile delivery in tissue-specific Halo transgenic C. elegans

For technical controls deployed (i.e., independent experiments that offer meaningful comparisons in terms of effects of probe, UV light, etc., in non-targeted backgrounds), please refer to main text discussion and individual figure legends. All plates of (densely packed, but not starved) worms were washed with 3 mL of S buffer, and the samples were pipetted into 15 mL falcon tubes using glass pipettes. The samples were centrifuged at 3000 x g for 2 min. The supernatant was removed, and the pellets were washed with 10 mL S buffer until the supernatant was clear. Worm pellets were resuspended in 1 mL S buffer, pooled then split equally into 15 ml falcon tubes. 6 mL of a saturated OP50 culture was centrifuged and resuspended in 5 mL of S buffer per tube. To prevent starvation, the OP50 in S buffer was added to each tube, as described in the section above. Afterwards, Ht-PreHNE(alkyne) was diluted in S buffer to make a 10x stock (120 μM), and 1000 μL of this solution was added to the samples. The final volume for each condition was made up to 10.0 mL by adding S buffer. [The final concentration of Ht-PreHNE(alkyne) was 12 μM]. After 6 hours of incubation involving end-to-end rotation under dim-red light at room temperature, the samples were washed twice (each time with 10 mL S buffer) and a third time with 50 mM HEPES (pH = 7.6). Each wash/incubation lasted 30 minutes. Between each wash, the worms were pelleted by centrifugation at 3000 x g for 2 min. Subsequently, the samples were transferred to a 6-well plate. The experimental group and the control group (as described in Figure 1B and elsewhere) were placed under a UV lamp (366 nm, 5 mW/cm^2) for 5 min.

Then the samples were transferred to 1.5 mL tubes and pelleted, and flash-frozen in liquid nitrogen. The resulting pellets could be kept at -80 °C for up to 1 week.

***Time-dependent photo-uncaging assay* in vivo**

Following Ht-PreHNE(alkyne) treatment and washing steps as described in the section above, worm samples were placed under a UV lamp (366 nm, 5 mW/cm^2) for 0, 1, 3, 5, and 15 min. The protein concentration of lysates (assessed by Bradford assay described elsewhere) was normalized to 1 mg / mL in 200 μL. 250 μL 5x stock Click mixture for 1250 μL total reaction volume was prepared by mixing 62.6 μL 20% SDS, 62.6 μL t-BuOH, 12.5 μL 100 mM $CuSO_4$, 12.5 μL Cu(II)TBTA (10 mM in 55% DMSO), 50 μL 50 mM HEPES (pH = 7.6), 25 μL 500 μM Cy5-azide. 25 μL of 100 mM TCEP stock solution [freshly prepared in Argon-saturated 500 mM HEPES (pH = 7.0)] was added just before use. 50 μL of 5x Click mixture was added to 200 μL of 1 mg/mL lysates. The final concentration of Click reaction components were 1% SDS, 5% t-BuOH, 1 mM $CuSO_4$, 0.1 mM Cu (II)TBTA, 2 mM TCEP, 10 μM Cy5-azide in 250 μL samples. The samples were incubated at 37 °C for 30 minutes following vortexing (a few seconds). 30 μL samples were pipetted to new 1.5 mL tubes. 10 μL 4x Laemmli dye with 6% BME was added to each tube to quench the reaction. The samples were subjected to in-gel fluorescence analysis.

Biotin-Click pulldown for enrichment of tissue-specific electrophile-sensor proteins

For each pulldown assay for target enrichment, 6 x 10 cm plates were used per condition. (Typically, the volume of worm pellets obtained from 6 x 10 cm plates is 100 μL.) Final lysate concentration and volume of the lysates were standardized to 2.5 mg/mL and 1000 μL, respectively. 100 μL bed volume of pre-rinsed streptavidin beads were prepared with 1 mL ddH_2O then 2x 1 mL 0.5% LDS in 50 mM HEPES (pH = 7.6) by end-to-end rotation for 5 min. Between each step, the beads were pelleted by 500 x g centrifuge for 1 min and the supernatant was removed. Subsequently, the samples were added to the beads. After 2 h incubation on a rotator at room temperature, tubes were centrifuged at 2000 x g for 1 min and lysate was removed from the beads.

1.25mL of 5x Click mixture for 6.25 mL total volume was prepared by mixing 313 μL of assay buffer containing in final concentration: 20% SDS, 313 μL t-BuOH, 62.5 μL 100 mM $CuSO_4$, 62.5 μL 10 mM Cu(II)TBTA in 55% DMSO, 361.5 μL 50 mM HEPES (pH = 7.6), 12.5 μL 100 mM biotin azide. 125 μL of 100 mM TCEP [freshly prepared in argon-saturated 500 mM HEPES (pH = 7.0)] was added just before use. 250 μL of 5x Click mixture was added to 1000 μL 2.5 mg/mL lysates. The final concentration of Click components in the assay mixture were: 1% SDS, 5% t-BuOH, 1 mM $CuSO_4$, 0.1 mM Cu(II)TBTA, 2 mM TCEP, and 200 μM biotin azide. The mixture was incubated at 37 °C for 30 min after vortexing (a few seconds). Subsequently, 4x volume of pre-chilled (-20 °C) pure ethanol was added to each lysate, followed by storage at -80 °C, from overnight to 3 days.

After precipitation, the samples were centrifuged at 20,000 x g for 30 min at 4 °C. The supernatant was removed, and the pellets were washed twice with 1 mL ice-cold 70% ethanol by vortexing for 1 minute, then one wash with acetone. Between each wash, the proteins were pelleted by 20,000 x g, at 4 °C for 10 min. Following the last wash, acetone was removed and evaporated. Next, 80 μL of resuspension buffer: 8% LDS and 1 mM EDTA in 50 mM HEPES (pH = 7.6) was added to each pellet. The pellets were resolubilized by vortexing and sonicating using Bioruptor® Pico sonication device (cat. # B01060010) over 10 minutes. This process was repeated until the pellets were fully solubilized. Samples were diluted with 50 mM HEPES (pH = 7.6) to a final concentration of 0.5% LDS and centrifuged at 20,000 x g for 10 minutes. 30 μL sample was removed and treated with 10 μL 4 x Laemmli dye to be used as an input sample.

The remaining samples were moved to a fresh tube with 50 μL bed-volume of streptavidin beads that had been washed with 250 μL of ddH2O (washed twice) followed by 250 μL of buffer [50 mM Hepes (pH 7.6) (final wash). After 2 h incubation on a rotator at room temperature, the samples were spun down at 2000 x g for 1 min and a small sample (30 μL) of supernatant was removed and treated with 10 μL 4 x Laemmli dye to be used as a flow-through sample. The beads were washed 3 times with 1 mL 0.5% LDS for 30 minutes at room temperature then centrifuged at 500 x g for 5 min, room temperature. After all of the wash buffer, including residual amount, was carefully removed, 30 μL of 2 x Laemmli dye with 6% BME was added to beads. Then the samples were boiled for 10 min at 98 °C, then centrifuged at 20,000 x g for 5 min. The supernatant was removed as the elution sample.

Optimization of external biotin treatment time and dose for OS-Ultra-ID biotinylation activity saturation in live C. elegans

For all OS-Ultra-ID-assocaited experiments, 20 healthy transgenic adults (P_0) were picked onto standard 10 cm NGM plates. After the plates were full of the F_2 progeny (not starved) at the larval stage, all worms were collected and then redistributed to freshly-made MG1655:BioBKan plates as a 1 to 6 ratio of 10 cm plates (i.e., 1 plate to 6 plates). The following procedure was used to identify the external biotin treatment time and dose that can saturate biotinylation activity in vivo. All assays were performed under dim-red light. All plates of (densely packed, but not starved) worms were harvested with 3 mL of S buffer [6.45 mM K_2HPO_4, 43.6 mM KH_2PO_4, 100 mM NaCl, filter-sterilized (0.22 μm)], and the samples were pipetted into 15 mL falcon tubes using glass pipettes. [In terms of the number of worms, per each condition, one 10 cm plate of confluent worms (densely packed, but not starved) was typically used.] To wash away MG1655:BioBKan, the tubes were centrifuged at 3000 x g for 2 min. The supernatant was removed, and the pellets were washed with 10 mL S buffer until the supernatant was clear. Worm pellets were resuspended in 1 mL S buffer, pooled then split equally into Eppendorf tubes. To prevent starvation, the following procedure was performed: 10 mL of a saturated OP50 culture was centrifuged and the resulting OP50 pellet was resuspended in 2.5 mL of S buffer. 250 μL of this resulting 4x mixture was added to each of the Eppendorf tubes above containing pelleted worms to fully resuspend the worms. In parallel, biotin was diluted/resuspended in S buffer to prepare a 4x stock. This stock solution was added to the samples above to render a gradient of final concentrations as 0, 0.2, 1, 5, and 25 mM. The final volume of each condition was made up to 1.0 mL by adding S buffer. After 0.5, 1, 2,

and 4 hours of incubation involving end-to-end rotation under dim-red light at room temperature, the samples were washed twice (each time with 1 mL S buffer) and a third time with 50 mM HEPES (pH = 7.6), each wash/rotation lasting 30 minutes. Between each wash, the worms were pelleted by centrifugation at 3000 x g for 2 min. Subsequently, the samples were flash-frozen in liquid nitrogen. The resulting pellets could be kept at -80 °C, for up to 1 week. Worm pellets were lysed (see section 'worm lysis'), and lysates were made to a concentration of 1.25 mg/mL. 4X Laemmli buffer with 6% BME was added before being loaded onto gel and analyzed by streptavidin blot.

Biotinylated protein enrichment for OS-Ultra-ID strains

For all OS-Ultra-ID-associated experiments, 20 healthy transgenic adults (P_0) were picked onto normal 10 cm NGM plates. After the plates were full of the F_2 progeny (not starved) at the larval stage, all worms were collected and then redistributed to freshly-made MG1655:BioBKan plates as a 1 to 6 ratio of 10 cm plates (1 plate to 6 plates). (*Note*: Biotin deficiency limits the number of F_2 progeny that could be raised from 20 P_0 adults in MG1655:BioBKan plates). In terms of the amount of worms, per each mass-spec sample, 6 x 10 cm plates of confluent worms (densely packed, but not starved) were typically used. The external biotin treatment concentration was 5 mM and the time was 4 hours. The other procedural steps were similar to those described above. After the worm lysis and protein concentration normalization, 30 μL sample was removed and treated with 10 μL 4 x Laemmli dye to be used as an input sample for LFQ analysis. The input samples were collected for the streptavidin blot analysis. The remaining lysates were moved to a fresh tube with 50 μL (bed-volume) of streptavidin beads that had been washed with 250 μL of ddH_2O (washed twice) followed by 250 μL of buffer [50 mM Hepes (pH 7.6) (final wash). After 2 h incubation on a rotator at room temperature, the samples were spun down at 2000 x g for 1 min and a small sample (30 μL) of supernatant was removed and treated with 10 μL 4 x Laemmli dye to be used as a flow-through sample. The beads were washed 3 times with 1 mL 0.5% LDS for 30 minutes at room temperature then centrifuged at 500 x g for 5 min, at room temperature. After all of the wash buffer, including residual amount, was carefully removed, 30 μL of 2 x Laemmli dye with 6% BME was added to beads. Then the samples were boiled for 10 min at 98 °C, then centrifuged at 20,000 x g for 5 min. The supernatant was removed as the elution sample for TMT-11plex analysis.

Mass spectrometry sample preparation in OS-Localis-REX and OS-Ultra-ID experiments

For OS-Localis-REX samples, following the biotin-click pulldown, all elution samples were loaded into separate wells of a home-made 11% SDS-PAGE gel and were run until the dye-front had penetrated 1-2 cm into the gel to desalt the samples. For OS-UltraID samples, the samples were loaded into Novex™ Tris-Glycine mini protein gels. The gel was cut into small pieces which were washed twice in 50% ethanol and 50 mM ammonium bicarbonate (AB) for 20 min and dried by vacuum centrifugation. Sample reduction was performed with 10 mM DTT for 1 h at 56°C. A washing-drying step as described above was repeated prior to alkylation with 55 mM Iodoacetamide for 45 min at 37°C in the dark. Samples were washed and dried again and digested overnight at 37°C using Mass Spectrometry grade Typsin at a concentration of 12.5 ng/μL in 50 mM AB and 10 mM $CaCl_2$. Resulting peptides were extracted in 70% ethanol, 5% formic acid twice for 20 min with permanent shaking. Samples were further dried by vacuum centrifugation and stored at -20 °C. Peptides were desalted on C18 StageTips and dried by vacuum centrifugation. For TMT labeling, peptides were first reconstituted in 8 μL HEPES 100 mM (pH 8.5) and 3 μL of TMT solution (20 μg/μL in pure acetonitrile) was then added. Labeling was performed at room temperature for 1.5 h and reactions were quenched with hydroxylamine to a final concentration of 0.4% (v/v) for 15 min. TMT-labeled samples were then pooled at a 1:1 ratio across all samples. The combined sample was vacuum centrifuged near dryness and subjected to fractionation using the Pierce High pH Reversed-Phase Peptide Fractionation Kit following the manufacturer's instructions.

Mass spectrometry data analysis in OS-Localis-REX and OS-Ultra-ID experiments

The individual samples for LFQ analysis of the whole-proteome abundance in individual OS-Ultra-ID worms, or the resulting 12 fractions for TMT analysis of tissue-specific abundance identification within individual OS-Ultra-ID worms, the resulting fractions were resuspended in 2% acetonitrile, 0.1% FA and nano-flow separations were performed on a Dionex Ultimate 3000 RSLC nano UPLC system (Thermo Fischer Scientific) on-line connected with a Qexactive HF Orbitrap mass spectrometer (Thermo Fischer Scientific). A capillary precolumn (Acclaim Pepmap C18, 3 μm-100Å, 2 cm x 75μm ID) was used for sample trapping and cleaning. A 50cm long capillary column (75 μm ID; in-house packed using ReproSil-Pur C18-AQ 1.9 μm silica beads) was then used for analytical separations at 250 nl/min over 150 min biphasic gradients. Acquisitions were performed through Data-Dependent Acquisition (DDA). First MS scans were acquired with a resolution (ion mass/mass peak width) of 120,000 (at 200 m/z) and the 15 most intense parent ions were then selected and fragmented by High energy Collision Dissociation (HCD) with a Normalized Collision Energy (NCE) of 32% using an isolation window of 0.7 m/z. Fragmented ions were acquired with a resolution of 30,000 (at 200 m/z) and selected ions were then excluded for the following 40 s.

For OS-Localis-REX, the raw data were processed using MaxQuant 1.6.8.0 against a concatenated database consisting of the UniProt *C. elegans* complete reference proteome (26991 entries_LM190929) and a HaloTag-GFP protein. For OS-Ultra-ID, the raw data were processed using MaxQuant 2.4.4.0 against a concatenated database consisting of the UniProt *C. elegans* complete reference proteome (26695 entries_LM240314) and a mcherryUltraID protein. Carbamidomethylation was set as fixed modification, whereas oxidation (M), phosphorylation (S, T, Y), acetylation (Protein N-term) and glutamine to pyroglutamate were considered as variable modifications. A maximum of two missed cleavages were allowed and "Match between runs" option was enabled. For LFQ data from whole-proteome abundance analysis of individual OS-Ultra-ID strains, proteins with at least 2 valid values in at least one group were kept for the following analysis: imputation of missing values is performed following a normal distribution

with a width = 0.3 and a down-shift = 1.8. For TMT data analysis of tissue-specific abundance from individual OS-Ultra-ID strains, a minimum of 2 unique peptides (in OS-Localis-REX) or 1 unique peptide (in OS-UltraID) were required for protein identification and the false discovery rate (FDR) cutoff was set to 0.01 for both peptides and proteins. Hits were further selected using criteria described in main text. See also Figures S1I and S2F.

Age synchronization of C. elegans

For synchronization, 3 x 10 cm plates of indicated worm strains were used. All plates were harvested using 5 mL of M9 media [5.8 g $Na_2HPO_4 \cdot 7H_2O$ (22 mM); 3.0 g KH_2PO_4 (22 mM); 5.0 g NaCl (86 mM); 0.25g $MgSO_4 \cdot 7H_2O$ (1.0 mM) for 1 L, that had been filter-sterilized (0.22 μm) before use]. The samples were pipetted into a 15 mL falcon tube using glass pipettes. The tube was centrifuged at 2000 x g for 1 min to pellet the worms. After aspirating the supernatant media, 15 mL of fresh 20% alkaline hypochlorite solution (3.0 mL bleach, 3.75 mL 1 M NaOH and 8.25 mL ddH_2O) was added to the tube. Once most of the worm bodies had dissolved (typically after 5 minutes of end-to-end rotation), the M9 media was added to fill the tube and then the tube was centrifuged at 4000 x g for 1 min to pellet the eggs. After aspirating the hypochlorite solution, the pellet was washed with 3 x 10 mL M9 media. Subsequently, the pellet was resuspended with 7 mL M9 media and incubated overnight at room temperature with gentle rocking to hatch the eggs. The L1 worms were distributed onto 3 x 10 cm plates the next day.

RNA interference assay in *C. elegans*

The previously reported procedures were followed. Briefly, the normal nematode growth medium (NGM-agarose) was prepared as described elsewhere. After autoclaving and cooling to 50–60 °C, 1 mL of 5 mg/L cholesterol in EtOH, 1 mL of 1 M IPTG, and antibiotics (ampicillin, 50 μg/mL) were added. For 10 cm plates, 15 mL NGM-agarose media was pipetted using sterile procedures. The respective Ahringer's dsRNA-encoding plasmids or L4440 empty vector were transformed into HT115 competent cells and were grown in LB/Ampicillin (50 μg/mL) at 37 °C overnight. The concentrated bacterial culture was then seeded onto the NGM plates with IPTG and left to dry at room temperature for overnight induction of dsRNA expression. Synchronized L1 worms were raised on these plates (for targeted knockdown) at 22 °C for 40-48 hours.

RNA isolation and reverse transcription

Synchronized late L4 worms were collected from RNAi plates and washed 3 times with M9 media to remove bacteria. The worms were then resuspended in 1 mL TRIzol™ reagent and homogenized. Samples were used immediately for RNA isolation or stored at -80 °C until further use. To isolate the RNA, 0.2 mL of chloroform was added to 1 mL TRIzol™ reagent then mixed by shaking. After incubation for 2-3 min, the samples were centrifuged at 12000 x g at 4 °C for 15 min. The aqueous phase containing RNA was transformed into a new Eppendorf tube. 0.5 mL of isopropanol was added to precipitate the RNA. The aqueous phase was incubated with isopropanol for 10 min at 4 °C and then centrifuged at 12000 x g at 4 °C for 10 min. After discarding the supernatant, the RNA pellet was washed with 1 mL 75% (v/v) ethanol. The samples were vortexed briefly before centrifugation at 7500 x g at 4 °C for 5 min. The resulting pellet was resuspended with 20-50 μL Rnase-free water. Extracted RNA was quality-controlled by Agarose gel electrophoresis analysis and concentration was determined by A_{260nm} using a BioTek Cytation3 microplate reader with a Take3 accessory. cDNA was synthesized with reverse transcription kits using RNaseOUT™ Recombinant Ribonuclease Inhibitor and Superscript™ III Reverse Transcriptase.

Quantitative real-time PCR (qRT-PCR)

For each sample (and associated technical and biological replicates as described in figure legends), PCR was performed using iQ SYBR Green Supermix (Bio-Rad) and primers specific to the gene of interest following the manufacturer's protocol. Amplicons were chosen that were around 200 bp in length and had no predicted off-target binding predicted by NCBI Primer BLAST. For genes with multiple splice variants, primers were chosen that amplified conserved sequences across all splice variants. Primers were validated using standard curves generated by amplification of serially-diluted cDNA; primers with a standard curve slope between –0.8 and 1.2 and $R^2 \geq 0.97$ were considered acceptable. Single PCR products were confirmed by melting analysis following the PCR protocol. Quantitative PCR data was carried out using QuantStudio™ 7 Pro. Samples with a threshold cycle >35 or without a single, correct melting point were not included in data analysis. Normalization was carried out using a single housekeeping gene (β-actin) as indicated in each dataset and the $\Delta\Delta C_t$ method. See Methods S1 for primer sequences.

Scoring of fertilized eggs laid by C. elegans

Plates for RNAi-targeted knockdown (6 cm, 8 mL of NGM-media) were prepared as described elsewhere. For each phenotypic assay, 12 L4-young adult worms were picked from 10 cm plates (subjected to RNAi), at the end of 40 hours post plating of L1. The worms were transferred individually to 6 cm plates (subjected to RNAi). On the morning and the evening of Day 1 and 2 post plating of L1, the worms were transferred to fresh 6 cm plates (subjected to RNAi), and further on each subsequent evening, until no new eggs were observed. The number of eggs was counted at specific time intervals - 3 times on Days 1 and 2; 2 times on Days 3 and 4, once on subsequent days, until no new eggs were observed. All counted eggs were validated as healthy embryos by assessment of hatching.

C. elegans *viability analysis*

RNAi-fed worms (from 6 cm plate size, prepared using 8 mL of NGM-media) were prepared as described above. For each phenotypic assay, 10 L4-young adult worms were picked from 10 cm RNAi plates 40 hours post plating of L1, and were transferred individually to 6 cm RNAi plates. The worms were monitored for their survival. The worms were transferred to fresh 6 cm RNAi plates in the morning

and the evening of Day 1 and Day 2; and in the evening of subsequent days, until no new eggs were observed. A worm was considered dead if no response was observed after 3 gentle touches on the head with a platinum pick and it displayed no pharyngeal pumping.

C. elegans body bend assay

RNAi-fed worms (from 6 cm plate size, prepared using 8 mL of NGM-media) were prepared as described elsewhere. For each phenotypic assay, 10 L4-young adult worms were picked from 10 cm RNAi plates 40 hours post plating of L1, and were transferred individually to 6 cm RNAi plates. The number of bends at the pharynx was counted for 2 minutes for every worm, every alternate day until death. Data were recorded only when the worm was away from the edges of the bacterial food lawn. The worms were transferred to fresh 6 cm RNAi plates in the morning and the evening of Day 1 and Day 2; only in the evening of subsequent days until no new eggs were observed.

C. elegans egg-laying assay

RNAi-fed worms (from 6 cm plate size, prepared using 8 mL of NGM-media) were prepared as described elsewhere. For each phenotypic assay, 3 x 10 cm plates were prepared and synchronized L1 worms were raised on them for 40 hours at 22 °C. The worms were then collected and washed 3 times with M9 media to remove bacteria. The worms were then resuspended in 0.5 mL M9 media and transferred to 1.5 mL tubes. HNE-alkyne-functionalized (in vehicle DMSO) master stock solution was prepared in M9 media and added to each tube such that final concentration was 2 mM in final volume of 0.7 mL. For each HNE-alkyne-treatment condition, corresponding final volume of DMSO vehicle was used as a control. After one hour of incubation involving end-to-end rotation, samples were washed 3 times with 0.5 mL M9 media and resuspended in 0.2 mL M9 media. These worm suspensions were seeded onto freshly-prepared RNAi plates. The worms were allowed to revive for 4 hours at 20 °C. 12 L4-young adult worms were then picked from these RNAi plates and transferred individually to 6 cm RNAi plates. On the next evening (Day 2), the worms were transferred to fresh 6 cm RNAi plates, and subsequent transfers were performed in the morning and evening of Days 2-3; and on the evening of subsequent days until no new eggs were observed. The number of eggs was counted at specific time intervals - 3 times on Days 1-2; 2 times on Days 3-4; once on subsequent days until no new eggs were observed.

C. elegans food race assay

Food race plates were prepared at least two days prior to experiment, which were NGM plates with 50 μL of OP50 seeded as a dot 1 cm away from the edge of the plate on the equator, as established and described. Large population of worms was bleached-synchronized and recovered on either NGM plates or RNAi plates (10 cm plates, as described elsewhere) at 22°C for 40 hours. The worms were then collected and treated by different doses of HNE(alkyne) or by the equivalent volume of its vehicle solvent in M9 buffer for 1 hour with end-to-end rotation, washed 3 times by M9, and recovered on NGM plates for 4 hours. The worms were then collected again and transferred to a marked position also 1 cm away from the edge of the plate on the opposite side of the OP-50 lawn on the equator drop-wise. The timer starts when the M9 has evaporated, and the number of worms that have reached the lawn was recorded at 30, 60, 90, and 120 min, and the next day, matched against the total number of alive worms.

C. elegans defecation assay

RNAi-fed worms (from 10 cm plate size, prepared using 15 mL of NGM media) were prepared as described elsewhere. The food lawn was normalized to a 1.2 OD value before being seeded on the NGM media specially for this assay. For each phenotypic assay group, two 10 cm plates were prepared and synchronized L1 worms from the same pool were raised on these plates for 48 hours at 22 °C. The half worms were for imaging without the treatment. For each condition, 12 individual worms are recorded individually for 10 x defecation cycles by Leica M205 FA microscope. The other half worms were then collected and resuspended in 0.5 mL M9 media and transferred to 1.5 mL tubes. HNE-alkyne-functionalized (in vehicle DMSO) master stock solution was prepared in M9 media and added to each tube such that the final concentration was 2 mM in a final volume of 0.75 mL. For each HNE-alkyne-treatment condition, the corresponding final volume of DMSO vehicle was used as a control. After one hour of incubation involving end-to-end rotation, samples were washed 3 times with 0.5 mL M9 media and resuspended in 0.2 mL M9 media. These worm suspensions were seeded onto freshly prepared 10 cm RNAi plates. The worms were cultured at 20 °C afterward. 16 hours later, 20 worms are recorded individually for 6 x defecation cycles for each condition. The defecation cycle was determined by intervals between two pBoc behaviors.

C. elegans male induction and crossing

20 x L4-young adult hermaphrodites were picked onto 2-3 x 10 cm plates, which were incubated for 6 hours at 31 °C afterward. The plates were transferred to 20 °C until the healthy F1 worms grew after the induction. Then all the males were picked to another 6 cm plate with healthy L4-young hermaphrodites at a 3:1 to 4:1 ratio. The males from the next generation were used for crossing. The hermaphrodites from another strain were picked together with these males to 35 mm plates for crossing at a similar male-to-hermaphrodite ratio. After 3 days, heterozygous F1 worms from crossing were picked to fresh 35 mm plates individually to ensure their self-crossing. Subsequently, 16-20 x hermaphrodite F2 worms were picked to 35 mm plates separately. Once enough F3 progenies from F2 self-crossing were observed on the plates, the F2 mothers were picked out and checked by single worm PCR. 10 x individual F3 worms were picked and checked by single worm PCR to ensure the homozygosity from the F2 mother containing the target transgene or mutation. Sometimes more self-crossing steps were required depending on the F3 homozygosity. Only the homozygous worms would be used for subsequent experiments. All crossing and culture temperatures are 20 °C.

Single worm PCR

Single adult worms were picked into a 10 μL worm digestion buffer in a PCR tube (1X HF buffer, 0.5 mg/mL proteinase K). The tubes were spun down at 14000 g for 15 seconds before digestion. The worms were digested by flash-freezing in liquid nitrogen for 10 min followed by a 90-minute incubation at 65 °C and a 15-minute protease K inactivation at 95 °C. Then the mixture was used directly for PCR as the template. For the PCR reaction, 2 μL DMSO, 0.2 μM corresponding primer pair, 0.2 mM dNTPs mixture, and 0.04U/ μL Phusion polymerase were added to a final volume at 50 μL 1X HF buffer. The PCR cycle was set to 98 °C for 50 seconds, and 30 times 98 °C for 10s; 53 °C for 30 seconds; 72 °C for 45 seconds. After the PCR reaction, the product was checked with 1% agarose in NEB buffer. DNA electrophoresis gel and Sanger sequencing after cleaning with the PCR clean-up kit, if necessary.

Lipid droplet imaging

RNAi-fed worms containing dhs-3p::dhs-3::gfp transgene (from 10 cm plate size, prepared using 15 mL of NGM-media) were prepared as described elsewhere. For each phenotypic assay group, one 10 cm plate was prepared and synchronized L1 worms from the same pool were raised on these plates for 48 hours at 22 °C. The worms were then collected and resuspended in 0.5 mL M9 media and transferred to 1.5 mL tubes. HNE-alkyne-functionalized or its reduced version DHN; oxidized version HNA (in vehicle DMSO) master stock solution was prepared in M9 media and added to each tube such that the final concentration was 2 mM in a final volume of 0.75 mL. For each small-molecule-treatment condition, the corresponding final volume of DMSO vehicle was used as a control. After one hour of incubation involving end-to-end rotation, samples were washed 3 times with 0.5 mL M9 media and resuspended in 0.2 mL M9 media. These worm suspensions were seeded onto freshly prepared 10 cm RNAi plates. The worms were cultured at 20 °C afterward. 16 hours later, individual worms were picked and imaged under both stereo objective and 5x HR objective (Leica FluoCombi III) with a Leica M205 FA microscope. For Oil Red O staining experiments, instead of imaging the worms directly, the worms were collected by M9 to 1.5 mL tubes and washed 3 times. Worm pellets without supernatant were fixed by adding 500 μL 60% isopropanol. 500 μL freshly 0.45-μm filtered 0.3% Oil Red O in 60% isopropanol (by mixing 0.5% Oil Red O in 100% isopropanol and ddH_2O the day before) was added to the worms to enable the staining. After 18 hours of end-to-end rotation at 25 °C in a wet chamber (web paper towels and aluminum foil covered), the supernatant was removed. The remaining worm pellets were washed with 500 μL 60% isopropanol twice and then added with 250 μL 0.01% Triton X-100 in S-basal buffer. Stained worms can be imaged or stored at 4 °C for a month. The GFP signals were quantified by selecting the intestinal region and analyzed in Fiji ImageJ 1.53f51 under the 5x HR objective mode. The Oil Red O images were taken under the RGB mode with the 5x HR objective; the signals were quantified by selecting the body region (without the pharynx) in the blue channel after inverting the images in Fiji ImageJ 1.53f51.

C. elegans immunofluorescent imaging following bulk HNE treatment

Healthy, age-synchronized L4-young adult worms single adult worms were collected, suspended in 0.5 mL M9 media, and transferred to 1.5 mL tubes. HNE-alkyne-functionalized (in vehicle DMSO) master stock solution was prepared in M9 media and added to each tube such that the final concentration was 2 mM in a final volume of 0.75 mL. For each HNE-alkyne-treatment condition, the corresponding final volume of DMSO vehicle was used as a control. After one hour of incubation involving end-to-end rotation, samples were washed 3 times with 0.5 mL M9 media and fixed in 1 mL 4% paraformaldehyde overnight with gentle end-to-end rotation at 4 °C. After pelleting at 2000x g and removal of paraformaldehyde, the worms were incubated in methanol at -20 °C for 24 h. Subsequently, the worms were washed for 30 min each, twice with PBS including 0.015% Tween-20, and twice with 50 mM HEPES buffer including 150 mM NaCl, pH = 7.6. The signal of alkyne functionalized HNE was visualized by click reaction: the worms were incubated in the freshly made cocktail click mixture, with the final concentration containing 50 mM HEPES (pH = 7.6), 150 mM NaCl, t-BuOH (5%), CuSO4 (1 mM), Cu(II)TBTA (0.1 mM), TCEP [2 mM; made as a 100 mM stock in 500 mM HEPES (pH 7.6)] and Cy5-azide (10 μM). The TCEP was added at the end of the mixture preparation. The worms were incubated at room temperature in the Eppendorf thermomixer at 300 g for 1 hour. Afterward, the samples were washed 3 times in PBS including 0.015% Tween-20, and then incubated overnight with gentle end-to-end rotation at 4 °C. For the subsequent incubation with antibodies, the worms need to be washed twice in 1 mL PDT buffer (PBS, 0.1% Tween-20, 1% DMSO) for 30 min each at room temperature and blocked in 1 mL blocking solution (PBS, 0.05% Tween-20, 10% v/v FBS, 2% w/v BSA) for 1 hour at room temperature. After the blocking, the worms were incubated with goat anti-GFP (B2) (Abcam, ab6673) solution (1:500 in blocking solution) at 4 °C overnight. Similarly, the worms were washed twice in 1 mL PDT buffer (PBS, 0.1% Tween-20, 1% DMSO) for 30 min each at room temperature and blocked in 1 mL blocking solution (PBS, 0.05% Tween-20, 10% v/v FBS, 2% w/v BSA) for 1 hour at room temperature. Then Donkey pAb to Goat IgG AlexaFluor 488-conjugated (Abcam, ab150133) solution (1:500 in blocking solution) was added to the samples and incubated for 1.5 hours. After 3 times washing in 1 mL PDT buffer, 30 min each at room temperature, the worms were imaged under both stereo objective and 5x HR objective (Leica FluoCombi III) with a Leica M205 FA microscope. The fluorescent signals were quantified by selecting the intestinal region and analyzed in Fiji ImageJ 1.53f51 under the 5x HR objective mode.

Cell growth, transfection, and targetable electrophile sensing test (T-REX)

HKE293T and Hela cells were maintained in 1 x MEM + Glutamax media supplemented with 10% FBS, 1× NEAA, 1× sodium pyruvate, and 1× Pen-Strep in 60 mm growth factor treated plates. When the cell density was ~70%, cells were transfected with specific halo-POI plasmid using TransIT-2020 transfection reagent per the manufacturer's recommendation. All subsequent steps were done under a dim-red light. 36 hours after transfection, the cells were treated with 15 μM Ht-PreHNE(alkyne) in serum-free media and

incubated for 2 h, followed by gentle rinsing with serum-free media three times every 30 min over the next 1.5 h. The preheated UV light (10-min on before using, 365 nm, ~5 mW/cm^2) was placed 2 cm above the sample for 5 min for photo-uncaging alkyne functionalized HNE. The lids of cultural dishes were removed during the irradiation. Afterward, cells were harvested by TrypLE express enzyme into 1.5 mL Eppendorf tubes, washed two times of ice-cold DPBS, once of 50 mM HEPES (pH = 7.6), and flash-frozen in liquid nitrogen. Cell pellets were lysed in 400 μL freshly prepared lysis buffer containing 50 mM HEPES (pH 7.6), 150 mM NaCl, 1% Triton-X100, 1× Roche cOmplete mini, EDTA-free protease inhibitor mixture, and 0.3 mM TCEP by rapid freeze-thaw and 15-seconds vortex for three times. The cell debris was removed by centrifugation at 20000 g for 30 min at 4 °C. Protein concentrations in cell lysate were determined to be 1.25 mg/mL using Bradford assay. Subsequent biotin-click pulldown steps are similar to methods in worms as described before.

Enzymatic activity test of CYP2A6 with HNE inhibition

Vivid™ CYP450 Screening Kit (PV6140) from ThermoFisher Scientific was used to test the enzymatic activity of CYP2A6. From 0.25 μM to 32 μM, a series of double concentrations of 3-cyano coumarin (substrate) was added to an opaque 96-well plate to determine the K_m. The enzyme concentration was 10 nM, with 30 μM NADPH in 100 μL reaction volume. The fluorescent signals at 460 nm were recorded every minute, over the course of 1 hour, using Cytation-5 multimode plate reader. The enzymatic reaction velocity was calculated by linear fitting of signals observed within the initial 20-minute period, the data from which were used for fitting to Michaelis-Menten kinetics and calculating the K_m. For HNE-inhibition assays, CYP2A6 was incubated with different concentrations of HNE or EtOH (vehicle) for 20 min, prior to addition of 30 μM NADPH and 100 μM 3-cyano coumarin, rendering final concentrations of CYP2A6 to be 10 nM, and HNE as indicated in corresponding figure, during the measurement of remaining enzyme activity. The fluorescent signals at 460 nm were recorded every minute, over the course of 1 hour, using Cytation-5 multimode plate reader. Enzymatic reaction velocity for subsequent fitting and analysis was calculated based on the data observed during the initial 30-minute period. See main text discussion and corresponding figure legends for the equations used.

Overexpression and enzymatic activity test of microsomal CYP2A6

HEK293 cells were transfected in 20*10^{6}cells /mL in RPMI1640 media (Thermo Fischer) with 0.1% pluronicF68 (Applicam). 15 μg sterile plasmids containing CYP2A6 mutants were added to 10 mL media for transfection. After mixing by shaking, 30 μg Pei-Max (Polyscience, Chemie Brunschwig) were added to the cells, mixed, and cultured at 37 °C with stirring for 1.5 hours. The cells were diluted to a concentration of 1*10^{6}cells/mL in Hycell TransFxH Media (Cytiva). After a 3-day culture with stirring at 37°C, cells were harvested by centrifugation. Cell pellets can either be kept at – 80 °C or lysed in 400 μL (For 5 mL media) 50 mM potassium phosphate buffer (pH =8.0), by rapid freeze-thaw and 15-second vortex three times. The supernatant was removed after centrifugation at 12000 g for 5 min at 4 °C. Protein concentration (c, mg/mL) normalization was based on the Bradford assay for the supernatant in each sample. The remaining cell debris was resuspended in 50 mM potassium phosphate buffer (pH =8.0) again, by matching the buffer volume to the corresponding protein concentrations in supernatant (volume of resuspending buffer = 40*c μL). The subsequent enzymatic activity test steps were similar to the commercial CYP450 Screening Kit as described elsewhere, by substituting the 10 nM enzyme to 50 μL CYP2A6 microsomes. For the activity test of different mutants, the 3-cyano coumarin deployed was 100 μM. For the HNE-inhibition assays, CYP2A6 microsomes were incubated with 400 μM HNE or EtOH (vehicle) for 20 min, prior to addition of 30 μM NADPH and 10 μM 3-cyano coumarin as the final concentration. CYP2A6 amount was determined by western blot analysis.

In vitro HNEylation of CYP2A6 for validation of HNEylation using Cy5 in-gel fluorescence analysis

Recombinant CYP2A6 (TP322995) from Origene was used to test the in vitro HNEylation of CYP2A6. Before the reaction, 90 μM HNE-alkyne and 1.8 μM CYP2A6 were preheated in a 37 °C metal bath. 15 μL CYP2A6 stock (final concentration: 1.5 μM) and 3 μL HNE-alkyne stock (final concentration: 15 μM) were mixed and incubated at 37 °C to start the reaction. 2 μL solution was pipetted to 28 μL ice-cold 50 mM HEPES with 1x Click mixture, at 0s, 15s, 30s, 60s, 90s, 120s, 180s, 240s after mixing. The final concentration for the click reaction contained 1% SDS, 50 mM HEPES (pH = 7.6), t-BuOH (5%), $CuSO_4$ (1 mM), Cu(II)TBTA (0.1 mM), TCEP [2 mM; made as a 100 mM stock in 500 mM HEPES (pH 7.6)] and Cy5-azide (10 μM). The mixture of the HNEylated CYP2A6 and click reagents was incubated at 37 °C for 30 min, followed by adding 12.5 μL 4x loading dye with 6% BME. The cy5 signals were read out by in-gel fluorescence and the protein amounts were read out by colloidal Coomassie blue staining. Gels were quantified in Fiji ImageJ 1.53f51 and the data relevant to time-dependent HNE modification was fitted to Y=0.020533 + (1-0.020533)*(1-exp(-k_{obs}'*x)) in GraphPad Prism. To enable comparison with the previously-reported electrophile-sensing rates of kinetically-privileged HNE-sensor proteins, The adjusted second-order observed rate constant of k_{obs}= (3.7 ± 0.8) x 10^8 $M^{-2}\cdot s^{-1}$ was derived by considering the concentration of the protein and HNE-alkyne as described in the main text and corresponding figure legends.

Sample preparation for HNEylation site identification by mass spectrometry

1 μM of recombinant CYP2A6 (Origene), approximately 2.83 μg in 45 μL, was prewarmed at 37°C on a shaker in a red light room for 5 min. 0.8 μM or 10 μM final concentration of in-house-synthesized HNE(alkyne) in DMSO was added to the protein (5 μL) for the final volume of 50 μL, and incubated for 5 min in a red light room. Samples were then resuspended in 4 M urea, diluted by 5 volumes of with 100 mM Tris-HCl pH 8, and digested overnight at 37°C by 1/20 w/w enzyme-to-protein ratio of mass spectrometry-grade trypsin. The reaction was stopped by the addition of formic acid and peptides were dried by vacuum centrifugation. Peptides were resuspended

in 0.1% TFA solution and were desalted in StageTips using 4 C18 disks (Empore 3M) based on the standard protocol.[86] Desalted peptides were dried down by vacuum centrifugation.

Mass spectrometry (MS) analysis for HNEylation site identification

The tryptic peptides were resuspended in 10 μL of 0.1% FA and 2% acetonitrile (Biosolve) for nano-LC-ESI-MS analysis, which was carried out using an Exploris 480 Orbitrap Mass Spectrometer (Thermo Fischer Scientific) coupled with a Dionex UltiMate 3000 RSLCTM (Thermo, Sunnyvale, CA). 2 μL were injected onto a capillary precolumn (Acclaim Pepmap C18, 3 μm-100Å, 2 cm x 75μm ID) for sample trapping and cleaning. A 50 cm long capillary column (75 μm ID; in-house packed using ReproSil-Pur C18-AQ 1.9 μm silica beads; Dr. Maisch) was then used for analytical separations at 250 nL/min over 90 min biphasic gradients. Acquisitions were performed through Top Speed Data-Dependent Acquisition mode using a cycle time of 2 seconds. First MS scans were acquired with a resolution of 120,000 (at 200 m/z) and the most intense parent ions were selected and fragmented by High energy Collision Dissociation (HCD) with a Normalized Collision Energy (NCE) of 30% using an isolation window of 2 m/z. Fragmented ions were acquired with a resolution of 30,000 (at 200m/z) and selected ions were then excluded for the following 20 s. All data were acquired under Xcalibur 3.0 operation software (Thermo-Fisher Scientific).

Data analysis for digest-MS-based HNEylation site identification

All MS and MS/MS raw spectra were processed by Proteome Discoverer v2.5 (Thermo Fisher Scientific). Database search was performed against the *H. Sapiens* Uniprot database (UP000005640, revised on 2023 Oct 19) with 82,685 entries and 20,596 genes. Parent mass tolerance was set at 10.0 ppm and fragment mass tolerance was set to 0.05 Da, with search type set to monoisotopic and maximum number of missed cleavages of 2. Variable modifications were set with N-terminal acetylation, carbamidomethylation, and pyro-Q to E. In addition to these, variable modifications of HNE(alkyne) ($C_9H_{12}O_2$, Mmi 152.0837), reduced HNE(alkyne) ($C_9H_{14}O_2$, Mmi 154.0994), dehydrated HNE(alkyne) ($C_9H_{10}O$, Mmi 134.0732), and reduced and dehydrated HNE(alkyne) ($C_9H_{12}O$, Mmi 136.0888) for Cys, His, and Lys were added. Peptide identifications were accepted if they could be established at greater than 84.0% probability to achieve an FDR less than 1.0% by the Percolator posterior error probability calculation. Protein identifications were accepted if they could be established at greater than 99.0% probability to achieve an FDR less than 1.0% and contained at least 2 identified peptides. Protein probabilities were assigned by the Protein Prophet algorithm. Proteins that contained similar peptides and could not be differentiated based on MS/MS analysis alone were grouped to satisfy the principles of parsimony. Scaffold (Scaffold v5.3.1, Proteome Software Inc., Portland, OR) was used to validate MS/MS-based peptide and protein identifications.

In vitro reaction of CYP2A6-mediated HNE(alkyne) turnover, and preparation for product identification by mass spectrometry

The procedure was modified from previous published methods, using reagents from CYP2A6 Vivid Blue Screening Kit (Cat #PV6140). Reaction volume was 20 μL per tube, each containing 10 μL 1 μM CYP2A6 Baculosomes (final 0.5 μM) and 10 μL master mix of 1X Vivid P450 Buffer (final 0.5X), 3.0 mM NADPH (final 1.5 mM), 10.0, 3.0, and 1.0 mM of HNE (final 5.0, 1.5, and 0.5 mM, diluted in ddH_2O from 10 mM stock in vehicle EtOH), and matching volumes of EtOH. The two mixtures were mixed together and placed at 37°C for 30 min and flash frozen. All samples were thawed together on room temperature shaker with the addition of 1.8 μL 100% TFA to precipitate protein. The thawed solution was centrifuged at 20,000g for 5 min at 4°C, and 1.8 μL of 9.56 M NaOH was added to the collected supernatant. The solution was incubated at 37°C for 30 min on shaker with 3.9 μL fresh 7X mM GSH such that final HNE:GSH ratio of ~1:2 based on the HNE concentration. 10 μL of the sample was diluted in 90 μL MeOH and placed on ice until mass spectrometry analysis immediately after.

Mass spectrometry analysis of the product from CYP2A6-assisted HNE(alkyne) turnover

Samples were kept in chilled autosampler at 10°C during analysis. Analysis was performed in negative ion mode on Vion IMS QTOF (Waters) in-line with Acquity UPLC Class I (Waters) Sample Manager, Binary Solvent Manager, and Column Manager, operated under UNIFI software (Waters). 5 μL of each sample was injected onto 40°C heated Acquity Premier BEH 1.7 μm 2.1 x 50 mm C18 Column (Waters, P/N 186009452) at 0.4 μL/min flow rate of 100% Solvent A (0.1% FA) and 0% Solvent B (methanol). Between 0.5 and 3.0 min, Solvent B increases to 100%, and remains until 5.0 min. Between 5.0 and 5.1 min, Solvent B decreases back to 0%, and remains until 6.0 min. The QTOF analyzer was set to sensitivity mode, at 1.4 kV capillary voltage, 120°C and 500°C for source and desolvation temperatures, respectively. Scan range was set between 50-1200 *m/z* at 1 s scan time, lock mass correction every 5 min, and Intelligent Data Capture enabled. MS2 was enabled with collision energy of 4.0 eV at low energy, and between 20.0-40.0 eV for high energy ramping.

Raw data processing was performed in UNIFI via Full Application Processing with the following compounds added for identification: GSH ($C_{10}H_{17}N_3O_6S$, 307.0838 Da), HNA ($C_9H_{16}O_3$, 172.1099 Da), GS-HNE ($C_{19}H_{33}N_3O_8S$, 463.1988 Da), and GS-HNA ($C_{19}H_{33}N_3O_9S$, 479.1938 Da). Molecules were identified based on matching to the *m/z*, the retention time (RT), and the Collision Cross Section (CCS) values of these molecules, determined through a separate experiment with standards. Target identification has an RT tolerance of 0.1 min, CCS tolerance of 3%, and a mass tolerance of 10 ppm. Peak smoothing was performed with mean smoothing algorithm at 2 half width with 2 iterations. Peak integration was performed with automatic peak width and threshold detection, integration at 0.0% liftoff and 0.5% touchdown. The output of this processing generates a Review where the observed *m/z*,

mass error ppm, observed RT, observed CCS in angstroms, response, and adducts information was available. Response values were used as the integrated area value, used for quantification of the amount of GS-HNA and GS-HNE molecules in each sample.

Synthesis of alkyne functionalized DHN and HNA

The synthesis until HNA-methyl ester was described as previously published.[23]

For methyl [(4-chlorophenyl)sulfinyl]acetate (**6**), 3.62 g (25 mmol) starting material **3** was added to 40 mL DMF, then 3.08 g (27.5 mmol) K_2CO_3 was added. After stirring for 0.5 h at rt., 3.83 g (25 mmol) **4** and 0.96 g KI were added to the system. After stirring overnight at rt., brine was added to the reaction. The product was extracted by EtOAc; washed with brine and cold water 4-5 times. The organic layer was dried with sodium sulfate and concentrated in a vacuum.

5.02 g (23 mmol) starting material **5** was added to 20 mL $CHCl_3$, then 5.75 g (25 mmol) mCPBA was added slowly. After stirring overnight, the reaction was quenched by saturated $NaHCO_3$. The product was extracted by CH_2Cl_2 and washed with $NaHCO_3$ 3 times. The organic layer was dried with sodium sulfate and concentrated in a vacuum. The product was purified by flash silica chromatography (80% hexane, 20% EtOAc) and analyzed by ^{1}H-NMR spectroscopy.

For non-2-ene-1,4-diol, 220 mg (1.2 mmol) starting material **7** was dissolved in 20 mL CH_2Cl_2 and cooled to 0 °C, then 4.8 mL DIBAL-H in hexane (1M solution) was added drop by drop. After stirring for 3 hours, the reaction was quenched by adding cold water and saturated Rochelle salt solution, followed by CH_2Cl_2 extraction. The white-solid product was dried and concentrated, purified by flash silica chromatography (70% hexane, 30% EtOAc), and analyzed by ^{1}H-NMR spectroscopy (400 MHz, $CDCl_3$): δ 7.06 (dd, J = 15.6, 4.6 Hz, 1H), 6.08 (dd, J = 15.6, 1.7 Hz, 1H), 4.41 (ddt, J = 6.5, 4.7, 2.4 Hz, 1H), 2.26 (td, J = 6.7, 2.6 Hz, 2H), 1.98 (t, J = 2.6 Hz, 1H), 1.84 – 1.57 (m, 4H).

For 4-hydroxy-2-nonenoic acid, 220 mg (1.2 mmol) starting material **7** was dissolved in 15 mL THF/water at a 1:1 ratio, then 0.48 g LiOH (20 mmol) was added. After stirring for 2 hours, the reaction was washed by ether two times. Subsequently, 2 M HCl was added to the aqueous layer slowly until pH = 2-3. The yellow-oil product was extracted by EtOAc, dried and concentrated, purified by flash silica chromatography (60% hexane, 40% EtOAc), and analyzed by ^{1}H NMR (400 MHz, $CDCl_3$) spectroscopy: δ 5.84 (dt, J = 15.6, 5.1 Hz, 1H), 5.75 (m, 1H), 4.15 (t, J = 5.2 Hz, 3H), 2.22 (tt, J = 4.3, 2.5 Hz, 2H), 2.06 (s, 2H), 1.96 (t, J = 2.7 Hz, 1H), 1.70 – 1.53 (m, 4H).

QUANTIFICATION AND STATISTICAL ANALYSIS

The quantification methods were explained in the corresponding methods. Samples generated from the same pool of animals (e.g., 6 x 100 mm plates, depending on specific experiments) were considered one biological replicate. Data analysis and statistical treatments are detailed in corresponding figure legends. *P* values were calculated either from t-test or adjusted comparisons in ANOVA, explained in the decision tree for the t-test or ANOVA test (Methods S3). Data were plotted/fit and statistics were generated using GraphPad Prism. Bonferroni correction was applied where applicable and indicated, typically when multiple comparisons elevate the chance of Type 1 errors. When images are shown, they are representative of multiple independent samples. For experiments involving cultured cells, samples generated from individual wells or plates were considered biological replicates. For *C. elegans* experiments, designation of how biological replicates were considered is described in figure legends. In the figure legend for each experiment, how the data are presented in the figure (typically mean ± SEM) is clearly indicated.

CellPress
OPEN ACCESS

Supplemental figures

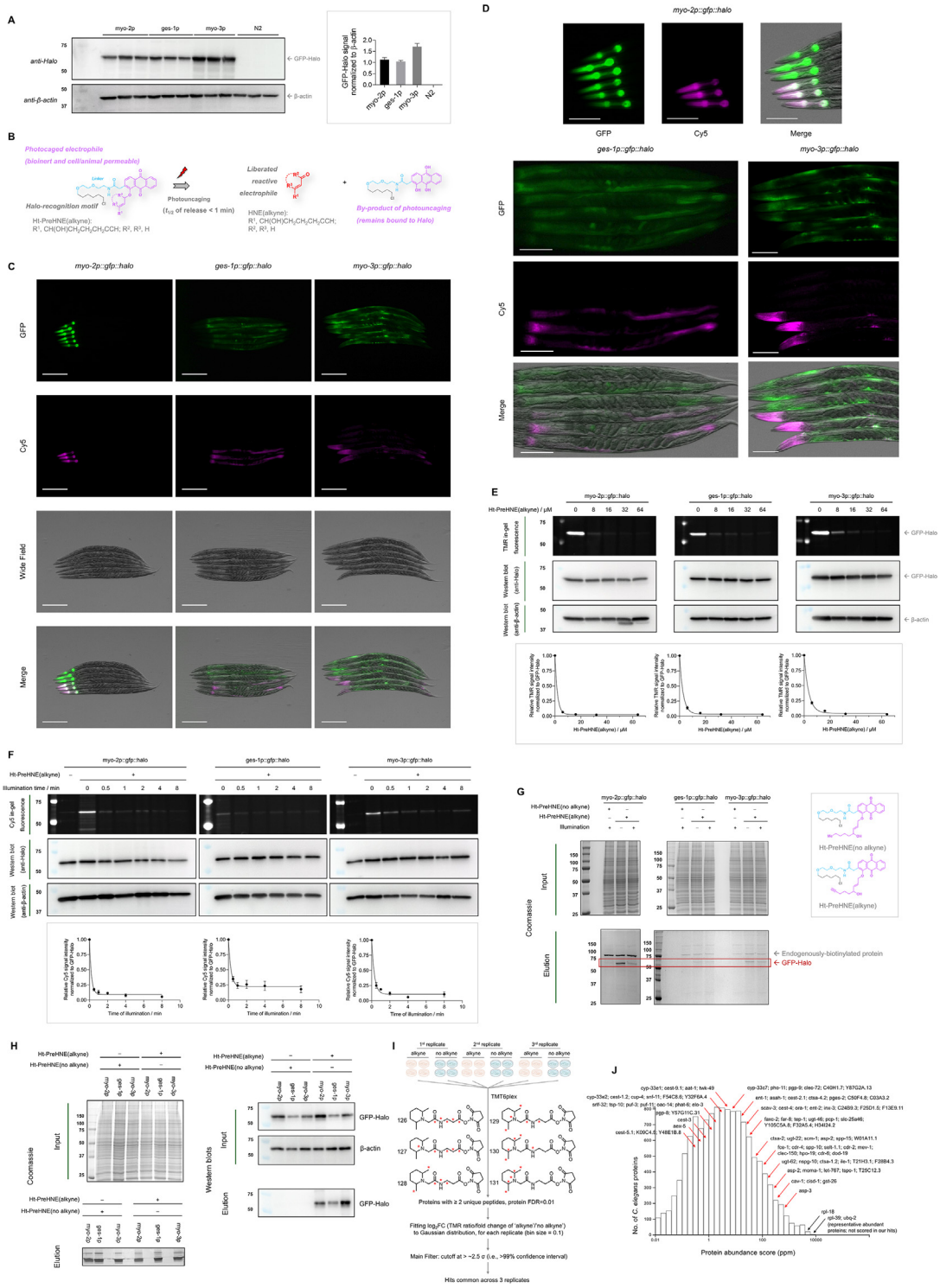

(legend on next page)

Figure S1. OS-Localis-REX development, validations, and results, related to Figure 1

(A) Assessments of transgene expression. Expression level of GFP-Halo transgene product in three organ-specific transgenic strains. 20 healthy L4-young adult transgenic *C. elegans* were selected and grown on nematode growth medium (NGM-agarose) plates (10 cm in diameter) for 4–5 days at 20°C. Worms were then lysed and normalized lysates were subjected to western blot analysis using anti-Halo antibody. Representative data shown from $n = 3$ independent biological replicates. Samples from Bristol N2 wild-type strain were used for comparison. Inset: quantification (by ImageJ) where GFP-halo signals were normalized against β-actin loading control. See also Figure 1A. $n = 3$ for all conditions.

(B) Schematic of chemistry underlying precision localized electrophile delivery platform, used to identify electrophile-actionable protein targets in specific organs of live *C. elegans*. See also Figure 1B.

(C) Immunofluorescence and click-imaging validate the organ-specific anchorage of photocaged-electrophile probe (Ht-PreHNE[alkyne]) binding. Myo-2, ges-1, and myo-3 promoters respectively drive GFP-Halo expression in pharynx, intestine, and body-wall muscles expression, enabling the organ-specific photocaged-electrophile probe anchoring. Each image shows 3 respective age-synchronized organ-specific GFP-Halo-expressing hermaphrodites at day 1 adult stage with Ht-PreHNE(alkyne) treatment (3 lower worms), against 3 age-matched worms with Ht-PreHNE(no-alkyne) treatment (3 upper worms). Scale bars: 200 μm. Note: these animals are mosaic, and hence GFP expression patterns are not identical across all GFP-Halo-transgenic worms in the same group. See also Methods S1.

(D) Zoomed images of (C). Scale bars: 100 μm. Note: these animals are mosaic, and hence GFP expression patterns are not identical across all GFP-Halo-transgenic worms in the same group.

(E) Assessments of minimum probe concentration to saturate Halo. Minimum Ht-PreHNE(alkyne) probe concentration required for saturating GFP-Halo active site in live *C. elegans* determined by TMR-Halo-ligand-blocking analysis. Ht-PreHNE(alkyne)-treated (6 h) or corresponding DMSO-treated live worms were subjected to lysis, followed by treatment of resulting lysate with TMR-Halo ligand (10 μM, 30 min), which labeled the Halo not bound by Ht-PreHNE(alkyne) in worms. Representative data are shown from $n = 3$ independent biological replicates. Inset: quantification (by ImageJ) of dose-dependent blockage of TMR-Halo-ligand binding, normalized against western blot signals for total GFP-Halo and β-actin loading control. $EC_{50}^{[\text{Ht-PreHNE(alkyne) for saturating GFP-Halo } \textit{in vivo}]} = 1.3 \pm 0.2$ μM for *myo-2p::gfp::halo* strain; 1.9 ± 0.3 μM for *ges-1p::gfp::halo* strain; 2.5 ± 0.3 μM for *myo-3p::gfp::halo* strain. $n = 3$ for all conditions.

(F) Assessments of photouncaging efficiency. Time-dependent photo-uncaging of Ht-PreHNE(alkyne) in live *C. elegans*. Ht-PreHNE(alkyne)-treated (12 μM, 6 h) live worms were subjected to a low-power hand-held lamp (366 nm, 5 mW/cm^2) for indicated time. Representative data are shown from $n = 3$ independent biological replicates. Inset: quantification (by ImageJ) of time-dependent liberation of HNE(alkyne) from Halo, reported by Cy5-signal depletion, normalized against GFP-Halo signal. Data were fit to exponential curve: $t_{1/2}$ (photo-uncaging *in vivo*) = 0.2 ± 0.1 min for *myo-2p::gfp::halo* strain; 0.2 ± 0.1 min for *ges-1p::gfp::halo* strain; 0.2 ± 0.1 min for *myo-3p::gfp::halo* strain. $n = 3$ for all conditions.

(G) OS-Localis-REX validation of selective enrichment of electrophile-responder proteins from indicated organ-specific Halo-transgenic strains. Representative Coomassie-stained input and elution gels following biotin-streptavidin enrichment of electrophile(alkyne)-tagged proteins (and photocage-bound GFP-Halo) from *myo2p::gfp::halo, ges1p::gfp::halo*, and *myo3p::gfp::halo* strains. Selective enrichment was observed in samples treated with both Ht-PreHNE(alkyne) and light illumination, against two respective controls, namely, Ht-PreHNE(no alkyne) and light illumination; Ht-PreHNE(alkyne) alone treatment. Inset: corresponding photocaged-probe structures. The signal of GFP-Halo band (~60 kDa) decreased in samples treated with Ht-PreHNE(alkyne) and light illumination, as expected, as a result of photouncaging, leaving less amount of alkyne-functionalized photocaged-probe covalently bound to Halo. ~75 kDa band likely represents an endogenously biotinylated protein, serving as an internal control.

(H) Validation of enrichment workflow for TMT6-plex target ID of organ-specific electrophile responders by OS-Localis-REX. Left: representative Coomassie-stained input (top) and elution (bottom) gels for organ-specific TMT6-plex mass spectrometry analysis from indicated Halo-transgenic strains. TMT6-plex per each strain constituted 2 sets of conditions and 3 independent biological replicates, namely: Ht-PreHNE(no alkyne) and light treatment (triplicate control set); and Ht-PreHNE(alkyne) and light treatment (triplicate experimental set) (see also Figure 1B). Elution gel allows desalting prior to in-gel trypsin digest and TMT labeling. The thick bands in elution gel were streptavidin from high-capacity streptavidin agarose. Right: Same as the left one, except that samples were analyzed by western blot using anti-GFP and anti-β-actin antibodies. β-actin was used as the loading control. As expected, control groups did not enrich (no-alkyne)probe-bound-GFP-Halo.

(I) Selection criteria for quantitative ranking of organ-specific electrophile responders by OS-Localis-REX. TMT6-plex labeling and filtering workflow for organ-specific electrophile-responder target ID. See Figure 1B for preceding experimental details performed in live *C. elegans*. Alkyne and no-alkyne designate corresponding photocaged-probes used (see inset). For each replicate, hits (representing proteins with ≥2 unique peptides, protein FDR = 0.01) were first ranked by TMT-ratiometric analysis against no-alkyne-probe-treated controls, and these enrichment ratios (specifically, $\log_2$FC) were fit to Gaussian distribution analysis. Hits with >2.58 σ (corresponding to >99% confidence interval) from the mean, were combined from all 3 replicates per strain, and the resultant hits common to 3 replicates per strain were scored as significant hits. See also Figure 1C, Data S1 and S2, and Methods S1.

(J) Abundance profile of indicated OS-Localis-REX hits. OS-Localis-REX hits (see also Figure 1D and Data S2), mapped against whole-genome protein abundance in *C. elegans* (from PAXdb), reflect a wide-ranging native protein abundance across the electrophile-responders identified.

All data present mean ± SEM.

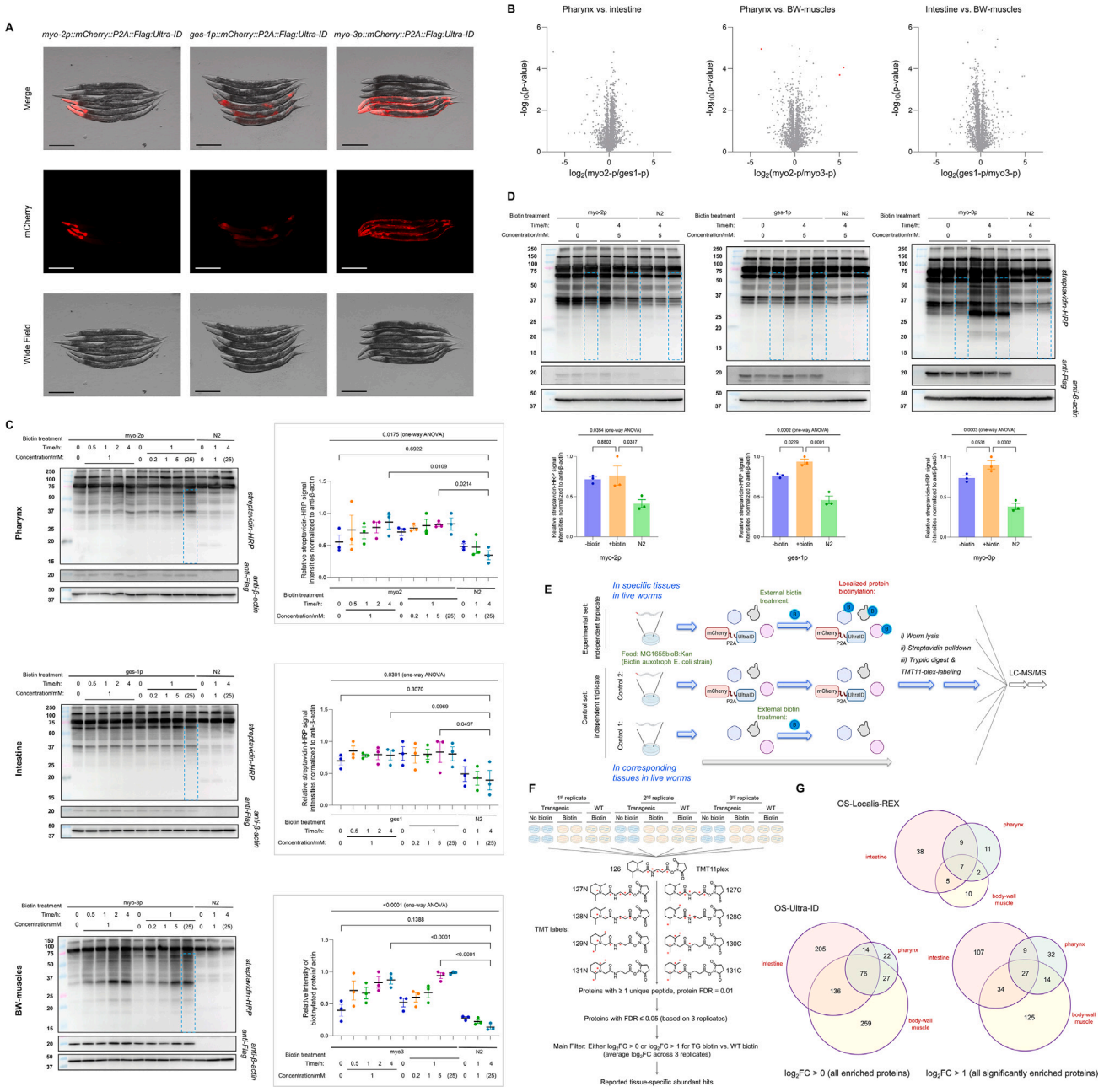

Figure S2. OS-Ultra-ID establishment, validations, and results, related to Figure 2

(A) Expression, morphological, and viability validations of OS-Ultra-ID strains by live imaging. Fluorescence imaging, post levamisole immobilization of live worms, confirms organ-specific mCherry-P2A-Ultra-ID expression: *myo-2*, *ges-1*, and *myo-3* promoters respectively drive mCherry-P2A-FLAG-Ultra-ID expression in pharynx, intestine, and body-wall muscles. Each image shows 3 respective age-synchronized organ-specific mCherry-P2A-FLAG-Ultra-ID-expressing hermaphrodites at day 1 adult stage (lower) against 3 age-matched wild-type N2 hermaphrodite worms (upper). Scale bars: 200 μm. Note: these animals are mosaic, and hence mCherry expression patterns are not identical across all 3 transgenic worms in the same group. The images within the first column here are reproduced in Figure 2A. See also Methods S1.

(B) Total proteome abundance remains largely the same across the three OS-Ultra-ID strains. Lysates derived from each strain were subjected to label-free quantification (LFQ) MS-based target ID. See STAR Methods for details. (a–c) The resulting volcano plots show pair-wise comparison across the 3 strains. Only 3 proteins were found to be statistically significantly different (FDR threshold = 0.05, $s_0 = 1$ for t test = variance between groups/(variance within groups + s_0), blue curves), and this was observed for comparison between pharynx (myo-2p)- and BW muscles (myo-3p)-specific Ultra-ID strains (middle). Ept-1 expression level was downregulated, and those of klp-15 and D1086.10 were upregulated, in pharynx-expressing strain, with respect to BW muscles-expressing strain (see 3 red dots in the middle plot). See also Data S4.

(legend continued on next page)

(C) Optimizations of Ultra-ID enzymatic activity in newly generated OS-Ultra-ID strains. Streptavidin blot analyses of lysates originating from indicated strains, following treatment with indicated dosage of biotin over indicated time periods. The worms in these experiments were fed with MG1655:BioBKan (biotin-auxotrophic *E. coli*). The Bristol N2 (wild type) shows the endogenously biotinylated proteome background, to a lower extent than that in transgenic worms expressing active Ultra-ID in the absence of exogenous biotin treatment. Inset on the right: in each case shows quantification of signals below 60 kDa MW marker within the corresponding blot (region marked by a representative dotted blue rectangle), normalized by anti-β-actin loading control. Note: complete solubility was not achievable at "(25)" mM biotin. Thus, 5 mM was considered the highest dosage in accurately reporting the dose-responsive biotinylation activity data. *p* values were calculated by Dunnett's multiple comparisons test, post one-way ANOVA. $n = 3$ for all conditions.

(D) Validations of OS-Ultra-ID transgenic strains and enrichment workflow for TMT11-plex target ID of organ-specific high-abundant proteins. Biotinylated proteins were increased in indicated Ultra-ID transgenic (Tg) strains upon treatment with 5 mM of biotin for 4 h. See STAR Methods for details. Worms were lysed, and lysates were analyzed by streptavidin blots. The N2 (wild type) strain treated with biotin and the respective Tg strains without exogenous biotin treatment were included as controls. Due to the endogenous biotinylation in these animals (see main text discussions) and the high endogenous activity of Ultra-ID, the signals in Tg strains (without biotin treatment) were higher than wild-type animals, despite the fact that all animals were fed with biotin-auxotrophic *E. coli*. The bands in N2 lanes represent endogenous biotinylated proteins in wild-type *C. elegans*. Quantified data for signals below 60 kDa MW marker (see dotted blue rectangle) of blots were normalized by anti-β-actin loading control. These observations guided us to choose biotin-treated N2 as more relevant controls for TMT-ratio calculations. See discussions in main text and also Data S3 and S5. $n = 3$ for all conditions.

(E) Workflow illustrating organ-specific proximity mapping (OS-Ultra-ID) in live *C. elegans*, quantitative mapping of organ-specific protein abundance. Animals were cultured from MG1655bioB:Kan (biotin auxotroph *E. coli* strain). Live animals of selected strain were treated with either external biotin (top row, experimental set comprising independent biological triplicates) or buffer alone (middle row, "control 2," comprising independent biological triplicates). Bristol N2 worms were treated with identical time and concentration of external biotin for control set 1 (bottom row, "control 1," comprising independent biological triplicates). Following washout, the animals were lysed, and biotinylated proteins were enriched by streptavidin pull-down as described in STAR Methods. Subsequent to trypsin digest, the digested peptides were labeled isotopically by TMT11-plex reagents prior to LC-MS/MS analysis. See also (D).

(F) Setup and selection criteria for quantitative ranking of organ-specific high-abundant proteins by OS-Ultra-ID. TMT11-plex (only 9 types of TMT tags were used in this experiment due to 9 different groups: see discussion for details) was deployed. For each replicate, hits (representing proteins with ≥ 1 unique peptide, protein discover FDR = 0.01) were first selected by setting an FDR ≤ 0.05. Afterward, based on the TMT quantitative ratiometric analysis against the data resulting from wild-type (N2) biotin-treated strains as controls, either $\log_2FC > 0$ (all enriched proteins) or $\log_2FC > 1$ (2-fold significantly enriched protein) were further selected. See also Figures 2A–2C and Data S3 and S5.

(G) Unique and common hits mapped by OS-Localis-REX and OS-Ultra-ID across 3 organs. See Figure S1I for selection criteria of OS-Localis-REX and (F) of OS-Ultra-ID. For OS-Localis-REX (Top), briefly, 11, 38, and 10 proteins were regarded as organ-unique and statistically significant electrophile-responders derived from indicated organ-specific GFP-Halo-transgenic strains; and 9, 5, and 2 proteins appear in two strains; and 7 proteins are electrophile-responders commonly responsive in all three strains. See also Data S1 and S2. Bottom left: based on $\log_2FC > 0$ (all enriched proteins) threshold and other criteria as defined in (F), 22, 205, and 259 proteins are unique organ-specific high-abundant proteins derived from corresponding OS-Ultra-ID strains; and 14, 136, 27 targets appear in two strains; and 76 proteins are high-abundant proteins common to all three strains. Bottom right: based on $\log_2FC > 1$ (all significantly enriched proteins) threshold and other criteria as defined in (F), 32, 107, and 125 proteins are unique organ-specific high-abundant proteins derived from corresponding OS-Ultra-ID strains; and 9, 34, and 14 targets appear in two strains; and 27 proteins are high-abundant proteins common to all three strains. See also Data S5.

All data present mean ± SEM.

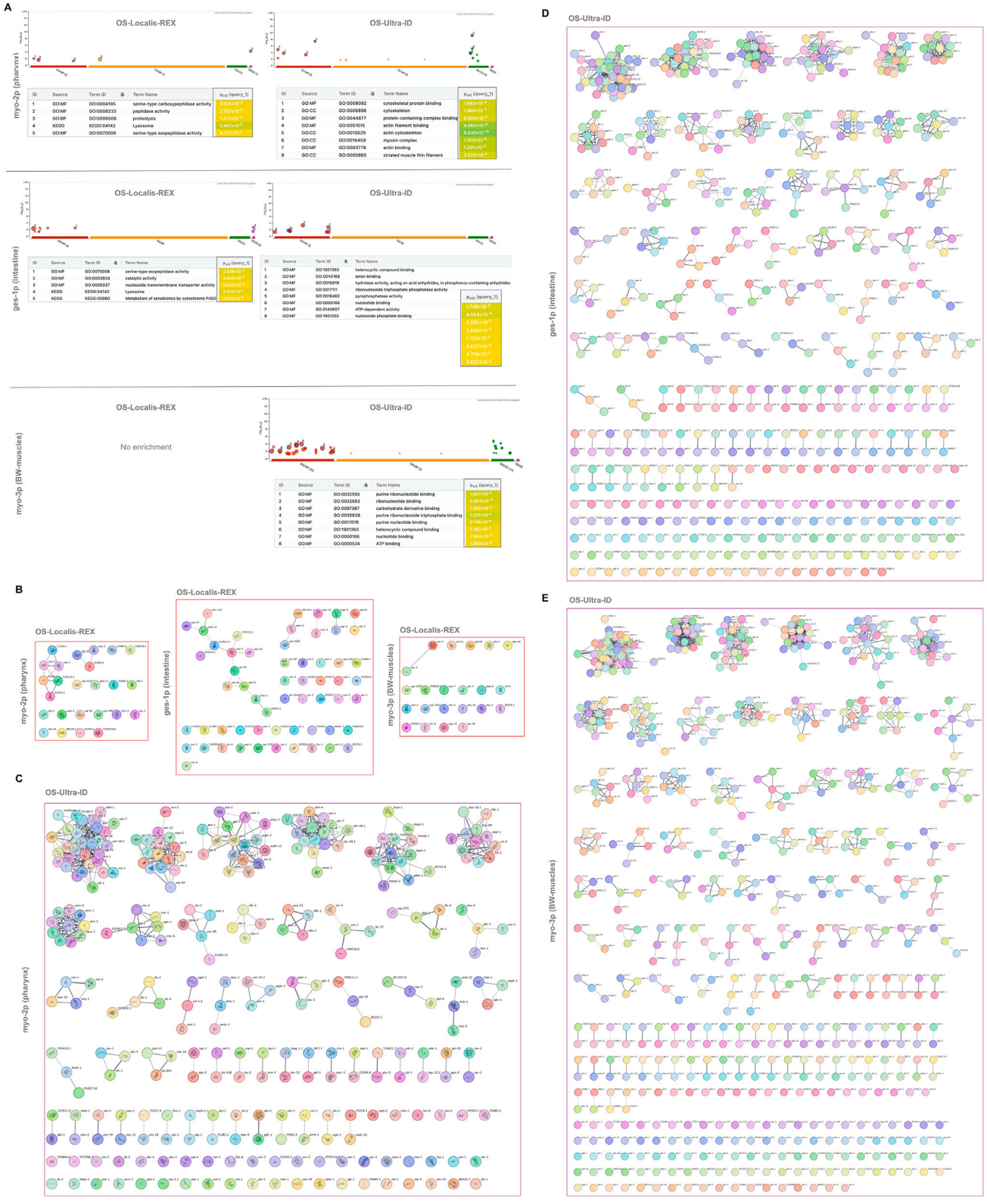

(legend on next page)

Figure S3. Bioinformatic analyses of ranked hits from OS-Localis-REX and OS-Ultra-ID, related to Figures 1 and 2

(A) Functional enrichment analysis of ranked hits from OS-Localis-REX and OS-Ultra-ID, using g:*Profiler*. OS-Localis-REX hits shown in Data S2 were subjected to online software *g:Profiler*, using manufacturer's protocols[80] (https://bio.tools/gprofiler). A similar analysis was performed for OS-Ultra-ID datasets (Data S5A–S5C) by inputting the respective ranked protein list from each organ including all hits with fold-enrichment greater than 2. Insets in each correspond to output showing p_{adj} in the order of table entries. The resulting Manhattan plots from the enrichment analysis results were set to display: GO subterms (MF, molecular function; CC, cellular component; BP, biological process); and KEGG biological pathways. OS-Localis-REX hits derived from BW-muscle-specific Halo-transgenic strain have no functional enrichment. See, URL below for general interpretations of the Manhattan plots, and main text for discussions. https://biit.cs.ut.ee/gprofiler/page/docs.

(B–E) Network clustering and functional enrichment of ranked hits from OS-Localis-REX and OS-Ultra-ID, using STRING analysis. OS-Localis-REX hits (in B) shown in Data S2 and OS-Ultra-ID hits (C–E, corresponding to Data S5A–S5C: those manifesting fold-enrichment greater than 2), were subjected to STRING analysis followed by MCL clustering, following manufacturer's protocols.[83] Default cutoff thresholds in Cytoscape (v3.10.1) were deployed following https://jensenlab.org/training/stringapp/ (exercise:3). For clarity, GO terms and KEGG pathways outputs are omitted within this figure, but terms identical to those shown in (A) were obtained as anticipated, and no overlapping terms were observed between hits from OS-Localis-REX and those from OS-Ultra-ID. As in (A), OS-Localis-REX hits derived from BW-muscle-specific Halo-transgenic strain have no functional enrichment. See main text for discussions.

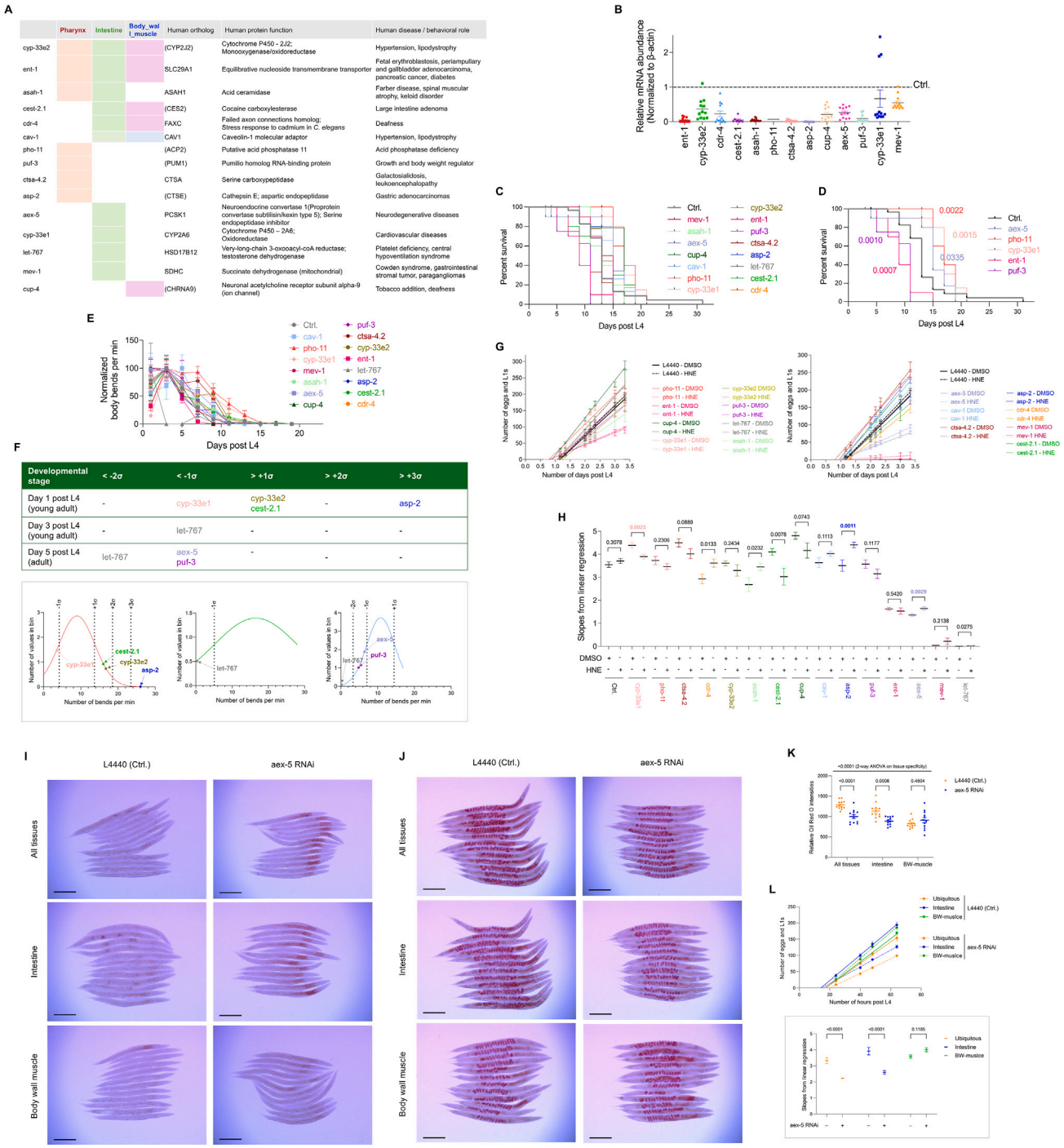

Figure S4. Investigations into functional relevance of selected OS-Localis-REX hits, related to Figure 3

(A) Seleted indicated OS-Localis-REX hits. 15 selected hits assayed for functional relevance in this study, and their human orthologs and associated functions. Human orthologs in parentheses were identified using BLAST search. Others were established orthologs annotated in WormBase. See also Data S2.

(B) RNAi knockdown in *C. elegans* validated by RT-qPCR. RNAi procedure and RT-qPCR analysis were performed as described in STAR Methods. Relative mRNA abundance was normalized to β-actin. Horizontal dotted line indicates knockdown control (Ctrl), the value of which was arbitrarily set to 1.0. See Methods S1 for primer sequences. n = 12 for all conditions, including 3 biological replicates and 4 technical replicates.

(C and D) Effect of RNAi knockdown of individual hit proteins on animal survival. The viability assay and RNAi were performed as described in STAR Methods. The resultant data comparing each trace from RNAi of each of the 15 genes, against knockdown control (Ctrl.) (in C), were subjected to log-rank (Mantel-Cox) (Figure 3A) and Gehan-Breslow-Wilcoxon (in D) tests, respectively, uncovering in 4 and 5 targets, that have an effect on survival, as described in Figure 3A. See also illustrative chart in Figure 2E. n = 30 for the control group. n = 10 for other groups.

(legend continued on next page)

(E) Effect of RNAi knockdown of individual hit proteins on animal motility. The assay assessing the number of body bends made by worms subjected to indicated RNAi targeting 15 individual genes, or knockdown control (Ctrl.), was performed as described in STAR Methods. See also illustrative chart in Figure 2E. Data across all 15 genes (and Ctrl.) were normalized such that the highest body-bending rate corresponds to 100 in each case. Figure 3B selectively shows data corresponding to the 7 genes (out of these 15 shown in this supplemental figure) whose RNAi resulted in statistically significant perturbations in motility, based on Gaussian distribution analysis (see F). n = 30 for the control group. n = 10 for other groups.

(F) Gaussian distribution analysis of measured non-normalized body-bending rate results in the shown list of outstanding genes with indicated standard deviations, from the mean body-bending rate, against indicated developmental stage. Inset below shows Gaussian plots for non-normalized body-bending rate at, left: day 1 post L4. Middle: day 3 post L4, and right: day 5 post L4. Genes exhibiting $>1\sigma$ or $<-1\sigma$ were indicated in each plot.

(G) Effect of RNAi knockdown of individual hit proteins in HNE-treated vs. untreated animals on the efficiency of fertile eggs laid. Linear regression analysis of the number of fertile eggs over indicated days. Figure 3B selectively shows data corresponding to the 3 genes (out of these 15 shown in this supplemental figure) whose RNAi resulted in statistically significant effects on egg-laying rate as a function of electrophile treatment. n = 48 for the control group. n = 12 for other groups.

(H) Slope values from linear regression in (G). p values are derived from unpaired, two-tailed Students' t test—error is standard error from linear fitting. See also illustrative chart in Figure 2E. The egg-laying assays in worms treated with RNAi of individual 15 genes, in the presence and absence of HNE, were performed as described in STAR Methods. n = 48 for the control group. n = 12 for other groups.

(I) Images of the oil red O-stained L4 *C. elegans* subjected to aex-5 RNAi against RNAi control. 12 fixed age-synchronized L4 worms were oil red O stained and manually aligned in each image. Aberrant accumulation of lipids in the anterior intestine was observed only in the intestinal- or ubiquitous-aex-5-RNAi-treated groups, with respect to the corresponding RNAi-control groups. Scale bars: 200 μm.

(J) Images of the oil red O-stained adult *C. elegans* subjected to aex-5 RNAi against RNAi control. 12 fixed age-synchronized adult hermaphrodites were oil red O stained and manually aligned in each image. In the intestinal- and ubiquitous-aex-5-RNAi-treated worms, the lipid level was decreased, and the worm sizes were smaller than control worms. Scale bars: 200 μm.

(K) The oil red O signals were quantified by circling the entire animal except for the pharyngeal region of adult worms (in J). p values were calculated by Šídák's multiple comparisons test in two-way ANOVA. n = 12 for all conditions.

(L) Egg-laying rate of *C. elegans* altered in response to specific organ of aex-5 RNAi. Time-dependent rise in the total number of eggs in indicated groups subjected to three types of organ-specific or ubiquitous RNAi, against RNAi control (L4440). n = 11 for the ubiquitous RNAi, DMSO group. n = 12 for other groups. Inset: egg-laying rate of corresponding groups. In ubiquitous-RNAi and intestinal-RNAi groups, worms showed decreased egg-laying rates with respect to the corresponding RNAi-control groups.

All data present mean ± SEM.

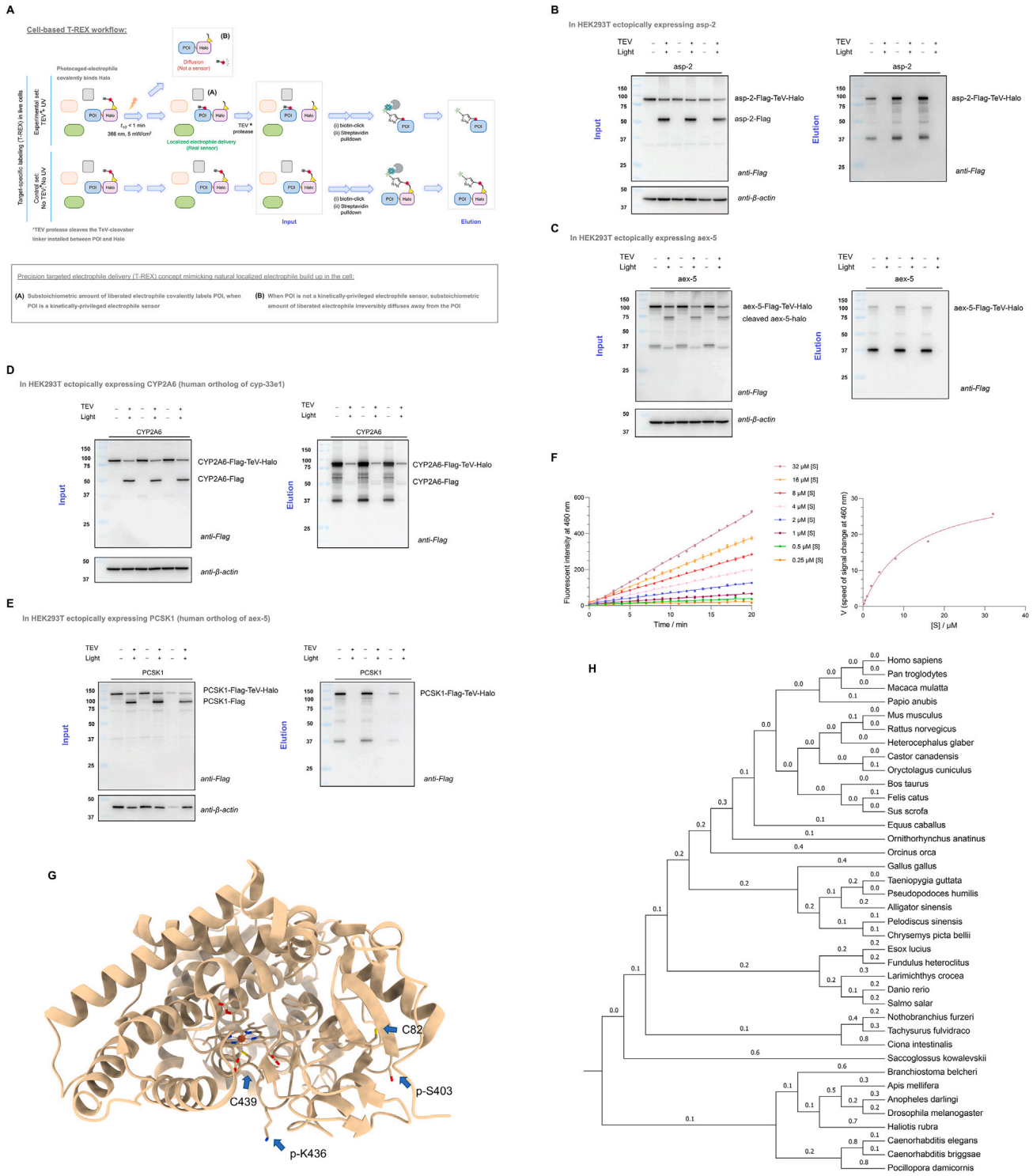

Figure S5. Validations of Cyp-33e1 and its human orthologs CYP2A6 as kinetically privileged responders of HNE using live cell-based and recombinant protein-based investigations, related to Figure 4

(A) Workflow of target-specific electrophile labeling (T-REX) for validating the kinetically privileged-electrophile-sensing ability of cyp-33e1 and its human ortholog, CYP2A6, in live HEK293T cells. Cultured HEK293T cells ectopically expressing corresponding Halo-fused protein-of-interest (POI) constructs as indicated in (B)–(E) and Figures 4A, S6A, and S6B) were subjected to T-REX precision localized electrophile delivery (against samples not exposed to light, i.e., no

(legend continued on next page)

electrophile release, as negative controls), followed by cell lysis, TeV-protease treatment (where applicable as indicated in (B)–(E) and Figures 4A, S6A, and S6B) that separates Halo and POI, and Click-biotin pull-down (see an overview workflow shown and also STAR Methods for details).

(B and C) Cyp-33e1 (but not asp-2 and aex-5) is a privileged electrophile sensor in live HEK293T cells. Following cell-based T-REX procedure and click-biotin pull-down workflow (A), input and elution samples were analyzed by western blot using anti-FLAG antibody. Anti-β-actin antibody was used as loading control of the input samples. Each blot shows data from 3 independent biological replicates. See also Figure 4A. Predicted molecular weights of protein of interest (POI) and relevant constructs (MWs): POI-FLAG-TeV-Halo-His: 84 kDa (asp-2); 96 kDa (aex-5); and POI-FLAG (post TeV-protease cleavage): 49 kDa (asp-2); 61 kDa (aex-5). Note: incomplete TeV cleavage results in residual full-length fusion protein in + TeV lanes where applicable. Inadvertent cleavage occurs during the course of pull-down, leading to multiple FLAG-positive bands in negative-control samples in elution blot. Nonetheless, no HNE(alkyne)-tagged enriched species in experimental samples (+ TeV, + light) in elution blot was observed. These data in combination with corresponding results from cyp-33e1 (Figure 4A), CYP2A6 (human ortholog of cyp-33e1, D), and PCSK1 (E), and *in vitro* HNEylation of CYP2A6 (Figure 4B), collectively validate kinetically privileged electrophile-sensing propensity of cyp-33e1/CYP2A6, over other POIs assessed under identical assay conditions. See also Figures 5A, 5B, S6A, and S6B and Data S3.

(D and E) CYP2A6 (but not PCSK1), human ortholog of cyp-33e1, is a privileged electrophile sensor in live HEK293T cells. The experimental setup and data interpretations identical to those described above in (B) and (C) legend were deployed, except that POI corresponds to CYP2A6 or PCSK1. PCSK1 is the human ortholog of aex-5. Predicted molecular weights (MWs): POI-FLAG-TeV-Halo-His: 94 kDa (CYP2A6); 121 kDa (PCSK1); and POI-FLAG (post TeV-protease cleavage): 59 kDa (CYP2A6); 86 kDa (PCSK1). Note: incomplete TeV cleavage results in residual full-length fusion protein in + TeV lanes where applicable. Inadvertent cleavage occurs during the course of pull-down, leading to multiple FLAG-positive bands in negative-control samples in elution blot. Nonetheless, the HNE(alkyne)-tagged enriched species in experimental samples (+ TeV, + light) in elution blot in (D) corresponds to MW of CYP2A6-FLAG. In (E) with PCSK1, no HNE(alkyne)-tagged enriched species in experimental samples (+ TeV, + light) was observed in elution blot. These data in combination with corresponding results from cyp-33e1 (Figure 3A), asp-2, and aex-5 (B and C), and *in vitro* HNEylation of CYP2A6 (Figure 3B), collectively validate kinetically privileged electrophile-sensing propensity of cyp-33e1/CYP2A6, over other POIs assessed under identical assay conditions. See also Figures 5A, 5B, S6A, and S6B and Data S3.

(F) Determination of K_m of substrate, 3-cyano coumarin, for CYP2A6, human ortholog of cyp-33e1. Derivation of K_m of the substrate, 3-cyano coumarin (see STAR Methods for details). Left: progress curves of the CYP2A6-catalyzed fluorescent-product formation, as a function of indicated substrate concentrations. Right: the slopes from the progress-curve plot fit to linear regression, to yield enzymatic reaction velocities, that were subsequently plotted against substrate concentrations. Subsequent fit of the data to Michaelis-Menten equation $v = V_{max}*[S]/(K_M + [S])$ indicates K_M 12 ± 6 μM; V_{max} 34 ± 7 a.u. s^{-1}. See also Figures 4C, 5C, 5D, S6D, and S6E. $n = 3$ for all conditions.

(G) Ribbon representation of human CYP2A6 (PDB: 1Z10) featuring previously reported canonical enzyme-mediated PTM sites and the two electrophile-sensing cysteines discovered in this study. See also Figure 4D. PhosphoSite+ database maps 9 different enzymatic PTMs (albeit noting that these were identified from large-scale proteomics datasets, with limited or no biochemical validations): phosphorylation at Ser4, Thr16, and Ser22 (the 3 residues not visible in crystal structure); Thr163, Thr295, and Ser403; dimethylation at Arg148 and Arg161; and acetylation at Lys436. 3D structural analysis shows Ser403 and Lys436 (shown in the figure) to be spatially proximal to the two newly identified electrophile-sensing sites, C82 and C439, respectively.

(H) Phylogenetic analysis of cyp-33e1 and cysteine sites. Briefly, 38 representative metazoan species were first selected. All possible Cyp-orthologs in each species were analyzed with respect to sequences of cyp-33e1 and CYP2A6, using the NCBI BLASTp tool. The representative isoforms were selected based on the following parameters: E value, query cover, and positive amino acid, in the BLAST output, to build the maximum likelihood tree[82,87] across different species based on the sequence alignment results. Note: sequence alignments of representative 38 isoforms, one from each species, were performed using MUSCLE.[61] Numbers reflect the distance between branches. See also Figure 4D.

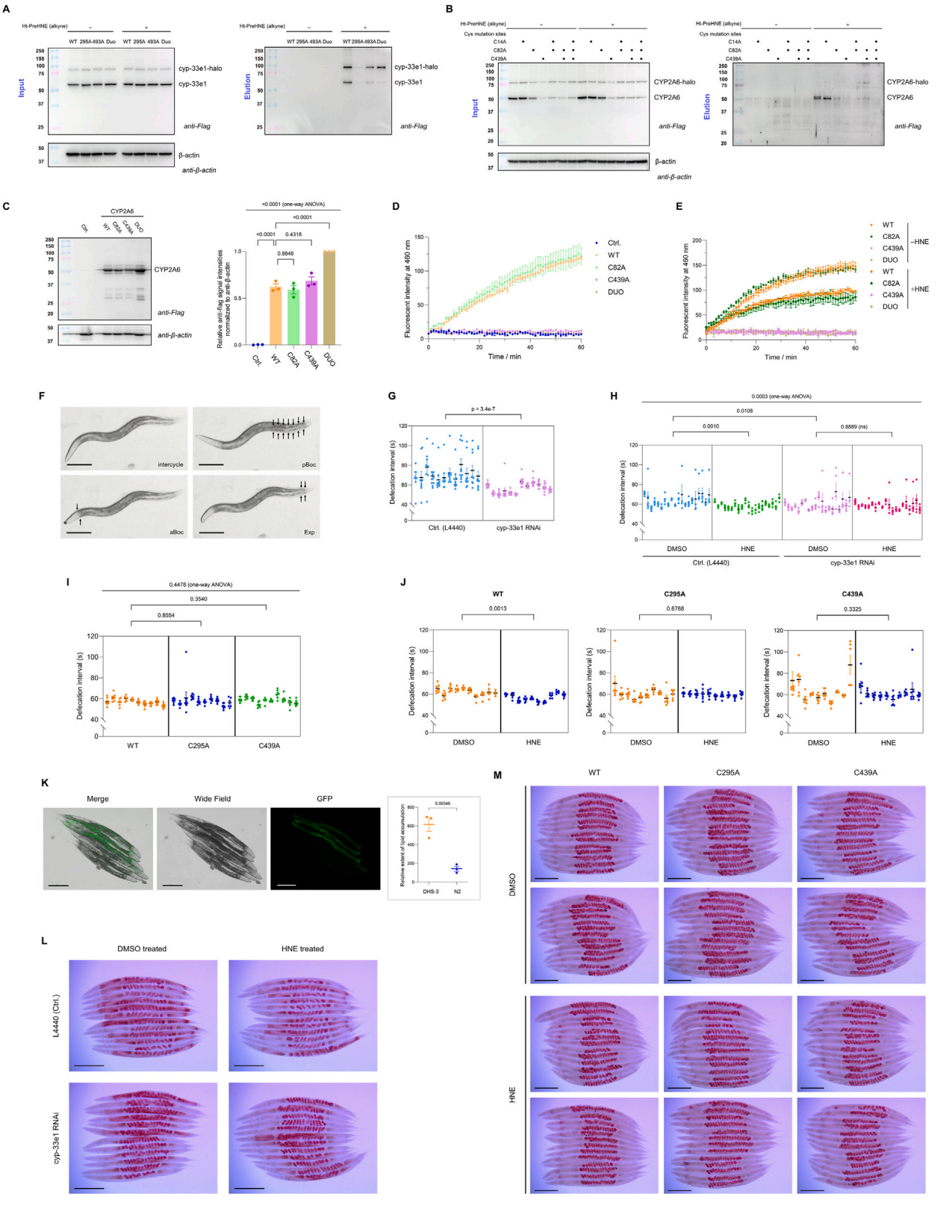

(legend on next page)

Figure S6. Cyp-33e1 and CYP2A6 sense HNE at two cysteines, but the regulation of intestinal physiology is catalytic cysteine (C439) dependent, related to Figures 5 and 6

(A) Cell-based T-REX identifies kinetically privileged electrophile-sensing sites within cyp-33e1. T-REX-assisted evaluation of electrophile-sensing ability of protein of interest (POI): cyp-33e1 WT; single; or double ("duo") cysteine-to-alanine mutants as indicated, were assayed in HEK293T cells ectopically expressing the corresponding Halo-FLAG-(TeV)-POI constructs. Briefly, HNE(alkyne) is transiently made available in substoichiometric amounts within the proximity of indicated Halo-FLAG-(TeV)-POI in live cells following established cell-based T-REX workflow, against indicated controls. Input and elution samples resulting from Click-biotin pull-down of the protein, post lysis of cells subjected to T-REX (vs. indicated control), and subsequent TeV-protease-mediated separation of Halo and cyp-33e1 (WT or mutant), analyzed by western blot using anti-FLAG and anti-β-actin antibodies. For a generic cell-based T-REX workflow, see Figure S5A. Predicted molecular weights (MWs): cyp-33e1-FLAG-TeV-Halo-His: 95 kDa and cyp-33e1-FLAG (post TeV-protease cleavage): 60 kDa. Note: incomplete TeV cleavage resulted in residual full-length fusion protein in all lanes in both input and elution blots. See Figure 5A for corresponding quantification.

(B) Cell-based T-REX identifies kinetically privileged electrophile-sensing sites within CYP2A6. Experiment as in (A), except that CYP2A6 and its indicated mutants replaced cyp-33e1 variants. See Figure 5B for corresponding quantification. Predicted molecular weights (MWs): CYP2A6-FLAG-TeV-Halo-His: 94 kDa and CYP2A6-FLAG (post TeV-protease cleavage): 59 kDa. Note: incomplete TeV cleavage resulted in residual full-length fusion protein in all lanes in both input and elution blots. The quantified data (see Figure 5B) took into account differences in expression levels across WT and mutants.

(C) Western blot analysis and quantification of CYP2A6 (WT and indicated mutants) ectopically overexpressed in HEK293+Hycell expression system. Note: quantified data in (D) and (E) and Figures 5C and 5D, were adjusted for expression-level variations as analyzed by western blot.

(D) Oxidoreductase activity tests and progress curve analyses of CYP2A6 (WT and mutants). Product formation (7-hydroxylation of 4-cyanocumarin) catalyzed by partially purified microsomal CYP2A6 WT and indicated mutants against negative control was measured as described in STAR Methods. See also (C) and Figure 5C. $n = 3$ for all conditions.

(E) Oxidoreductase activity tests and progress curve analyses of CYP2A6 (WT and mutants) in the presence and absence of HNE. Progress curve analyses of partially purified human microsomal CYP2A6 (WT and indicated mutants) following treatment or no treatment with HNE (400 μM, 20 min pre-incubation) were undertaken as described in STAR Methods. See also Figure 5D. $n = 3$ for all conditions.

(F) Representative images of wild-type N2 hermaphrodites undergoing Intercycle (animal at the stage in-between the DMP cycles) and 3 distinct motor steps of the DMP: pBoc, aBoc, and expulsion (Exp). See also Video S1. Briefly, following intercycle, defecation begins with posterior body muscle contraction (pBoc), with ensuing tail compression (furrowing, black arrows in pBoc) (0–8 s). After a short (~1 s) relaxation period, the anterior body muscle contraction (aBoc) occurs (10–11 s), with distinct pharynx movement (black arrows in aBoc), which was immediately followed by enteric muscle contraction (Emc) or expulsion (Exp), whereby the animal's internal pressure expels gut contents via anus opening (black arrows in Exp) (12–13 s). Note: the video was decelerated 0.5×. Scale bars: 200 μm.

(G) Cyp-33e1 regulates defecation motor program (DMP) cycles of *C. elegans*. Measured DMP intervals of age-synchronized control-RNAi (left) or cyp-33e1-RNAi (right) worms at L4 stage (48 h after seeding on RNAi plates). *p* values were calculated by the nested t test. The nested t test was taken because several defecation intervals were recorded from the same worm. Given this linkage between measurements, an unpaired, two-tailed Students' t test is not applicable. See also Videos S2 and S3. $n = 114$ for the L4440 (control) group. $n = 126$ for the cyp-33e1 RNAi group.

(H) Cyp-33e1's electrophile-sensing activity plays a functional role in regulating defecation motor program (DMP) cycles of *C. elegans*. Measured DMP intervals of age-synchronized control-RNAi (left) or cyp-33e1-RNAi (right) worms following 1-h exposure to either electrophile (2 mM HNE in DMSO) or vehicle control (equivalent vol % of DMSO) and 16-h recovery (at day 1 adult stage). *p* values were calculated by Tukey's multiple comparisons test, post nested one-way ANOVA. See also Figure 5G and Videos S4, S5, S6, and S7. DMSO, L4440: $n = 109$; HNE, L4440: $n = 111$; DMSO, cyp-33e1: $n = 110$; HNE, cyp-33e1: $n = 111$.

(I) DMP changes are not ascribable uniquely to loss of cyp-33e1 activity. Measured DMP intervals of wild type (left), C295A knockin (middle), or C439A knockin (right) age-synchronized live worms at L4 stage (48 h after seeding to RNAi plates). *p* values were calculated by Dunnett's multiple comparisons test, post one-way ANOVA. See also Videos S8, S9, and S10. See also Figure 5H. WT: $n = 79$; C295A: $n = 75$; C439A: $n = 69$.

(J) Both electrophile-sensing cysteines within cyp-33e1 are functional regulators of stress-induced changes in *C. elegans* defecation motor program (DMP) cycles. Measured DMP intervals of wild type (left), C295A knockin (middle), or C439A knockin (right) age-synchronized live worms following 1-h exposure to 2 mM HNE(alkyne), or vehicle control (equivalent vol % of DMSO) and subsequent 16-h recovery (at day 1 adult stage). *p* values were calculated by nested t test. See also Videos S11, S12, S13, S14, S15, and S16. See also Figure 5I. DMSO, WT: $n = 63$; HNE, WT: $n = 67$; DMSO, C295A: $n = 65$; HNE, C295A: $n = 65$; DMSO, C439A: $n = 66$; HNE, C439A: $n = 67$.

(K) Lipid-droplet reporter *dhs-3p::dhs-3::gfp* strain manifests a strong GFP signal against background autofluorescence in age-matched wild-type N2 animals. Representative images of 3 age-synchronized *dhs-3p::dhs-3::gfp* hermaphrodites at day 1 adult stage (top) and age-matched wild-type N2 worms (bottom), subsequent to levamisole immobilization. Scale bars: 200 μm. Inset: quantification. The GFP signal was quantified by circling the intestinal region in both groups. *p* values were calculated by unpaired, two-tailed Students' t test. $n = 3$ for all conditions.

(L) Images of oil red O-stained worms subsequent to electrophile HNE treatment. 12 age-synchronized hermaphrodites at day 1 adult stage were fixed and oil red O-stained, and subsequently manually aligned for image acquisition. Scale bars: 200 μm. The oil red O signals were quantified by circling the entire animal except for the pharyngeal region. See also Figure 6C for quantification and analysis. Note: images for RNAi-control group are reproduced in Figure 6C. Alkyne-functionalized electrophile was used for consistency with click-imaging-based assays in other datasets.

(M) Images of oil red O-stained wild type and indicated knockin worms subsequent to electrophile HNE treatment. 13 age-synchronized hermaphrodites at day 1 adult stage were fixed, oil red O-stained, and manually aligned and shown in each image. Scale bars: 200 μm. The oil red O signals were quantified by circling the entire animal except for the pharyngeal region. See also Figures 6D and 6E for quantification. Alkyne-functionalized electrophile was used for consistency with click-imaging-based assay data elsewhere.

All data present mean ± SEM.

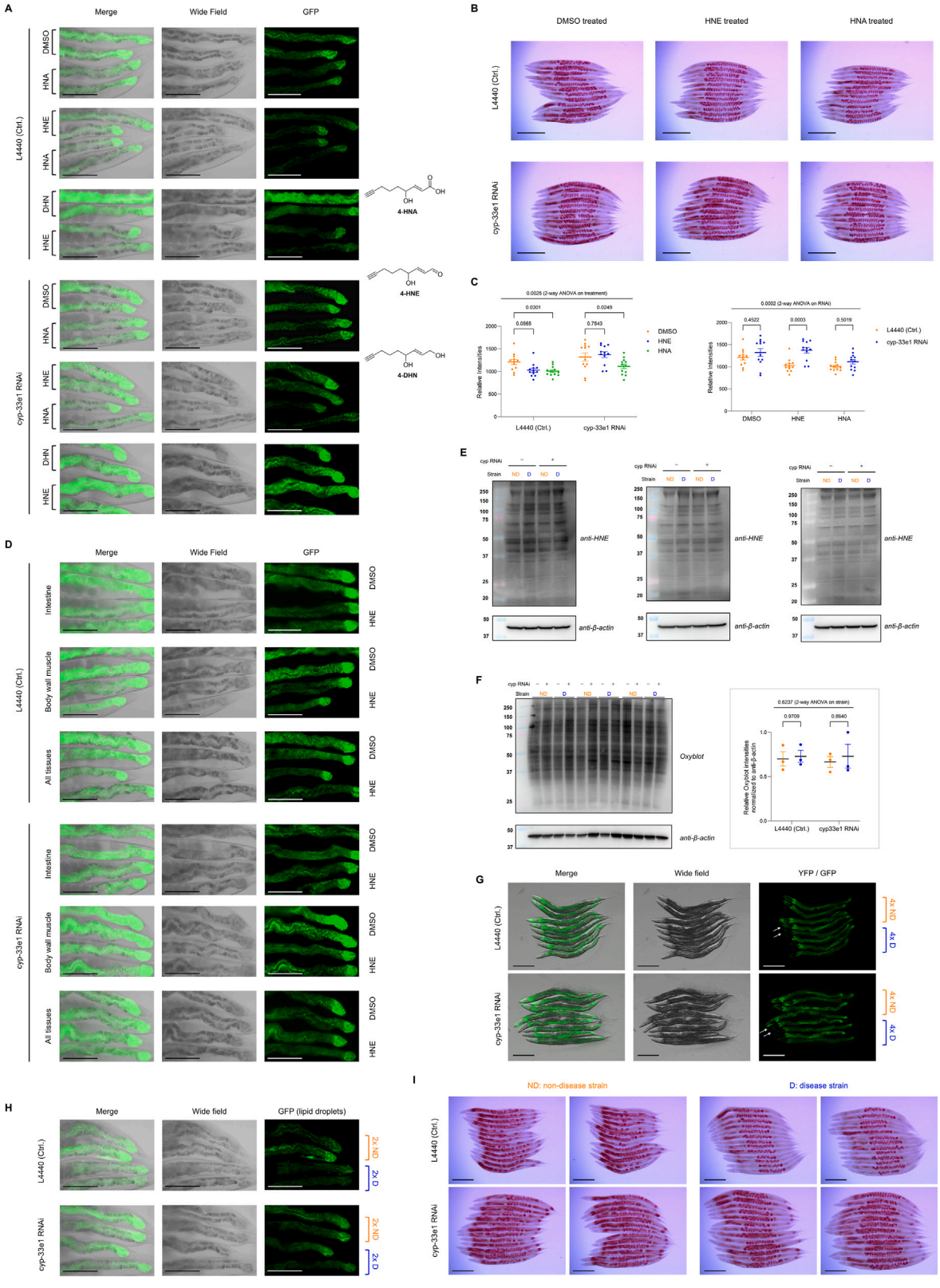

(legend on next page)

Figure S7. Cyp-33e1-dependent production of metabolite (HNA) promotes lipid depletion in both exogenous HNE-exposed animals and in neurodegenerative disease-inflicted animals with endogenous HNE stress, related to Figure 7

(A) Images of *C. elegans* posterior intestine, following either DMSO, HNE, HNA, and DHN treatment in the presence of cyp-33e1 RNAi or RNAi control. 4 age-synchronized, adult *dhs-3p::dhs-3::gfp* hermaphrodites were aligned manually after levamisole immobilization. In every image, the top 2 worms and the bottom 2 worms were treated under indicated conditions. In L4440 (control) groups, HNA-treated worms, and HNE-treated worms, both showed decreased lipid-droplet signals, relative to the DMSO- and DHN-treated worms. In cyp-33e1-RNAi groups, only HNA-treated worms showed decreased lipid-droplet signals relative to DMSO-, DHN, and HNE-treated worms. Scale bars: 100 μm. See also Figure 7A for quantification. Alkyne-functionalized versions of the small molecules were used for consistency with click-imaging-based assay data elsewhere.

(B) Images of oil red O-stained worms with either HNE or HNA treatment in the presence of cyp-33e1 RNAi or RNAi control. Representative images of oil red O-stained age-synchronized hermaphrodites at day 1 adult stage, validating decreased lipid levels in HNA-treated worms in both RNAi control and cyp-33e1-RNAi groups. Consistent with other data elsewhere, HNE treatment decreased oil red O signals in RNAi-control groups but not in cyp-33e1-RNAi groups. 12 fixed worms were manually aligned and shown in each image. Scale bars: 200 μm.

(C) Quantification of data in (B), presented in 2 different formats. Quantification of oil red O signals was performed by circling the entire animal except for the pharyngeal region to compare the effects of treatments. *p* values were calculated by Dunnett's multiple comparisons test post two-way ANOVA. Alkyne-functionalized versions of the small molecules were used for consistency with click-imaging-based assay data elsewhere. $n = 12$ for all conditions.

(D) Images of the *C. elegans* posterior intestine under organ-specific cyp-33e1 RNAi. 4 age-synchronized adult *dhs-3p::dhs-3::gfp* hermaphrodites at day 1 adult stage were aligned manually after levamisole immobilization. In every image, the top 2 worms and the bottom 2 worms were treated under indicated conditions. In L4440 (control) groups, all three strains (housing differential RNAi-machinery, see Methods S2D–S2G) showed decreased lipid-droplet levels following HNE treatment. By contrast, only intestinal-specific and ubiquitous-cyp-33e1-RNAi worms showed blockage of HNE-induced lipid depletion, whereas BW-muscle-specific cyp-33e1-RNAi worms failed to block HNE-induced lipid depletion. Scale bars: 100 μm. See also Figure 7C for the quantification results.

(E) Western blot analyses of HNEylated proteomes in *C. elegans* Huntington's diseased (D) strains and age-matched non-diseased (ND) animals subjected to cyp-33e1 RNAi or control RNAi. The higher degree of endogenous HNEylation was validated in *dhs-3p::dhs-3*::gfp × unc-*54p::htt513(Q128)::yfp* worms (diseased strain, D) using 3 independent biological replicates of anti-HNE western blots. See Figure 7F for quantification. The data from worms subjected to cyp-33e1 RNAi further reflect the higher levels of endogenous HNE selectively associated with L4440-fed (control, no RNAi) worms but not with cyp-33e1-RNAi worms. *p* values were calculated by Šidak's multiple comparisons test, post two-way ANOVA.

(F) Oxyblot analyses of HNEylated proteomes in *C. elegans* Huntington's diseased (D) strains and age-matched non-diseased (ND) animals subjected to cyp-33e1 RNAi or control RNAi. Contrasting the data in (E) and Figure 7D, the levels of carbonylated proteomes are indifferent across *dhs-3p::dhs-3*::gfp × unc-*54p::htt513(Q128)::yfp* worms (diseased strain, D) and age-matched *dhs-3p::dhs-3*::gfp × unc-*54p::htt513(Q15)::yfp* worms (non-diseased strain, ND) either in the absence or present of cyp-33e1 RNAi. 3 independent biological replicates of oxyblots are shown. Inset on the right: quantification. *p* values were calculated by Šidak's multiple comparisons test, post two-way ANOVA. $n = 3$ for all conditions.

(G) Fluorescent images of doubly Tg *C. elegans* Huntington's disease model strains (generated and validated as shown in Methods S2H), in the presence of cyp-33e1 RNAi or RNAi control. Age-synchronized hermaphrodites of indicated strains were subjected to control RNAi (empty vector L4440) or RNAi(cyp-33e1). 4 adults encoding: *dhs-3p::dhs-3*::gfp × unc-*54p::htt513(Q15)::yfp* (upper 4 worms, non-disease strain, ND) and *dhs-3p::dhs-3*::gfp × unc-*54p::htt513(Q128)::yfp* worms (lower 4 worms, disease strain, D) were aligned manually after levamisole immobilization. White arrows illustrate the known aggregation of Huntington (Htt) protein selectively observed in D strain but not in age-matched ND controls. See also (H) and Figure 7D. Note: YFP signal (fused to Htt protein) is selectively expressed in body-wall muscles, and thus it does not interfere with the lipid-droplet reporter GFP signal in the intesting. This result was independently validated using oil red O staining (I and Figure 7E). Scale bars: 200 μm.

(H) Fluorescent images of doubly Tg *C. elegans* Huntington's disease model strains (generated and validated as shown in Methods S2H), in the presence of cyp-33e1 RNAi or RNAi control, zoomed into posterior intestinal regions. Experimental setup as in (G). 2 adults encoding: *dhs-3p::dhs-3*::gfp × unc-*54p::htt513(Q15)::yfp* (upper 2 worms, ND strain) and *dhs-3p::dhs-3*::gfp × unc-*54p::htt513(Q128)::yfp* worms (lower 2 worms, D strain) were aligned manually after levamisole immobilization. Animals were age-synchronized hermaphrodites at day 1 adult stage. Scale bars: 100 μm. See also (G) and (I) and Figures 7D and 7E.

(I) Images of oil red O-stained doubly Tg *C. elegans* Huntington's disease model strains. 13 fixed age-synchronized day-1 adult hermaphrodites encoding either *dhs-3p::dhs-3*::gfp × unc-*54p::htt513(Q15)::yfp* worms (non-disease strain, ND) or age-matched *dhs-3p::dhs-3*::gfp × unc-*54p::htt513(Q128)::yfp* worms (disease strain, D) that had been oil red O-stained were manually aligned and shown in each image. Scale bars: 200 μm. The oil red O signals were quantified by circling the entire animal except for the pharyngeal region. *p* values were calculated by Šidak's multiple comparisons test, post two-way ANOVA. See also (G) and (H) and Figures 7D and 7E.

All data present mean ± SEM.